Unraveling distinctive sulphide mineralization and hydrothermal alteration on shallow seafloor hydrothermal systems

Ole Johan Hornenes

Master of Science Thesis

Department of Earth Science
University of Bergen
March 2017

Abstract

Since the discovery of seafloor hydrothermal systems in the late 1970´s, they have been found in different types of geological settings. Recent discoveries of active, inactive and inferred vent fields on the Arctic Mid Ocean Ridge reveals that hydrothermal activity might be more common than previously assumed. The Artic Mid Ocean ridge is a slow to ultra-slow spreading ridge, which can sustain long-lived hydrothermal activity with the potential to form large polymetallic mineral deposits. There is a growing interest in exploitation of seafloor hydrothermal deposits, as global demand for metal resources is growing. Exploration for these seafloor massive sulphide deposits is therefore an opportunity for academic research, and discovering metal resources of economic value. This thesis focuses on Perle and Bruse vent fields located on the southern segment of Mohn´s ridge and Aegir Vent Field located on central Mohns ridge. Perle and Bruse are part of the Jan Mayen Vent Fields, which also includes Troll wall and Soria Moria. Jan Mayen Vent Fields were discovered in 2005 during the BIODEEP-05 cruise. Perle and Bruse were later discovered in 2013 during the CGB cruise, and explored and sampled during the 2014 CGB cruise. Aegir Vent Field was discovered during the 2013 CGB cruise, and explored and sampled during the 2015 NORMAR/CGB cruise, and 2016 CGB cruise. Polished thin sections from the sampled material, was studied in transmitted and reflective light followed by Scanning Elecron Microscope using EDS to understand the petrography and mineralogy. Samples were powdered for isotopic analyses of Strontium, sulphur, radiometric dating of barite and whole rock geochemistry. Active chimney material from Perle is dominated by anhydrite, while barite is found in sampled mound rubble. Active chimneys from Bruse are dominated by barite, and have relict crystals of anhydrite that are partly dissolved. Both Vent fields are dominated by the sulphides pyrite, chalcopyrite, sphalerite and minor amounts of galena. Bruse has higher amounts of silica and the sulphide covellite, which is reworked from chalcopyrite. Radiometric dating shows that samples from Perle (7,4±0,4) is younger than Bruse (1400±50). Aegir shows a range of mineralogical assemblages that seems to be caused by age differences. The material is dominated by anhydrite, which seems to dissolves as the chimneys grow older, getting more enriched in barite, silica and sulphides. The sulphide phases are dominated pyrite, sphalerite, chalcopyrite and galena. Sr isotopes shows a degree of mixing between the hydrothermal fluid and seawater endmembers, Perle and Bruse shows an isotopic ratio closer to the hydrothermal fluid end member than Aegir which is closer to seawater values. Perle and Bruse have sulphur isotopes with values close to seawater.

Acknowledgements

I would first like to thank my supervisors Ana Filipa Alfaia Marques and Rolf Birger Pedersen from the University of Bergen for the guidance and for corrections and feedback on my work. I would also like to thank you for the opportunities you have given me during these two years with work tasks as a student assistant during two semesters, and with organizing some of the rock collection from the CGB cruises. I would also like to give a special thanks to Rolf Birger Pedersen and Ingunn Hindenes Thorseth for inviting me to the CGB cruise of 2016. I am very grateful for the opportunities as I have learned a lot from these experiences and it has inspired me to work further within this field.

I would like to thank Irina Maria Dumitru for excellent work with the making of the thin sections for my project; I am very impressed with how you managed to make thin sections of excellent quality from such challenging material. A big thanks to Martina Suppersberger Hamre for giving me a tour of the crushing lab and instructing me in how to prepare the rock powders, and to Ole Tumyr for giving safety instructions and allowing me to use the Rama lab. Yuval Ronen is greatly appreciated for his work with the strontium analysis, the digestion of samples for bulk chemical analysis and helping me write the section on sample preparation for analysis. I would like to thank Irene Heggstad, Trygve Knag and Egil Severin Erichsen for help and assistance with the Scanning electron microscope. A big thanks to Hildegunn Almelid and Siv Hjorth Dundas for bulk chemical analyses and for taking time to show me the analytical instruments used and to explain how the analyses were done. Thanks to Ana Filipa Alfaia Marques for providing me with sample ages derived from barite dating and Thanks to Cédric Hamelin and Ana Filipa Marques for sample photos taken during the CGB cruise. A big thanks to Oles Savchuk for preparation of powders and cutting samples for thin sections for the Perle and Bruse samples. I greatly appreciate the help I have gotten from Eoghan Reeves, Desiree Roerdink, Ingeborg Elisabet Økland and Adam Thomas Schaen with practical issues, discussions and providing me with literature.

I would like to thank my fellow students at the University of Bergen, and all the people that have made my studies such a good time. It is a privilege to have met so many great people.

Lastly I would like to thank my family and friends, you are valued beyond measure. Thank you all for supporting me during my study in Bergen.

Table of content

1 Introduction

The deep ocean is poorly understood and can be viewed as the last frontier in exploration of the Earth. The ocean has been mapped, but a large majority with a low resolution of ~5 km, which only makes it possible to detect large structures. Only around 10-15 % of the world's oceans have been mapped with a resolution of ~100 m, and only ~0,05 % with the highest resolution possible with sonar. Compared to this the resolution of the mapping done of the surfaces of the moon and mars is at a ~100 m (http://moocs.southampton.ac.uk). The fact that the world's oceans are so understudied makes it relevant for both academic research and industrial ventures. The first seafloor hydrothermal system was discovered in 1977 during the Alvin diving expedition to the Galapagos rift. During this expedition four vent areas were found along the axial ridge within the central rift (Corliss et al., 1979). With the use of the manned submersible, scientists were able to see for the first time how relict volcanic massive sulphide deposits that were found on land were created in the deep sea (Hannington, 2014). What they found during the dive was four active vent areas with mound dimensions of 30 to 100 m, from the vent area warm hydrothermal fluids were emanating (Corliss, 1979). The presence of hydrothermal convection in the oceanic crust were already a topic before the discovery, due to the discovery of hydrothermally altered ophiolitic rocks lead to the conclusion that hydrothermal processes must have occurred in the sub-seafloor (Spooner et al., 1974). A total of 521 hydrothermal vent fields have been discovered globally, with only a third of the length of the global oceanic spreading ridges surveyed for hydrothermal activity (Beaulieu et al., 2013). It has been suggested that there are still ~900 vent fields yet to be discovered (Beaulieu et al., 2015). Active seafloor hydrothermal systems are relevant for biology, and have a wide range of organisms that are adapted to the conditions at the vents. The conditions at the vent sites may be extreme, but the vents supply elements and organic compounds that can support life without photosynthesis. It is possible that hydrothermal systems played a significant role in the origin of life, and how life evolved (Martin et al., 2008). The resent discovery of lokiarchaeota shows that the eukaryotic host cell could have emerged from the archaeal domain of life (Spang et al., 2015). There is often abundance of life around the hydrothermal systems, and animals such as clams, shrimps, crabs, mussels and worms are often found in abundance (Grassle, 1985). Seafloor hydrothermal systems may carry metal-rich fluids that precipitate as sulphides during their upflow due to changes in temperature, pressure or pH forming accumulations of massive sulphides on the sea bottom or at the subsurface (Alt, 1995; Tivey, 2007). These accumulations are considered to be the modern analogues of ancient volcanogenic massive sulphide deposits (VMS) found on land (Tornos, 2006; Ohmoto, 1996; Scott 1997; Hannington 2014; Franklin 2005). VMS deposits have since the time of the ancient Greeks and up to modern times been an important source of metals, especially copper, zinc, lead, gold and silver (Jamieson et al., 2014). High demand for industrial metals such as copper have led to demand for the discovery of new ore deposits, and this opens for the possibility of exploiting seafloor massive sulphide deposits. Few mining companies have been interested in the exploitation of SMS deposits, but low metal prices and technological barriers have delayed these mining ventures from happening (Van dover, 2011; Boschen, 2013). With increasing mineral prices in 1990 there has come a new interest in the prospect of mining SMS deposits. In 1997 and 2011 the government of Papua New Guinea conceded exploration licenses and mining leases to Nautilus Minerals (Van Dover, 2011; Boschen 2013; www.Nautilusminerals.com). Nautilus Minerals have explored Papua New Guinea, Solomon Islands, Tonga and Clarion Clipperton Zone in the central Pacific Ocean for resources, and to look for commercially viable projects. They currently have a copper-gold project on Solwara 1 within the territorial waters of Papua New Guinea (www.Nautilusminerals.com). As of 2016 the company is acquiring production tools and vessels, if the project is successful it opens a new source of industrial minerals (www.Nautilusminerals.com).

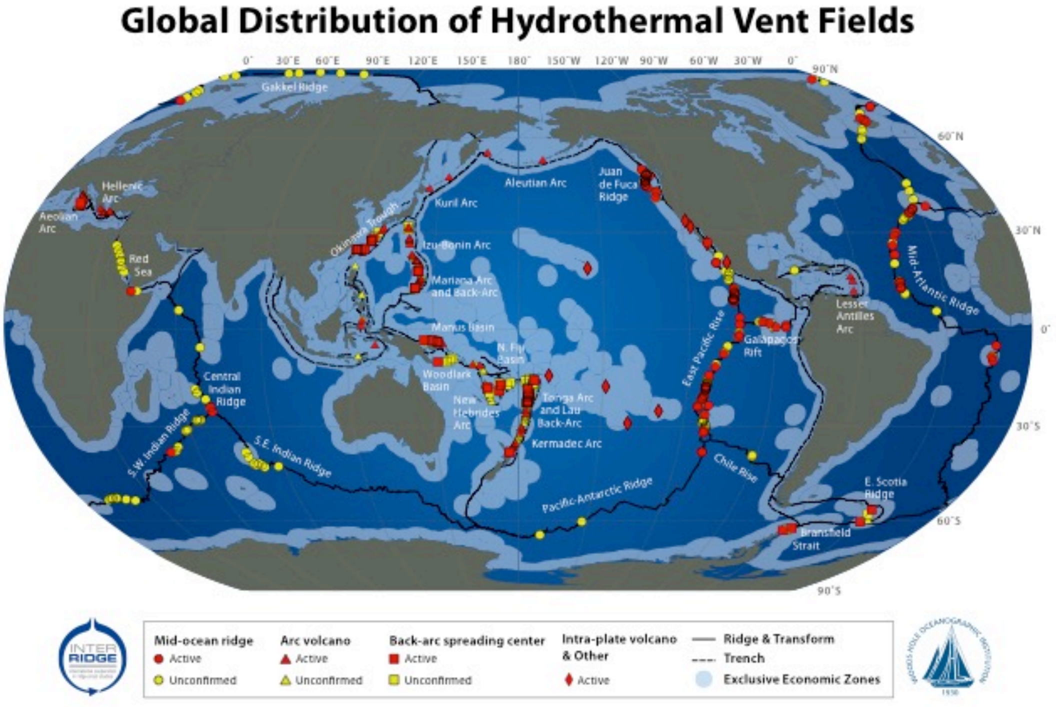

Figure 1: Map of the global distribution of discovered hydrothermal systems and related mineral deposits. The map is based on version 2.0 of the InterRidge vent database (Beaulieu et al., 2010).

1.2 Aim of study

- Petrographic and mineralogical characterization of the Perle, Bruse and Aegir vent systems.
- Comparison of the Perle and Bruse vent field.
- Compare Perle and Bruse with Aegir that is found on the central Mohns ridge.

2 Geological setting

2.1 The Arctic Mid-Ocean Ridge (AMOR)

The AMOR is the portion of the Mid-Atlantic ridge that lies north of the Arctic Circle at 66°N, from the northern shelf of Iceland (66°N) to the Siberian shelf in the Laptev Sea (77°N). This ridge system has a total extent of 4000 km and can be subdivided into six super segments with different lengths; (1) the Kolbeinsey ridge (540 km), (2) the Mohns ridge (550 km), (3) the Knipovich ridge (500 km), (4) the Molloy ridge (60 km) (5) The Lena trough (330 km), and (6) the Gakkel ridge (1600 km) (Pedersen et al., 2010b). The ridge system has three large/major fracture zones. This includes the west Jan Mayen fracture zone that lies at 71°N and limits Mohns ridge from the extinct Aegir ridge and the active Kolbeinsey ridge (Gernigon et al., 2009), Spitsbergen 77°N, and Molloy fracture zone that lies around 79°N. Two orientation changes also occur at 74°N separating Mohns ridge from Knipovich ridge and at 83°N that separating the Lena trough from Gakkel ridge (Pedersen et al., 2010b).

2.1.1 Spreading rate

Ultra slow spreading ridges have a full spreading rate below 12 mm/yr, but the common characteristics of an ultraslow spreading ridge can be found on ridges with full spreading rates up to 20 mm/yr (Dick et al., 2003). Gakkel ridge can be classified as a ultra slow spreading ridge as it has spreading rates that range from 6 mm/yr to 12.7 mm/yr, the rest of the arctic mid-ocean ridge has spreading rates that range from 13-18mm/yr (Dick et al., 2003; Cochran et al., 2003). The arctic mid-ocean ridge has full spreading rates that lie between slow and ultraslow.

2.1.2 Tectonic evolution

The onset of ridge spreading started in mid-Eocene with the formation of a triple junction South of Greenland that joined the Labrador Sea ridge, the Mid-Atlantic ridge and the early phase of the Norwegian–Greenland Sea (Geli, 1993). With the opening of the Norwegian Sea initiated 53 million years ago, the Mohns ridge was formed spreading 2.5 cm/yr perpendicular to the NNW-SSE relative displacement between the European and Greenland plates. In early Oligocene, the spreading in the Labrador Sea stopped leading to the reorganization of seafloor spreading. During late Oligocene, a reorganization of the North Atlantic plate boundaries changed the spreading direction to WNW-ESE when the Greenland plate rotated counter clockwise relatively to the Eurasian plate, and rifting jumped westwards from the Aegir ridge to the East of the Greenland plate and formed Kolbeinsey Ridge (Geli, 1993; Deuteuil and Brun, 1993).

2.2 The Mohns ridge

The Mohns ridge extends for 550 Km and is located between Jan Mayen Island at 71°N and the bend at 73°30´N, 8°0´E, that separates Mohns ridge from Knipovitch. The ridge topography consists of several linear, parallel flank ridges that range from 1000 to 2000 m deep, and a rift valley that ranges from 2600 m to 3400 m depth (Perry, 1986). The rift valley deepens irregularly towards the Northeast from a depth of 2500 m to 3000 m near Jan Mayen fracture zone to 2800 m to 3500 m at it´s eastern end (Geli et al., 1994; Vogt, 1986). The ridge has an unusual bathymetry due to the absence of deep-trough continuous fracture zones, nearly perfect symmetry of flank topography and the presence of knolls within it´s valley, the largest having a relief of up to 500 m (Perry, 1986). The ridge trends N60°, WSW-ENE, with a highly oblique direction of spreading, 30° to 40° relative to the spreading axis (Deuteuil and Brun, 1993). The southernmost segment of the ridge however is spreading orthogonally, and is strongly influenced by the Jan Mayen hotspot (Pedersen et al., 2010b). Most of the geological features on the ridge indicate an extension around N110°±10° (Dauteuil and Brun, 1996). The axial valley of the Mohn ridge has oblique highs and valleys that are spaced 20 to 45 km apart (Dauteuil & Brun 1996). The valley walls display strong asymmetry as the Northwestern ridge crest has complex topography with steep slopes and high unevenness while the Southeastern ridge crest displays a smoother morphology. The same study recognizes over 430 volcanoes on the ridge with over 60 of which that have a distinguishable caldera whereas the rest of the volcanoes are dome shaped. The distribution of the volcanoes is tectonically controlled with them being preferentially aligned on the oblique highs or close to them. Faulting patterns vary along the ridge. Faults in the rift valley walls are short and slightly oblique to the trend of the walls. In the axial valley the faults are longer and display a more complex shape trending N020° to N045°, and then rotating to N060º closer to the walls running parallel. The orientation of the faults also varies as the Northwestern ridge crest has faults with generally larger vertical throw than the faults on the Southeastern shoulder. The faults on the Northwestern ridge crest has a throw of dominantly 500 m to 1000 m, on the

Southeastern ridge crest the throw is dominantly less than 500 m. The faults inside the axial valley have a mean throw of around 400 m (Deuteuil & Brun, 1996). Spreading rates at Mohns ridge have changed along time and show different phases of seafloor spreading. Studies done by Geli (1993) show that spreading rates have shifted from 12 Ma until today. In detail, between 12 Ma and 9.5 Ma spreading rates were about 10 mm/yr, between 9.5 Ma and 5.6 Ma spreading rates slowed down to about 5 mm/yr on both flanks. Between 5.6 Ma and 3 Ma the spreading rate increased to 10 mm/yr on the NW flank, and 9 mm/yr SE flank. From 3 Ma until present, spreading rates have decreased to about 8 mm/yr on the NW flank, and 7mm/yr on the SE flank. Studies done by Klingelhöfer et al. (2000a) and based on geochemical analyses show that the Mohns ridge is 4 to 5 km thick, agreeing with the results from seismic reflection data that point to a thickness of 4,0±0,5 km (Klingelhöfer et al., 2000b). It has been derived from seismics that the thickness of ocean crust averages 7.1±0.8 (White et al., 1992) Crustal thickness at mid ocean spreading ridges with half rates below 20 mm/yr shows large variations with thicknesses in the range of 3-8km (Chen, 1992; Reid and Jackson 1981). This variation appears to be due to crustal thinning due to transform faults, and changes in melt generation with spreading rate (Chen, 1992). However, on the southern segment of the Mohns ridge the crust is anomalously thick with crust up to 10 km (Kandilarov et al., 2012). In areas where the spreading centers intersect regions of mantle plumes, anomalously thick oceanic crust can form (White et al., 1992). Mantle velocities under the spreading ridge are low, and are thought to be due to serpentinization (Klingenhöfer et al., 2000a; Francis, 1981). S-waves indicate that layer 3 is composed of gabbros with a 10-30% amount of serpentinized peridotite. Basalts from the Jan Mayen platform display subaerial characteristics are nepheline normative, rich in incompatible elements and have REE-patterns strongly enriched in light REE (Neumann and Schilling, 1984). These platform basalts have $^{87/86}$Sr ratios that range from 0.703505 to 0.703178 (Svellingen and Pedersen, 2003) Oceanic tholeiitic basalts have $^{87/86}$Sr ratios of 0.702 (Engel et al., 1965) Meaning that the basalts are enriched in $^{87/86}$Sr. Elkins et al. (2016) points to the possibility of a mantle plume beneath Jan Mayen island that could lead to flow across the fracture zone and influence mantle temperature and basalt composition at the southern Mohn´s ridge. Basalts along Mohns ridge are tholeiitic pillow basalts with phenocryst assemblages changing North-Eastwards from olivine ± plagioclase ± clinopyroxene ± magnetite to olivine ± plagioclase ± chrome-spinel. This change is accompanied with a progressive decrease in the content of incompatible elements and light REE-enrichments (Neumann and Schilling, 1984). Basalts from Mohns ridge have $^{87/86}$Sr ratios that range from 0,702853 to 0,703212 (Schilling et al., 1999). Plume source magma mixing with adjacent ridge-derived magmas could explain the northward trend of diminishing Jan Mayen magma signature along the Mohns ridge (Elkins et al., 2016).

2.3 Seafloor hydrothermal systems at AMOR

A total of six active vent fields have been confirmed along the AMOR, namely the Grimsey, Kolbeinsey, and Seven Sisters vent fields all located on the Kolbeinsey Ridge, and the Jan Mayen, Aegir, and Loki´s castle vent fields on the Mohns Ridge (Olsen et al., 2016; Pedersen et al., 2005, 2010a, 2010b). In 2001 the ice-breakers PFS Polarstern and USCGC Healy conducted petrological, geophysical, and hydrothermal plume surveys along more than 1100 km of the Gakkel ridge resulting in the discovery of 9 to 12 hydrothermal plumes, and dredges that led to the recovery of sulphide chimneys and thereby the discovery of the Aurora site at 82°N,6°W (Edmonds et al., 2003). Additionally hydrothermal material with evidence for sulphide mineralization has been dredged in several locations giving evidence for the presence of sulphide deposits and inactive vent fields yet to be explored. Some of these potential sites are on the Lena Trough, Squid Forest inactive vent field on the Kolbeinsey ridge, Copper Hill , and Mohn´s Treasure that are both located on Mohns ridge (Pedersen et al., 2010b). On Knipovich ridge seawater anomalies indicates that there are yet a abundance of hydrothermal sites to be discovered on the AMOR, anomalies are detected at 75°N, 76°N and 77°N (Sundvor, 1997; Connelly et al., 2002; Connelly et al., 2007). Seawater anomalies were also detected during Leg 2 of the CGB cruise of 2016, this anomaly was detected on the Knipovich ridge at 77°N. This MSc thesis focus on two hydrothermal systems located on the Mohns Ridge, the Perle and Bruse near Jan Mayen vent field on the southern portion of the segment and the Aegir vent field on the central Mohns.

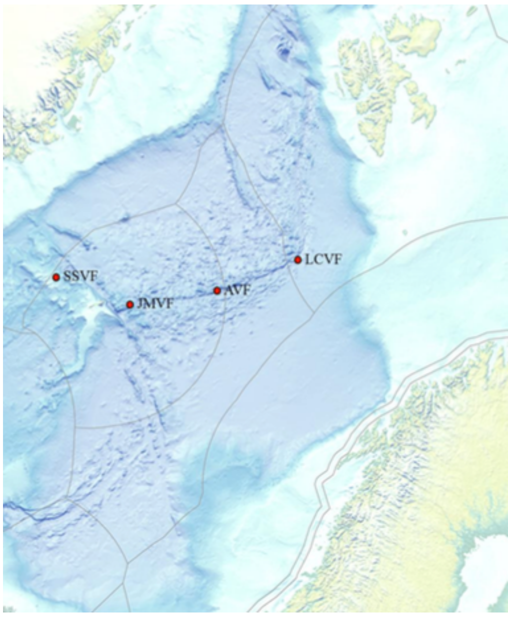

Figure 2: Location of Jan Mayen Vent Field (JMVF), Aegir vent field (AVF) and Loki´s Castle Vent Field (LCVF) on Mohn´s ridge And Seven Sisters Vent Field on the Northern Kolbeinsey ridge (Olsen et al., 2016)

2.3.1 Jan Mayen Vent Fields (71°N, 5°W)

The Jan Mayen Vent Field was discovered in 2005 during the BIODEEP-05 cruise on board of R/V G.O Sars (Pedersen et al., 2005; Pedersen et al., 2010b). The Jan Mayen system has three vent fields: Troll Walll and Soria Moria discovered in 2005 (Pedersen et al., 2010b) and Perle og Bruse found in 2013 and first explored in 2014 (F. Marques, personal communication). The Jan Mayen Vent Field is within the southern segment of Mohns ridge, 50 km north of the West Jan Mayen Fracture Zone (Pedersen et al., 2005). The vent fields are situated in the central part of the segment at 71°N and 6°E, bounded by the Jan Mayen Fracture Zone to the south and a nontransform offset to the north (Pedersen et al., 2010b).

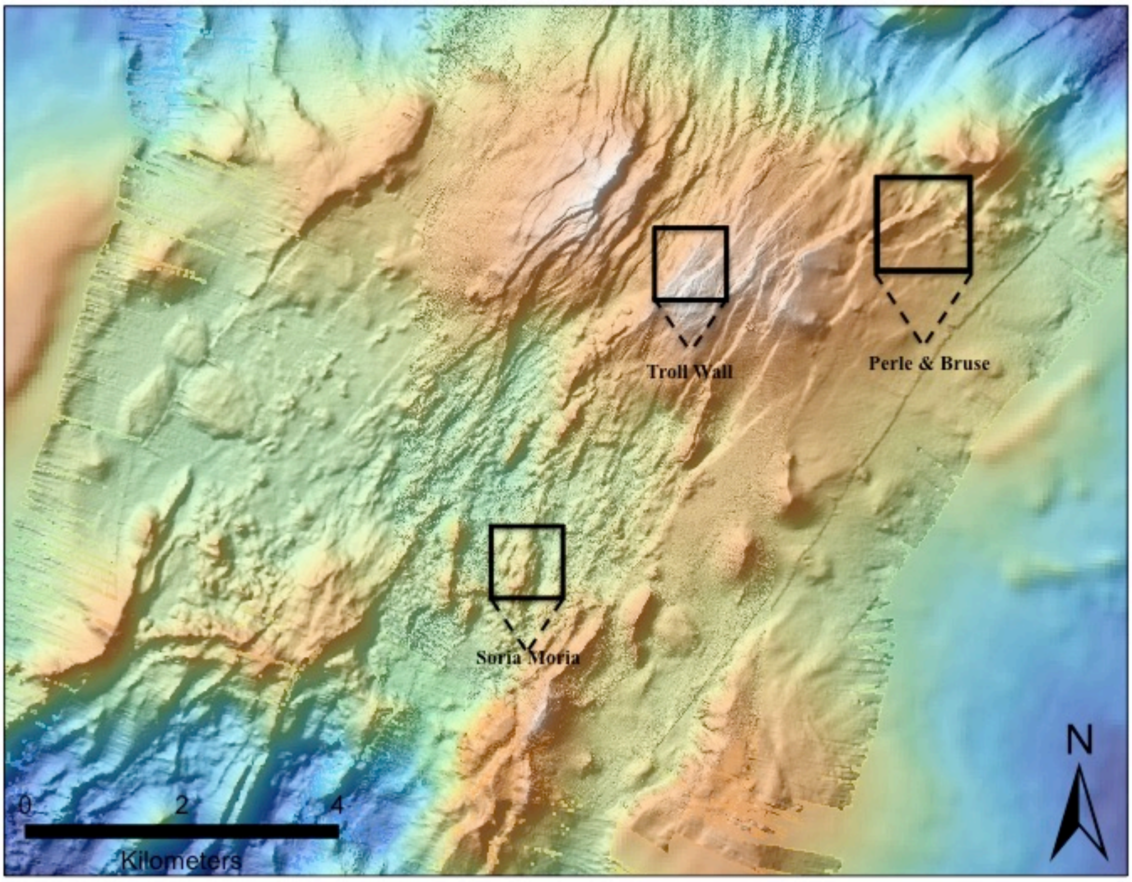

Figure 3: Location of Soria Moria Vent Field, Troll Wall Vent Field and Perle and Bruse on the Southern segment of Mohn´s Ridge. The map is modified from Pedersen et al., (2016).

2.3.1.1 Troll Wall

This vent area is located in the eastern margin of a rift valley in the shallowest part of ridge segment of Southern Mohns ridge. The venting of this field occurs trough talus deposits found along a 100 m high normal fault, venting occurs around 1 km of the fault and are intensified in a area where a single fault branches into two semiparallel faults that trend 40°. Along the faults and fissures of the rift diffuse venting have formed extensive iron oxide-hydroxide deposits. The vent field is found at a depth of ~550 m and consists of at least 10 major vent sites that each is composed of multiple chimneys that are up to 5-10 m tall. The fluids of the vent field was measured to be maximum 270°C and gas bubbles that are CO_2 dominated are escaping from multiple vent sites indicating phase separation. The chimneys are composed of anhydrite, barite, sphalerite and pyrite (Pedersen et al., 2010b).

2.3.1.2 Soria Moria

This vent area is found ~5 km south of the Troll Wall vent area, located on top of a volcanic ridge. The hydrothermal deposits of this vent area rests directly on lava flows that forms the volcanic ridge. The vent fields occurs in two discrete areas separated by a few hundred meters and the vent fields appears to be ~100-200m in diameter. There seems to be no structural control on one of the vent fields, while the other appears to be linked to a small fault basin. The vent fields are found at a depth of ~700m and the vent fluids reach temperatures of ~270°C. There are two different types of chimneys of the vent area. Sulphide chimneys that are up to 8-9 m tall are formed from white smoker fluids, and clear low temperature fluids forms irregular constructions composed of barite, silica and minor amounts of the sulphide phase pyrite, sphalerite and galena. The irregular chimney constructions of the low temperature fluids are up to 10 m tall and 15-20 m wide (Pedersen et al., 2010b).

2.3.1.3 Perle and Bruse

Perle and Bruse are two sets of active vent chimney clusters located ~2 km from Troll wall in an Eastern direction. The vent fields are located ~300-400 m apart, and are both located along fault lineaments. The mounds of the hydrothermal systems is composed of sulphide and sulphate debris and both systems has vents that are relatively small with a height of up to 2 m, spaced a few meters apart. There are no signs of fallen chimneys on the mound, but amongst the mound material there was sampled hydrothermal clasts that has textural characteristics that resemble chimneys (GS14-ROV8-Shuffle). Around the hydrothermal systems there are extensive areas that are covered by Fe-Hydroxide plates, these plates has fractures from which diffuse venting occurs and bacterial mats are found. The hydrothermal systems are found at a depth of ~500 m, Perle at a depth of ~560 m; Bruse is found at a depth of ~590 m. The chimneys are composed of sulphide and sulphate minerals, fluids venting from the two chimney clusters differs. Perle vents clear fluids with bubbles measured to be up to 248°C, and mound temperatures of 95°C(F. Marques, personal communication); Bruse vents clear fluids with no signs of bubbles that was measured to be up to 242°C (E. Reeves, personal communication).

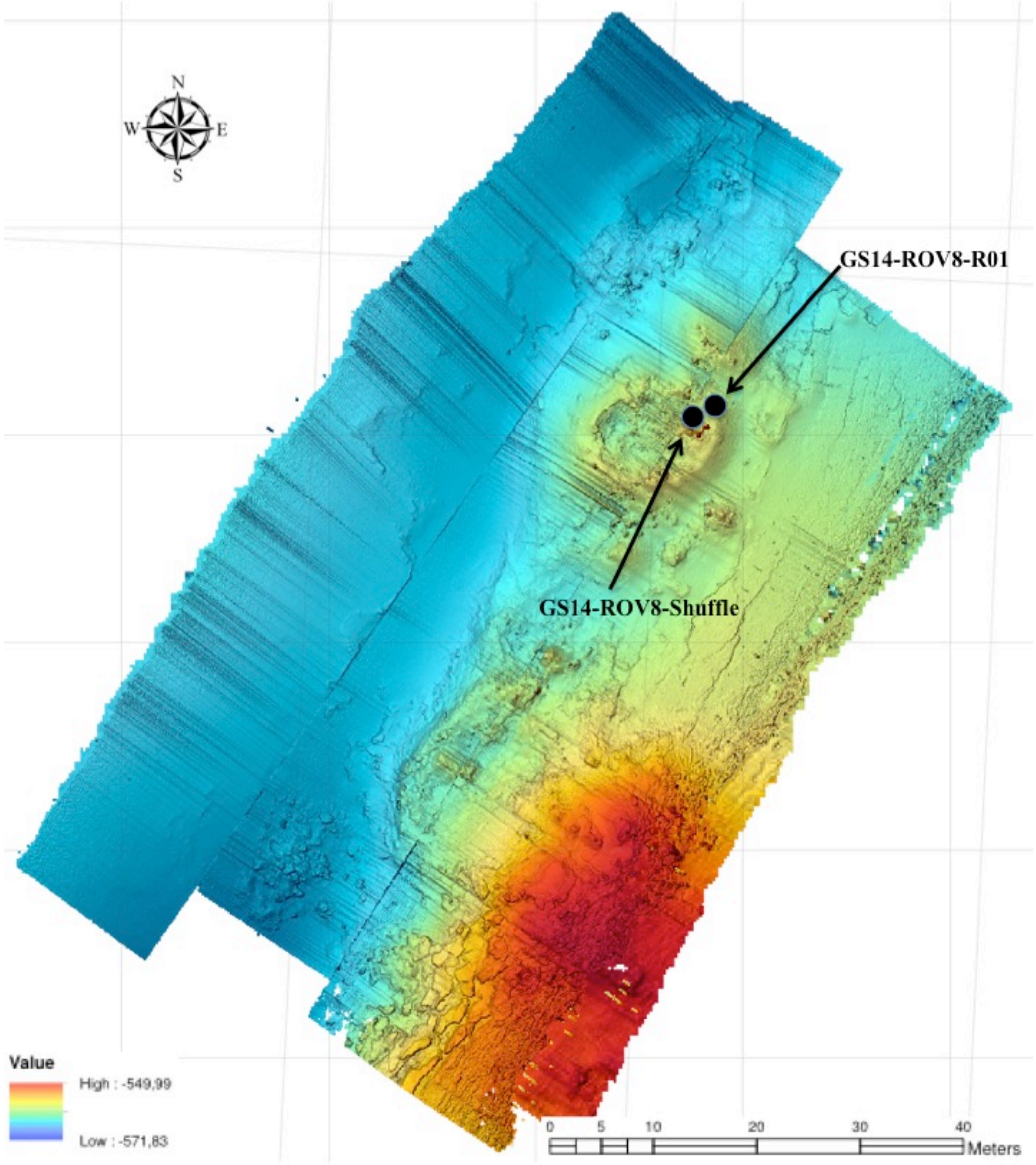

Figure 3: Map over the Perle Vent Field with sample locations shown for GS14-ROV8-R01 and GS14-ROV-Shuffle (Modified from Pedersen et al., 2016).

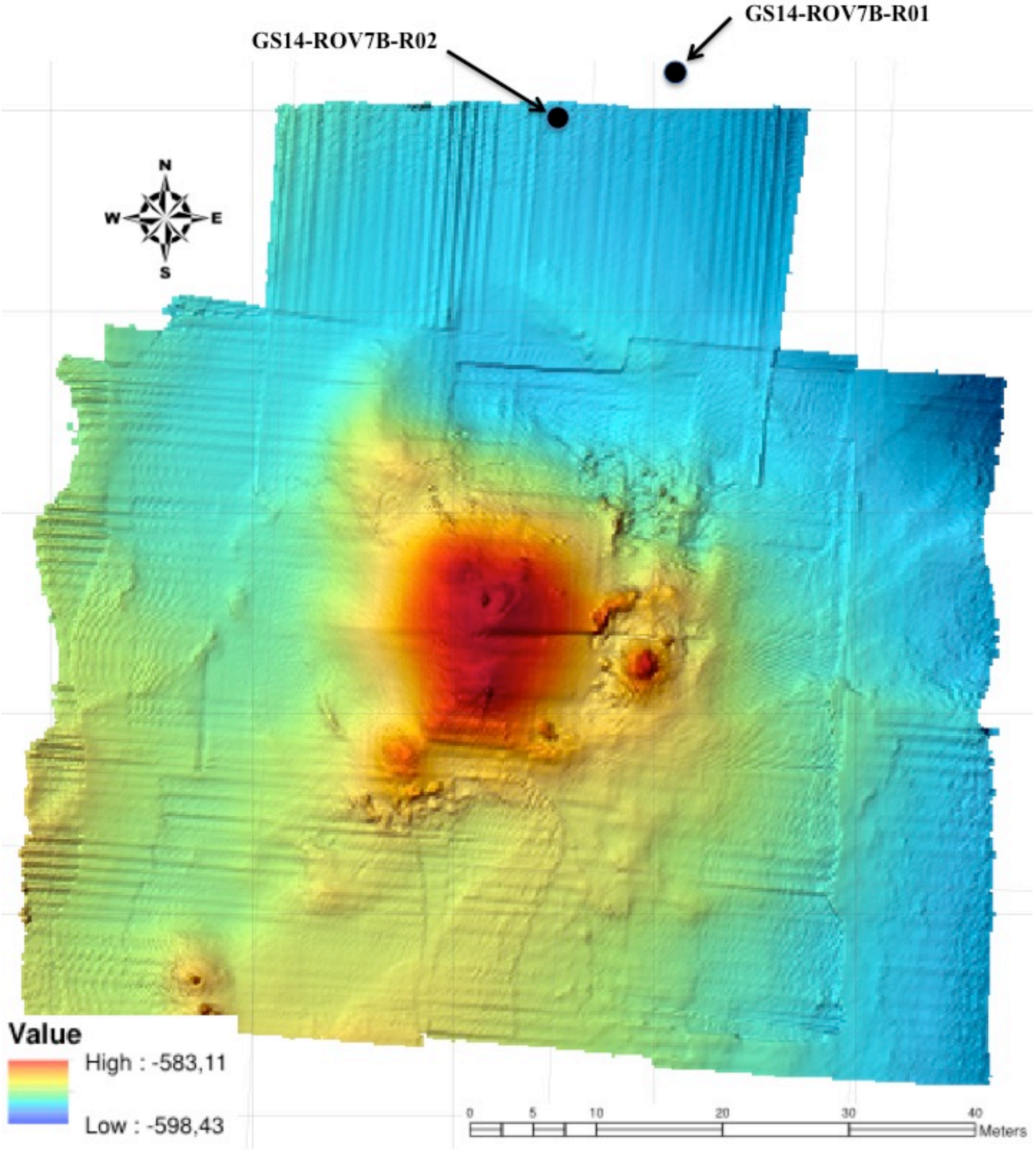

Figure 4: Map over the Bruse Vent Field with sample locations for GS14-ROV7B-R01 and GS14-ROV7B-R02 (Modified from Pedersen et al., 2016).

2.3.2 Aegir Vent Field (72°N, 1°E)

On the axial valley of the central Mohns ridge lays an oblique volcanic structure, the Hval ridge, standing orthogonal to the spreading direction. The structure is 26 km long by 8 km wide and raises 900 meters above the valley floor. Two large faults cut the Hval ridge at a N045°E direction, the Southeastern part is older and covered with sediment and has faulted terranes while the northern end has volcanoes and seems to be more recent. Basaltic pillow lavas cover the majority of the Hval ridge with a thin cover of sediment. The Aegir hydrothermal system was first explored during the cruise xxx on board of the R/V G.O. Sars by the CGB research team in 2015. A plume was detected over Hval ridge during the CGB 2013 expedition. During the 2015 NORMAR/CGB expedition Hugin were deployed to collect well-spaced lines of the same area. Using live stream of the methane concentration it was possible to locate a buoyant plume. A follow-up ROV dive discovered the Aegir vent field. Hydrothermal activity was located at ~2330 m deep, with a cluster of chimneys found on top of small mound deposits. The hydrothermal system is emerging from relatively fresh pillow basalts suggesting immature hydrothermal activity at this location. The fluids venting at Aegir are clear fluids with a max measured temperature of 279°C (E. Reeves, personal communications). Chimneys are preferentially distributed along fractures trending N045°E. Fractures around the chimneys shows and ochre coloured material and suggest diffuse venting activity. The hydrothermal deposits are relatively small and chimneys are found in clusters. The chimneys are composed of sulphate, silica and sulphides. Clusters of inactive chimneys were found nearby and suggest episodic hydrothermal activity in the area with volcanic activity and/or tectonic movements sealing fluid pathways and impacting vent distribution in the area.

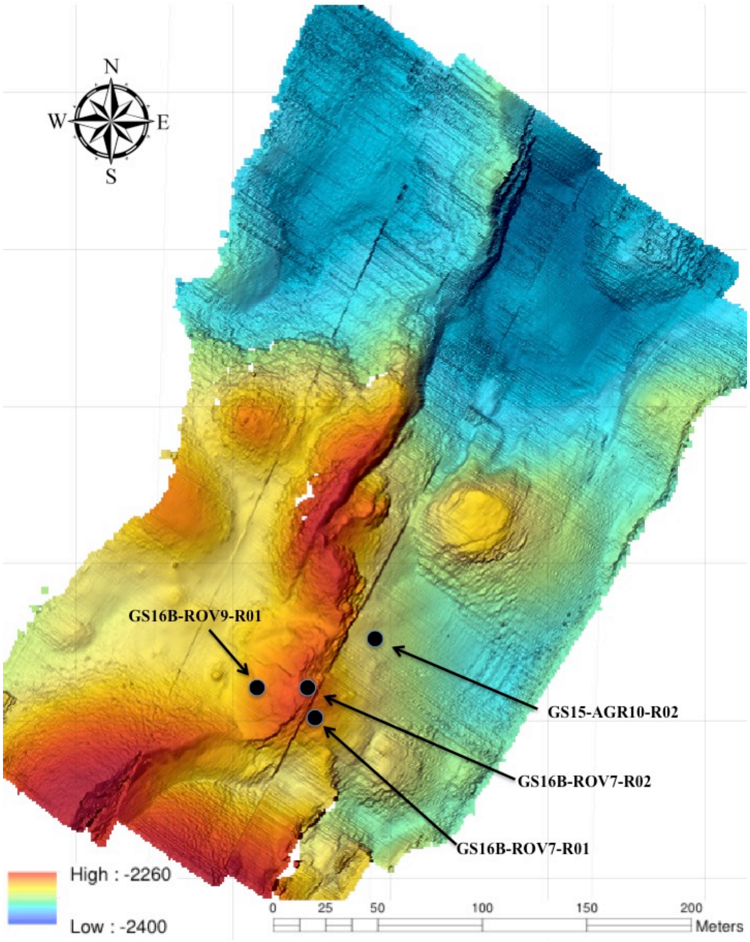

Figure 5: Map over the Aegir Vent Field with sample locations for GS15-AGR10-R02, GS16B-ROV7-R01, GS16B-ROV7-R02 and GS16B-ROV9-R01 (Modified from Pedersen et al., 2016).

2.3.3 Loki´s castle (73° N, 8° E)

This vent field is found along a 50-100 m deep rift that runs along the crest of a volcano. The vent areas are found above two Northeast striking normal faults that are semi parallel. The vent field is found at a depth of ~2400 m and black smoker fluids are 310-320°C. The vent field is composed of four active black smoker chimneys that are up to 13 m tall. The vent field has well developed sulphide mounds that are 20-30 m high and 150-200 m in diameter at the base. This size is comparable to the TAG mound that is one of the largest mounds known to date. The mineral phases of the chimneys is composed of anhydrite, gypsum, talc, sphalerite, pyrite, pyrrhotite and chalcopyrite (Pedersen et al., 2010a; Pedersen et al., 2010b).

3 Methods

3.1 Seafloor exploration and sampling

Perle and Bruse vent field (71°N, 5°W) at Southern Mohns ridge was discovered in 2013 using a multi-beam echo sounder EM302 that showed acoustic disturbances compatible with two bubble columns near to the Soria Moria and Trollveggen vent fields. This area was first explored during the CGB summer cruise on board of G.O Sars in 2014 by using two ROV (Aglantha and Mariner) and an AUV (Hugin) confirming that both bubble columns corresponded to actively venting hydrothermal fields. The ROV Aglantha is built by Argus remote systems, and is a large observation class electronic ROV, and can dive down to a depth of 600 m. The AUV used is a Hugin 1000 made by Kongsberg. It is owned and operated by the Norwegian Defense Research Establishment (FFI). It includes a sub-bottom profiler, "tilecam" optical camera system, turbidity sensor, magnetometer, methane sensors and CTD. It can be equipped with high-resolution interferometric synthetic aperture sonar. During leg 2 of the 2014 cruise the Perle og Bruse vent fields were explored again, this time using the ROV Argus Mariner XXL. This ROV is built by Argus remote systems and is a working class vehicle that can dive down to a depth of 6000 m. The ROV was equipped with, HD cameras, two manipulators, a grabber and a Schilling T4, a shuffle box, fluid and gas sampling apparatus and different scientific equipment added according to dive plans. Furthermore, during the 2013 CGB summer cruise a plume signal was detected in the water column at Hval ridge (72°N, 1°E) at the central Mohns ridge. In 2015, an AUV was used to survey and map the area using high-resolution HiSAS acoustic imaging and CH4 sensors defining areas of probable hydrothermal output. One ROV dive sufficed to find several active vent chimneys spreading over an active field area now named Aegir vent field. This time the ROV used was ÆGIR 6000, and is a supporter Mk 2 working class ROV manufactured by Kystdesign. It is equipped with HD cameras, two manipulators, an ATLAS grabber and a Schilling T4. It has one large sampling box, and different scientific equipment can be added according to dive plans. Both Perle og Bruse, and Aegir were explored later in 2016 using Ægir 6000. A total of 4 rock samples were sampled from Perle og Bruse with the use of the ROV Argus Mariner XXL in 2014. For this particular dive the ROV was equipped with a chainsaw that enabled the cut of a fresh surface on what seemed a feeding system to the vent chimneys at Bruse (GS14-ROV7B-R1), and an active chimney (GS14-ROV7B-R2). The remaining samples were taken from Perle where an active chimney (GS14-ROV8-R1) was collected with the use a grabber, and mound material (GS-ROV8-Shuffle) collected with the shuffle box. 4 rock samples were taken from Aegir vent field with the use of ROV Ægir 6000 in 2015 and 2016. There were collected fallen inactive chimneys (GS15-AGR10-R2 and GS16B-ROV7-R01), an inactive in-situ chimney (GS16B-ROV7-R02) and also a active chimney (GS16B-ROV9-R01). Sampling was done with the use of the grabbers of the ROV. After sampling, the samples were placed in the sampling/shuffle box until the ROV´s were brought on-deck. Once the samples were on deck, biologists and microbiologists were the first to sample the rocks probing from macro-fauna to microbes. The samples were then rinsed with fresh water and left to dry in an oven at temperatures lower than 48°C. Dried samples were then photographed, tagged and described. Subsequently the dried samples were packed and stored in sealed bags with nitrogen to prevent oxidation of the sulphides.

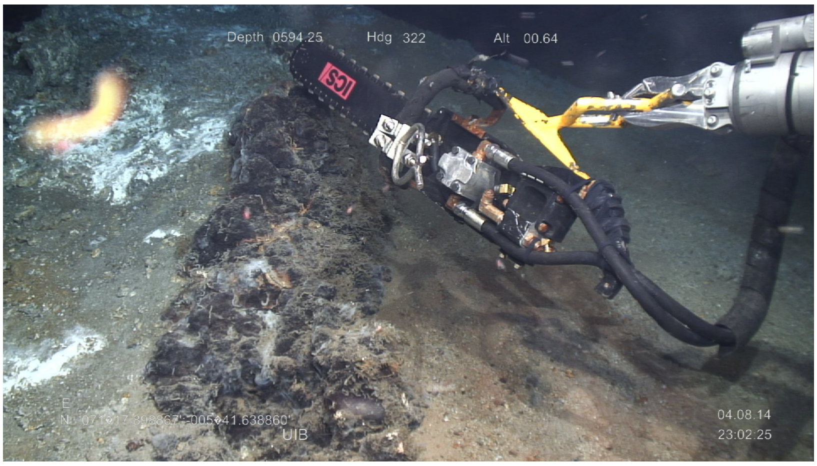

Figure 6: Sampling of the Bruse feeder structure (GS14-ROV7B-R01) using a chainsaw operated by the ROV.

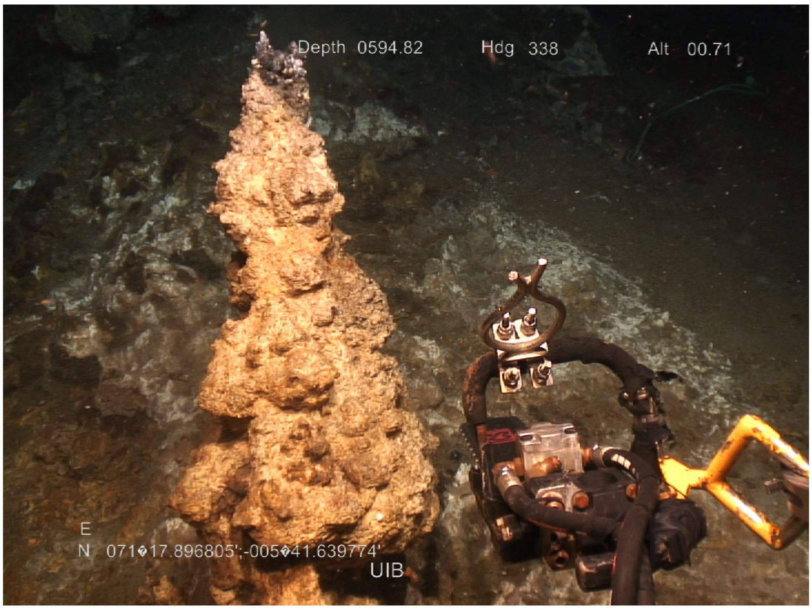

Figure 7: Sampling of a active chimney (GS14-ROV7B-R02) on the Bruse Vent Field using a chainsaw operated by the ROV.

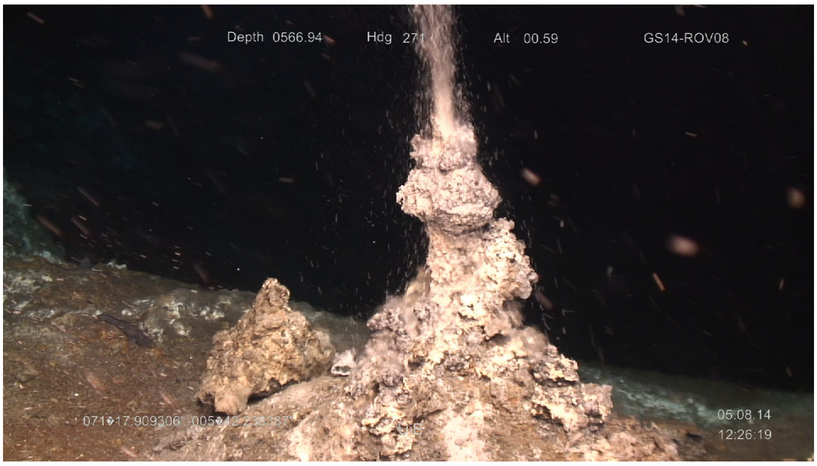

Figure 8: Picture of the active chimney (GS14-ROV8-R01) sampled at Perle Vent Field. This chimney was sampled with the use of the grabber.

Figure 9: Picture from the sampling of Perle mound material (GS14-ROV8-Shuffle) In the lower right of the picture it is possible to see the filling of the shuffle box.

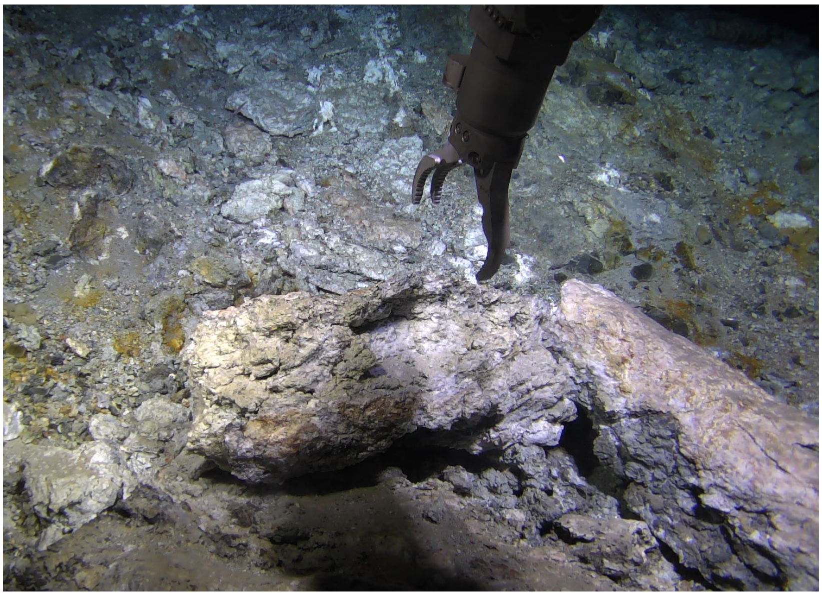

Figure 10: Picture of the sampling of an inactive chimney (GS15-AGR10-R02) at the Aegir Vent field using the ROV grabber.

Figure 11: Picture of the sampling of an inactive chimney (GS16B-ROV7-R01) at the aegir vent field using the ROV grabber.

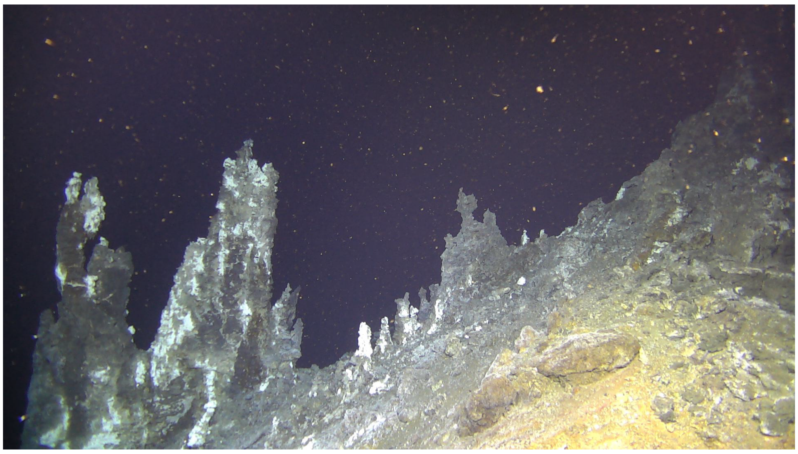

Figure 12: Picture of the inactive vent standing in situ (GS16B-ROV7-R02), it is the smaller vent standing to the right. It was collected using the grabber of the ROV.

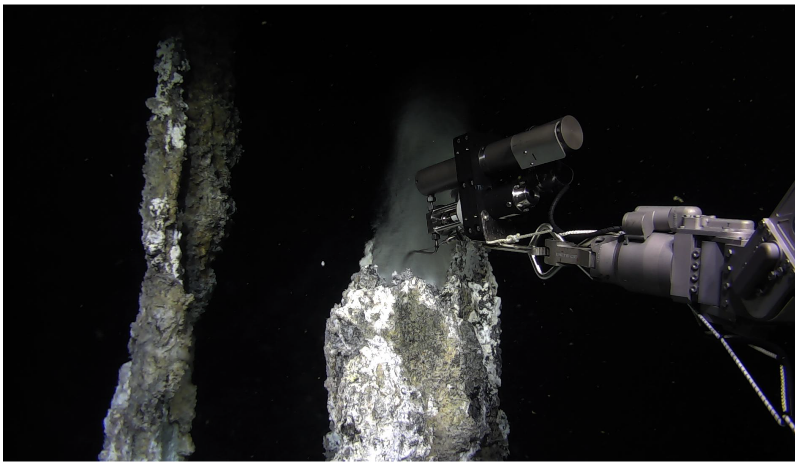

Figure 13: Picture of temperature probing and fluid collection from the active vent (GS16B-ROV9-R01). The vent was sampled with the use of the ROV grabbers.

3.2 Petrography

18 polished thin sections were studied in a petrographic microscope model Nikon ECLIPSE LV100POL in both transmitted and reflective light. Photomicrographs of the thin section were taken using the software program NIS-Elements BR 2.30. Brightness and image editing

was made using Apple Photo app. Scanning electron microscope (SEM) was used on the thin sections. The thin sections were first cleaned with 70 % etanol before they were carbon coated using Agar turbo Carbon coater for 15 seconds at 5 voltage. The SEM is owned by the University of Bergen and is a Zeiss Supra 55 VP, element analysis of the minerals in the thin sections was done with Energy Dispersive Spectrometry (EDS). From the work with petrographic microscope areas of interest were selected and pinpointed out with a marker (edding 141 F) to make it easier to locate the areas using the SEM. The thin sections were observed in both backscatter and secondary electron mode with a split screen. This way it was easier to detect the differences between the mineral phases of the thin sections. Once the areas of interest were located in-situ EDS semi-quantitative analysis was used for mineral ID.

3.3 Geochemistry

Rocks were crushed at the University of Bergen crushing lab. Weathered samples were carefully handled and using a diamond saw to remove alteration rims and cut to smaller portions. Samples were then wrapped in several layers of paper and crushed with a hammer precluding contact between the hammer and the rock. After the samples were crushed to approximately 2-0,1 mm size, particles were powdered using either an agate mill, or agate mortar.

3.3.1 Sulphur isotopes

Sulfur isotopes were analysed at ACTLABS. Barite was separated from the powdered samples by leaching them from the powders using HF, HNO_3 and HCl at UIB, and was sent to their lab in Canada for analysis. Pure barite is combusted to SO_2 gas under ~10^{-3} torr of vacuum. Combustion is achieved by mixing 5 mg of sample with 100 mg of V_2O_5 and SiO_2 mixture at a relationship of 1:1. Reaction takes place in a quartz glass tube at 950°C for 7 minutes. Copper turnings were used as a catalyst to ensure the conversion of SO_3 to SO_2. SO_2 has an inlet directly from the vacuum line to the ion source of a VG 602 Isotope Ratio Mass Spectrometer. The lab standards $SeaWater_{BaSO4}$ and $Fisher_{BaSO4}$ are run at the start and end of each set of samples, and are used to normalize the data and adjust for instrument drift (www.actlabs.com; Ueda, 1986).

3.3.2 Strontium isotopes

Strontium isotopes were analysed at University of Bergen. To remove organic impurities the sample was heated to 1000 °C for 1 hour in a Carbolite chamber furnace. Each sample was weighted to 0,1 gr each and digested with HF at a heating plate at 135 °C for 48 hours. HF was then evaporated to dryness and then hydrolysed in a weak solution of HNO_3 on the heating plate below boiling temperatures. The residue was then evaporated to dryness and dissolved in 1 ml of 3N HNO_3. Residual barium was separated from the solution by centrifugation using 2 ml micro-centrifuge tubes. Strontium was extracted from the samples trough specific extraction chromatography with Sr-spec resin. This step followed a modified version of the method of Deniel, 2001. Matrix was eluted with 2 portions of 2,5 ml 3N HNO_3 and one portion of 2,5 7N HNO_3 was added to remove Ba. Sr was then stripped from the column with 2 ml D-water. The eluate was stored in 2 ml micro centrifuge tubes and got evaporated to dryness. A small fraction of the extracted Sr was loaded onto Rhenium filaments and measured using a Finnegan MAT 262 thermal ionization mass spectrometer (TIMS) in double-filament configuration using dynamic mode. Sr ratios got corrected for mass fractionation using an $^{88}Sr/^{86}Sr$ ratio of 8,375209.

3.3.3 Dating of barite

The radiometric ages of barite from Perle og Bruse active and inactive chimneys were determined following the methodology of Ditchburn et al., 2012 using a short lived isotope system with $^{228}Th/^{228}Ra$ and $^{228}Ra/^{226}Ra$. Barite-dominated samples with well constrained mineralogy were sent to GNS Science (New Zealand) to be prepared and analysed by Professors Cornel de Ronde and Bob Ditchburn. The analytical steps described in Ditchburn et al., 2012 are as follows; samples are dried at 105 °C and crushed with pestle and mortar before the samples are gamma counted for the activity ratios of $^{228}Th/^{228}Ra$ and $^{228}Ra/^{226}Ra$. The sample is then added to a Pt dish with Na_2SO_4, K_2SO_4 and H_2SO_4 and heated until the salt fuses and fully decompose the sample. The solidified salt is then dissolved in boiling water to recover barite, $PbSO_4$ and silicate. Silicate is then removed through adding HNO_3 and HF and evaporating it to dryness. Fluoride is eliminated though adding Na_2SO_4, K_2SO_4 and H_2SO_4 and heating it until the melt clarifies, boiling water is then added to dissolve the solidified salt and barite and $PbSO_4$ is recovered. Barite and $PbSO_4$ is then dispersed in water and dissolved through adding it to boiling dilute alkaline EDTA, Pb carrier is added together with methyl red indicator. H_2SO_4 is added to precipitate $BaSO_4$ at a PH of 5, barite is recovered and Pb is retained in the solution. Barite is dried and weighed before it is gamma counted for ^{226}Ra. Results were then sent back and interpreted at the University of Bergen.

3.3.4 Geochemical analyses

Whole-rock geochemical analyses of major and trace elements were done at the University of Bergen and, by request, at Actlabs Canada. Sample pulverization for both in-house analysis and Actlabs was exclusively done at the University of Bergen. Two pulverized samples, one from an actively venting chimney at Perle and the other other from an actively venting chimney at Bruse were sent to ACTLABS in Canada for whole rock geochemistry analysis, for the in house analysis at UIB more powders had to be made from the active Perle chimney. The analysis were done by sodium peroxide fusion followed by ICP-OES, aqua regia digestion followed by ICP-OES, ICP-MS and INAA and cold vapour FIMS. For in-house analysis, sample digestion followed the initial steps similar to those as samples for strontium analysis. Samples were heated to 1000°C for 1 hour to remove organic impurities in a Carbolite chamber furnace. 0,10 gr of sample were weighted accurately in 25 ml PFA Savillex beakers and were digested in concentrated HF on a heating plate for 48 hours at 135°C. The HF supernatant was then evaporated to dryness and the residues hydrolysed in a weak solution of HNO_3 on a heating plate under sub-boiling point conditions. The nitrate salt residue was then evaporated to dryness and dissolved in 1 ml 3N HNO_3. Residue of barite was separated from the solutions by centrifugation in 2 ml micro-centrifuge tubes. The dissolved material was stored in 2 separate beakers for each sample. One contained the alkali earth elements, and one containing the H_2SO_4 resulting from the digestion with HF. The exception for this is the standard CZN-4 where all the dissolved material was stored in one beaker. There were no precipitates formed after the digestion with HF for this sample. Both beakers for each sample were analysed, after the analysis the values for each sample beaker were added together. The elements Al, Cu, Fe, K, Mg, Na, Pb and Zn were analysed with ICP-OES using a Thermo Scientific ICAP 7600. Scandium was used as an internal standard. Standard deviation was measured by running each sample 3 times. The elements Mo, Ag, Sb, As, Ti and Au were analysed with HR-ICP-MS using a Thermo Scientific element XR. Indium was used as an internal standard. Standard deviation was measured by running each sample 12 times. Standards used were BCR2, CCU-1d and CZN-4.

4 Theoretical background

4.1 Spreading rates

Hydrothermal systems occur dominantly along mid ocean ridges with spreading rates ranging from ultraslow going trough slow, intermediate, fast to ultrafast, but it can also occur along back arc spreading centers and associated with hot-spot related intraplate volcanism (German and Von Damm, 2006). Ultraslow ridge morphology occur when full spreading rate is under 12.7 mm/yr with Gakkel ridge as the only representative, but ridge morphology can occur on ridges with spreading rates up to 2 cm/yr (Dick et al., 2003). Ultra fast on the other hand have full spreading rates of over 12 cm/yr, the only spreading ridge that exceed these rates is the southern part of East Pacific Rise (German and Von Damm, 2006). Sub-lithospheric mantle temperatures are shown to decrease by 150°C from fast to ultraslow spreading regimes, both modelling and seismic structures of mantle structures beneath ridges indicate that most variation is found at shallow depth (Husson et al., 2015). Haymon, (1996) is indicating that there is a coupling between magma supply and hydrothermal fluxes for ridges with spreading rates between fast and intermediate, based on this it´s possible to classify ridge segments as either magma rich or magma poor independently of spreading rate. According to the publication magma rich segments are more common on segments of the ridge that has a fast spreading rate, and magma starved segments are more typical at slow spreading rates. It is not possible to determine in vent fluid chemical-data are coming from a ultrafast or slow spreading ridge, but spreading rate is however used as the proxy for magma supply for the ridge (German and Von Damm, 2006). Fast spreading ridges was long though of as the best setting for the development of large deposits of seafloor hydrothermal systems, but new discoveries on slow spreading ridges such as TAG (Humphris et al., 1995) and Loki´s castle (Pedersen et al., 2010a) indicate that you can get big accumulations of mineral deposits in these settings due to the stable conditions at these ridges (German and Von Damm, 2006). Slow spreading ridges are associated with tectonic activity rather than volcanic, this leaves the hydrothermal fluids more oxic because more dissolved seawater SO_4 has penetrated down to the reaction zone leaving the rocks within the hydrothermal cell more leached and altered (German and Von Damm, 2006).

4.2 Sub-Seafloor hydrothermal circulation

In hydrothermal systems heat is transferred trough the rock trough both convective circulation of water and thermal conduction trough the rock, this occurs in permeable rock as heated fluids will rise and cold fluids descends forming a convective cell (Renner et al., 1975). For oceanic crust with an age up to 70 Ma there exists a discrepancy in the heat flow that is measured and what thermal models of the cooling lithosphere is telling, as the heat flow is less than predicted (Stein and Stein, 1994). This discrepancy is explained by the presence of hydrothermal convection occurring in young oceanic crust (Fehn and Cathles, 1979). The heat flow discrepancy is largest at the mid ocean ridges and decreases with age, indicating that the hydrothermal water flux decreases with age (Stein et al., 1995). Magmatic heat sources will drive the convection of seawater trough the crust at mid-ocean ridges, the heated water that returns to the ocean forms sites of hydrothermal venting (Jupp et al., 2004). Alt (1995) describes the subseafloor processes that are taking place during hydrothermal activity into three zones: recharge, reaction and discharge zones. In the recharge zone where the seawater enters the crust and interacts with the rocks and gradually becomes heated which initiates low temperature reactions. At temperatures ranging from 40°C to 60°C reactions between basalt and seawater result in the alteration of olivine, plagioclase and basaltic glass with the formation of ferric micas, smectite, Mg-rich smectite, and Fe oxyhydroxides (Tivey, 2007; Alt, 1995). During these low temperature reactions, K, Rb, Cs, B and H_2O are removed from the seawater and added to the altered minerals, and Si, S and Mg are added to the fluids (Tivey, 2007; Alt; 1995). When the water penetrates deeper into the crust and is heated to temperatures above 150°C Mg is removed from the fluids due to formation of clays such as smectite rich in Mg and chlorite (Tivey, 2007; Alt, 1995). Between the temperatures of 150°C to 200°C anhydrite precipitates from the seawater (Bischoff and Seyfried, 1978) The precipitation of anhydrite removes all of the Ca from the seawater and around one third of the seawater sulphate, additional anhydrite precipitation can occur if Ca is released into the fluids from basalt (Tivey, 2007). In the reaction recharge zone the initial stages are inseparable from the low temperature reactions happening in the recharge zone, but in this zone the seawater gets heated which leads to changes in the fluid composition with physical conditions that are close to the critical point of seawater. In the reaction zone the fluids also become buoyant and start to rise towards the surface trough the upflow zone. The focusing of the fluids in the upflow zone can lead to the formation of massive sulphide deposits at the seafloor where the hot fluids react with the cold seawater. As the modified seawater goes further down towards the reaction zone it begins to react with Fe- bearing minerals such as olivine, pyroxene and pyrrhotite, leading to reducing conditions with high H_2 conditions (Tivey, 2007). Ion exchange reactions occur, such as albitization where anorthite is altered to albite and this will affect the concentrations of Ca and Na in the fluids (Tivey, 2007; Alt, 1995). The result of the processes that takes place in the recharge zone results in fluids that are slightly acidic, anoxic, rich in alkalis and poor in Mg relative to the starting seawater (Tivey, 2007). This fluid can leach sulphur and metals (e.g. Cu, Fe, Zn, Mn) as it percolates through the rock (Tivey, 2007; Alt, 1995). Chlorine in the form of the anion chloride is conservative trough the water-rock reactions and is a key component in the hydrothermal fluids, and as sulphate is precipitated, most of the remaining anions in the hydrothermal fluids are therefore present as chloro-complexes (German and Von Damm, 2006) There are few mineralogical sinks for chloride in the hydrothermal systems being phase separation the main process that controls the chloride concentrations (German and Von Damm, 2006).

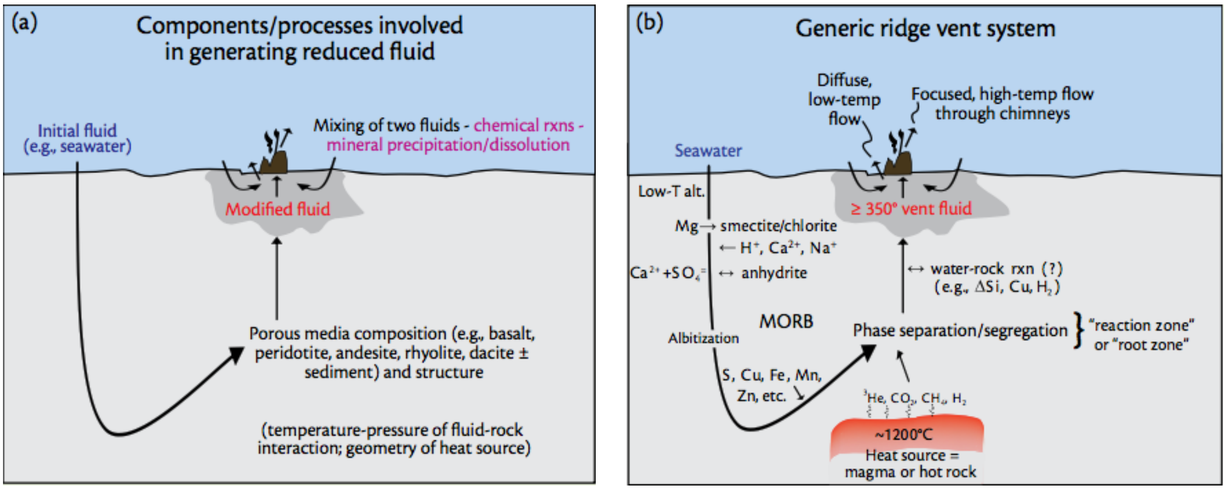

Figure 14: (a) This figure shows the components, processes and the path of ambient seawater trough the oceanic crust to make reduced hydrothermal fluids that then rise towards the seafloor and precipitate minerals as it mixes with seawater. (b) This figure explains the processes that take place as cold ambient seawater enters the crust and are progressively modified as the fluids migrate trough the oceanic crust, forming warm hydrothermal fluids that migrates towards the seafloor. Both figures are taken from Tivey, (2007).

4.3 Plumbing system

German and Von Damm, (2006) points to the importance of plumbing system as a fundamental difference while looking at vent fluids from hydrothermal systems at fast and slow spreading ridges while looking at intra field differences of vent fluid compositions. They point to the general difference between the ridges while looking at fluid composition at multiple vents in a vent fields is that at slow spreading ridges generally have a common fluid source that show compositional changes due to near surface processes, while at fast ridges vets that are spaced by a couple of meters can have different fluid sources. They point to that the explanation may be related to the depth the fluids are coming from, at slow ridges the fluids will come from a greater depth and be guided by fault planes or tectonic structures. At fast ridges the vent fields are fed from shallower heat sources and can therefore show greater variation between adjacent vents. Vent sites on slow spreading ridges appear to have longer longevity than at fast spreading ridges, based on the size of the structures and mound size (German and Von Damm, 2006). For hydrothermal activity spreading ridges to occur it is required the presence of a heat source in the form of either magma or newly solidified hot rock, exothermic reactions such as serpentinization (Lowell and Rona, 2002), a permeable medium that allows for circulation of fluids such as faults or fissures, and a fluid that reacts with the crust (Seawater) (Tivey, 2007). Hydrothermal outflow are most commonly found at the termination of single faults, or where multiple faults interact due to higher permeability and higher stress concentrations leading to active fracturing causing continual re-opening of fluid pathways (Curewitz and Karson, 1997).

4.4 Phase separation

At the typical depths for Seafloor hydrothermal systems (2500-3000 m) the two phase curve for seawater will normally not be intersected, but at shallow systems however the two phase curve may be intersected below the critical point and the fluids will begin to boil (Hannington, 2014). Depth controls what temperature is needed for phase separation, as greater depth requires higher temperatures to cause phase separation (German and Von Damm, 2006). The critical point for seawater is at 405°C at 300bar (Bischoff and Rosenbauer, 1985). For known vent systems that range from 800-3600 m depth needs a temperature of 297-433°C for phase separation to occur (German and Von Damm, 2006). If the hydrothermal fluids intersect the two phase curve under the critical point will separate vapour from the bulk liquid, if the two phase curve is intersected above the critical point it will result in separation of a brine from the liquids (Bischoff and Rosenbauer, 1985). During phase separation dissolved gases such as H_2S, H_2, CH_4, He and CO_2 will go into the less dense phase together with HCl and H_4SiO_4, transition metals and divalent cations like Ca^{2+} will get concentrated in the brine phase (Hannington, 2014; German and Von Damm, 2006).

4.5 Chimney growth

Seafloor hydrothermal chimneys follow, commonly, two distinct growth stages. The first is characterized by anhydrite precipitation as the hot vent fluids carrying Ca mix and heat sulphate-bearing seawater above 150°C creating a ring around the emanating fluids (Tivey, 1998), Once the anhydrite walls are in place, the vent fluids become insulated from the cooler seawater and stage two growth is initiated (Tivey and McDuff, 1990; Haymon, 1983). During stage two, sulphides start to precipitate by dissolving and replacing anhydrite during this stage the chimney is growing outwards with the precipitation of anhydrite, and inwards by precipitation of sulphides (Haymon, 1983). Anhydrite is unstable at seafloor temperatures and will dissolve (Jamieson et al., 2016), as the fluids migrate trough the vent chimney wall it can lower the temperature and initiate anhydrite corrosion that forms pores where sulphides can form (Los et al., 2016). Barite in hydrothermal systems is formed when hydrothermal fluids containing Ba that has been leached from rocks, and SO_4 from seawater mix so the fluids get supersaturated (Jamieson et al., 2016; Griffith et al., 2012) Unlike anhydrite barite has an extremely low solubility in seawater, which preserves the geochemical and morphological crystallization features (Jamieson et al., 2016). Copper-iron sulphides start to plate the inner walls and mixing of hydrothermal fluids and seawater across the porous walls results in deposition of zinc, copper-iron and iron sulphides in cracks and open spaces of the wall making the chimney less porous and enriched in metals (Tivey, 1998). Due to changes in thermal and chemical conditions in the chimney walls as the chimney ages, it results in the progressive development of sulphide zonation sequences (Haymon, 1983). The chimney can be divided into two zones based on mineral formation. In the interior of the chimneys temperatures are generally higher than the outer parts of the chimney as this is to a higher degree affected by mixing with seawater. The result is that you get mineral zonation in the chimney with high temperature minerals such as chalcopyrite in the interior, and lower temperature minerals such as sphalerite in the outer walls (Jamieson et al., 2016; Hannington et al., 1995; Tivey, 1998)

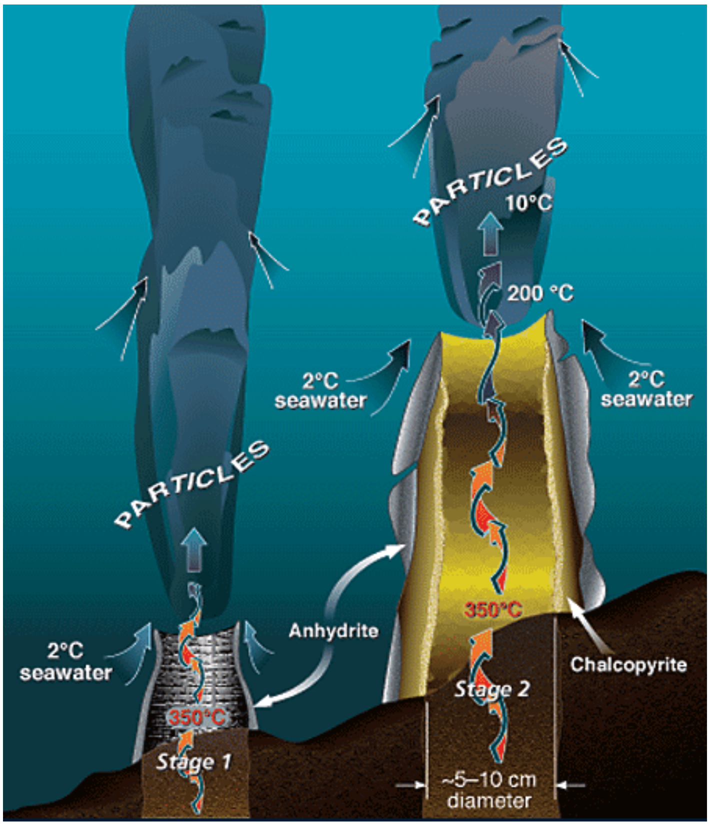

Figure 15: This figure illustrates the two stages of chimney growth as warm reduced hydrothermal fluids mixes with cold ambient seawater. During stage 1 of chimney growth warm hydrothermal fluids mixes with cold seawater rich in calcium and sulphate, which results in the formation of an anhydrite ring around the fluids. During stage 2 chalcopyrite starts to form on the inner chimney wall, and mixing between seawater and hydrothermal fluids in the chimney wall leads to formation of Zn, Cu-Fe and Fe sulphides in the wall which in turn decreases the porosity of the chimney and enriches it in metals (Tivey, 1998).

4.6 Isotope geochemistry

4.6.1 Strontium isotopes

Seawater has both Ca^{2+} and SO_4^{2-} and when it heats to more than 150°C anhydrite will precipitate, Ca^{2+} are present also in the hydrothermal fluids which makes it difficult to determine if the anhydrite is precipitated solely from seawater that was heated by hydrothermal fluids or by mixing by seawater and Ca^{2+} rich hydrothermal fluids (Tivey, 1998). Modern seawater has $^{87}Sr/^{86}Sr$ values of 0.07917 (Eickmann et al., 2014). Modern oceanic basalts show a scatter in the $^{87}Sr/^{86}Sr$ values that might be due to heterogeneity in the upper mantle and based on geochemical samples from fresh basalts and gabbroic intrusions it is suggested that the upper mantle lie within a range of 0.704±0.002 (Misra, 2012). Strontium is present both in hydrothermal fluids and in seawater however the two fluids show different isotopic ratios between the two isotopes ^{86}Sr and ^{87}Sr. Since strontium can take the place of Ca^{2+} in anhydrite's crystal lattice without any fractionation effects it is possible to determine if the source of strontium is the hydrothermal fluid, since it will have a higher isotopic ratio than seawater (Tivey, 1998; Misra, 2012).

4.6.2 Sulphur isotopes

Precipitated barite is similar with respect to the sulphur isotopic composition that it precipitated from, with a difference of less than 0.4‰ (Kuskabe and Robinson, 1977). In hydrothermal systems, sulfur in barite shows an isotopic signature that reflects the relative amount of sulfur incorporated from seawater SO_4 and/or from hydrothermal H_2S (Griffith et al., 2012). Seawater SO_4 has a $\delta^{34}S$ value of about 21,5‰, while the mantle has a value of 0‰ (Eickmann et al., 2014; Herzig et al., 1998; Misra, 2012; Kusakabe et al., 1990; De Ronde et al., 2003). $\delta^{34}S$ values of sulphates in hydrothermal systems that are around the seawater values will have values lower than 21,5‰ if there is contributions from the local oxidation of isotopically lighter vent fluid H_2S or sulfide minerals, and values higher than 21,5‰ indicate local reduction of seawater sulfate and isotopic enrichment of the residual sulfate (Shanks et al., 1995). Microbial reduction of sulfate could result in $\delta^{34}S$ values that are higher than that of seawater sulphate (Eickmann et al., 2014; Griffith et al., 2012). Oxidized hydrothermal H_2S has a $\delta^{34}S$ value of 1-2‰ (Griffith et al., 2012). During the progressive heating of seawater to temperatures around 150-200°C anhydrite is going to precipitate, and reduce the content of SO_4 (Shanks, 2001; Herzig et al., 1998) The remaining sulfate is then reduced to sulfide due to oxidation of ferrous Fe from minerals in the basalt, the variation in $\delta^{34}S$ comes from the mixing of reduced seawater with sulphur of basaltic origin with the various exchange reactions taking place between sulphate and sulphides and between sulphides (Herzig et al., 1998; Misra, 2012) and also bacterial reduction of sulphate to sulphide (Misra, 2012). There are many factors controlling the values in $\delta^{34}S$, such as temperature, source of the fluid and ratio of oxidised SO_4 to reduced H_2S (Ohmoto, 1972; Rye & Ohmoto, 1974; Misra, 2012).

4.6.3 Radiometric dating of barite

Barite has very low solubility making it resistant to weathering and preserving both the geochemical fingerprints of conditions of formation, as well as undisturbed isotopic decay (e.g. Jamieson et al., 2016). Radium has similar geochemical properties as barium, so when hydrothermal fluids carrying Ba mixes with seawater sulphate, radium will co-precipitate with barium in the barite crystals, while Ra parent isotopes (^{238}U that decays via ^{232}Th and ^{230}Th to form ^{228}Ra and ^{226}Ra respectively) are excluded from the barite crystal (De Ronde et al., 2005, 2011; Ditchburn et al., 2012; 2004; Jamieson et al., 2016). Activity ratios of ^{228}Th/^{228}Ra, and ^{228}Ra/^{226}Ra (Bq.Bq^{-1}) are used for dating in the age ranges of 0.3 to 12 years, and 3 to 35 years respectively, ^{226}Ra/Ba values is used for dating in the age ranges of 500 to 15 000 years (Ditchburn et al., 2012). These age ranges are very useful to date mineralization events in modern and active seafloor hydrothermal systems provided that the mineralization sequences are well constrained.

5 Results

5.1 Petrography and Mineralogy

A total of four rock samples have been taken from actively venting chimneys at Perle and Bruse in the Southern Mohns Ridge during the 2014 CGB Cruise. A total of 11 thin polished sections and 3 whole-rock powders were made covering the different textural and mineralogical aspects of the chimneys. Although within the same area and depth, the Perle og Bruse sites have distinct venting characteristics. While Perle vigorously vents clear bubble-rich fluids at ~248ºC, Bruse chimneys vent clear bubble-depleted fluids at approximately 242ºC (F.Marques; E. Reeves, personal communication) These observed differences have impact on the chimneys' mineralogy so that they will be described separately. Further North on the Mohns Ridge, and during the 2015 and 2016 CGB Cruise, four chimney samples were taken from Aegir hydrothermal system. Of these samples a total of 7 thin polished sections have been made covering the different textural aspects of the chimneys, and 5 representative whole-rock powders were prepared for chemical analyses. All abbreviations used are taken from Siivola and Schmid, 2007. SEM pictures is taken with backscatter or secondary element probe, and each picture illustrates the area from where the EDS microanalysis is taken from, each table is marked with what SEM picture it belongs to. For each thin section results from EDS analysis is followed by figures comprised of SEM pictures, and figures comprised of pictures taken in the microscope using transmittend or reflective light.

5.1.1 Perle Vent Field

The two rock samples GS14-ROV8-R01 and GS14-ROV8-Shuffle is taken from the Perle vent field produced four thin sections referenced as GS14-ROV8-R01 (A-1 to A-3), and GS14-ROV8-Shuffle. Whole-rock powders for chemical analysis were made from the GS14-ROV8-R01 sample.

5.1.1.1 Perle active chimney (GS14-ROV8-R1)

The sample was taken from an active hydrothermal chimney venting clear, bubble-rich fluids. The chimney shows a well-defined central orifice. Observations indicate that the white to darkish grey material is composed mostly of anhydrite and few sulphides.

Figure 16: Material from the Perle active chimney (GS14-ROV8-R01).

GS14-ROV8-R1A-1: Anhydrite is the dominant mineral phase in this thin section followed by sulphides. Anhydrite crystals are euhedral to subhedral and are up to 2.25 mm long. Their habits are tabular and acicular. The size of the crystals tends to be bigger in micro orifices and veins suggesting open-space crystal growth enabling larger crystal sizes. There is an estimate of 2-3 % sulphides in the sample. The main sulphide phase is pyrite followed by chalcopyrite and sphalerite. These sulphides occur predominantly aggregated in clusters that are around 0.8 mm thick. Textural observations suggest that pyrite and chalcopyrite formed first as both of these phases can be commonly found as inclusions in sphalerite. Other evidences also suggest that chalcopyrite co-precipitates with sphalerite.

Photo A:

shot nr:	Al	Si	S	Ca	Fe	Cu	Zn	Ni	Int
1	1,21	0,83	39,28		5,48	5,33	47,87		Sp
2		0,86	32,04		11,43		55,67		Sp
3			46,11	53,89					Anh
4			37,09				62,91		Sp
5			57,68		42,32				Py
6			56,68		43,32				Py
7			56,75		42,49			0,76	Py
8			58,65		41,35				Py

Photo B:

shot nr:	S	Ca	Fe	Cu	Int
1	47,41	52,59			Anh
2	56,72		40,21	3,07	Py
3	45,72	54,28			Anh

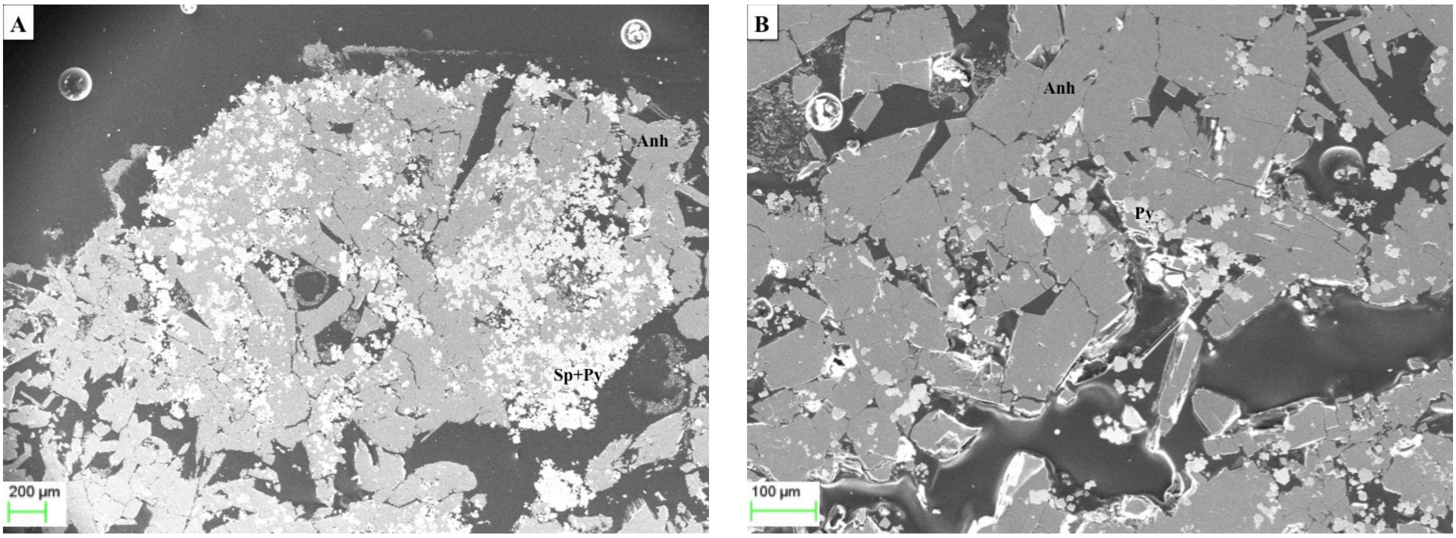

Figure 17: Both pictures A and B illustrate the relationship between the sulphates and sulphides of this sample. Sulphides are found precipitated on anhydrite crystals. Pyrite and sphalerite are found in the assemblages seen in the pictures. But Chalcopyrite is also found in the assemblages as illustrated by optical microscopy (See figure 18, picture C/D).

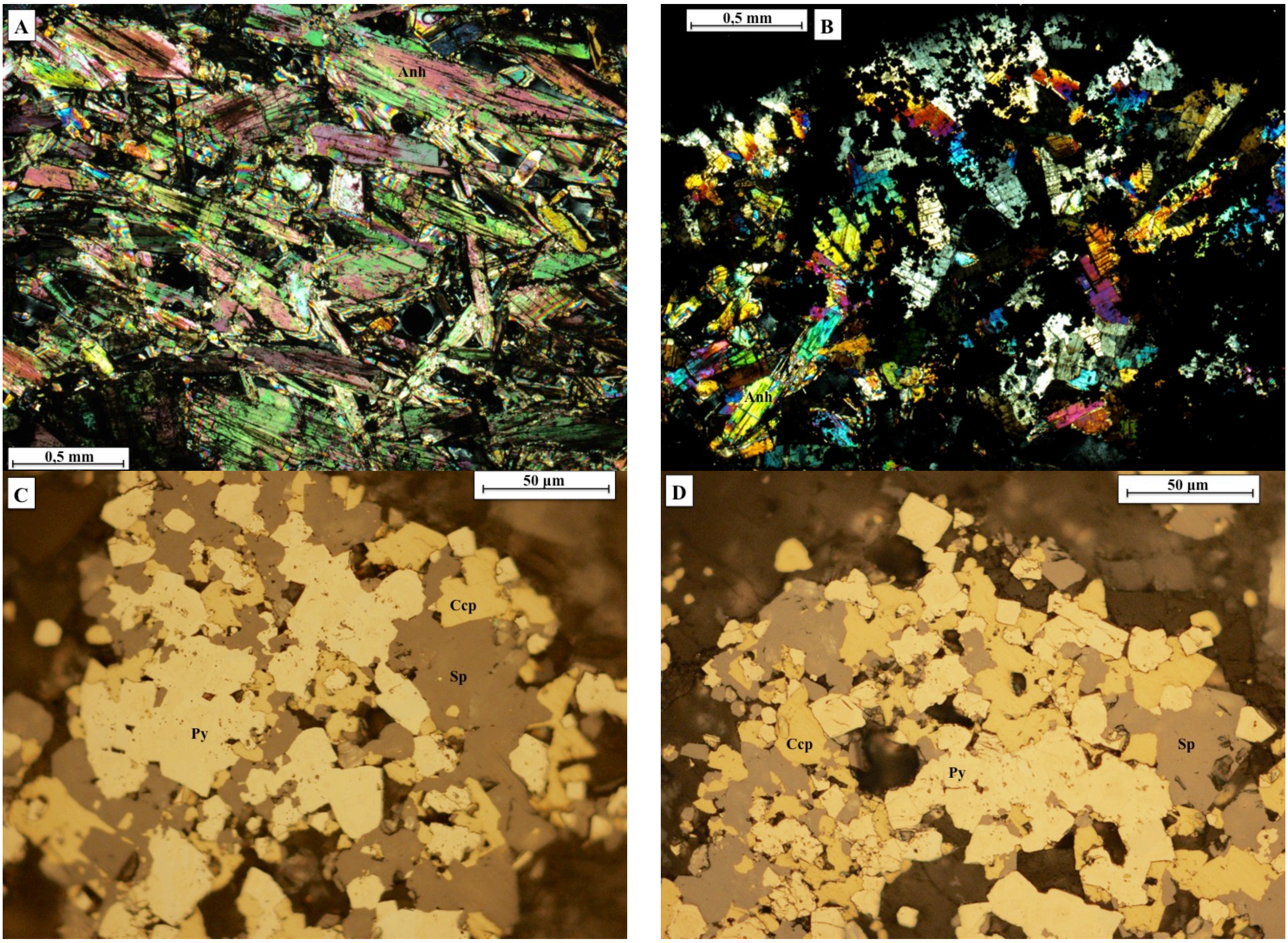

Figure 18: Picture A shows long euhedral to anhedral acicular anhydrite crystals. In picture B anhedral to subhedral anhydrite crystals covered by sulphide minerals as seen by the dark masses covering the anhydrite crystals. Picture C/D shows the sulphide phases found in the sample, which is dominated by pyrite, chalcopyrite and sphalerite.

GS14-ROV8-R1A-2: The main mineral phase in this thin section is anhydrite, followed by the sulphides. Anhydrite is euhedral tabular or acicular and the crystals can be up to 1.3 mm long. The sulphide content is here more abundant and estimated to be around 10%. The observed sulfide paragenesis in this thin section is similar to GS14-ROV8-R1A-1, but in this sample galena, a lead sulfide also is found. Galena is commonly found associated to sphalerite and can be found as inclusions inside the sphalerite crystals.

Photo A:

shot nr:	Na	S	Fe	Cu	Mo	Zn	Sc	Int
1		53,34	42,16		4,51			Py
2		34,04			6,32	59,64		Sp
3	0,5	40,6	28,67	27,75	2,49			Ccp
4		38,28				61,72		Sp
5		37,39	2,42			60,19		Sp
6		37,66				62,34		Sp
7		38,97	30,51	30,29			0,22	Ccp
8		38,36	6,98			54,66		Sp
9		52,93	42,4		4,67			Py
10		53,49	40,61	5,89				Py

Photo B:

shot nr:	Al	Si	S	Ca	Fe	Cu	Zn	V	P	Cd	Int
1	1,18	1,6	37,74		1,08		56,43			1,96	Sp
2			51,59	0,09	45,49	2,73			0,1		Py
3			45,02		31,84	7,55	15,43	0,08	0,08		Sp
4			53,99	0,14	44,15	1,45		0,15	0,13		Py
5			53,55		43,58	2,87					Py
6			51,7	0,12	43,59	4,39			0,2		Py
7			51,98	0,08	44,5	3,27			0,17		Py
8			33,75		1,18		62,59			2,48	Sp
9			52,14	0,1	46,26	1,29		0,11	0,09		Py
10			47,95		35,48	1,54	13,85		0,08	1,1	Sp
11			53,83	0,23	44,45	1,37			0,12		Py
12			53,12	0,1	45,74	0,85		0,19			Py

Photo C:

hot nr:	Mg	Al	Si	S	Ca	Sr	Fe	Cu	Zn	P	Cd	Re	Os	Int
1				43,2	56,8									Anh
2		0,01		43,4	55,9	0,67								Anh
3				33,8			0,99		61,1		4,03			Sp
4				52,2			45,1	2,5		0,15				Py
5			0,28	35,5	0,28		1,2		59		2,25	1,1	0,34	Sp
6				54,1	0,16		44	1,52		0,2				Py
7				35,1			0,96		61,8		2,12			Sp
8		0,02		34,1	0,24		0,68		62,6		2,34			Sp
9				36,3	0,1		29,7	34						Ccp
10	0,01	0,67	0,22	48,9	0,15		45,3	2,69	1,91	0,23				Py

Photo D:

shot nr:	Na	Mg	Al	Si	S	Cl	K	Ca	Sr	Fe	Cu	Zn	Cd	Pd	Int
1			2,74	0,36	34,5			3,1		28	31,3				Ccp
2			0,01	0,09	36,9					4,94		56,2	1,87		Sp
3			0,04		33,9					0,87		64	1,12		Sp
4					32,8					1,44		63,4	2,34		Sp
5			0,14		35					0,79		61,9	2,2		Sp
6			0,08		36,6					1,19		60,4	1,73		Sp
7					43			56,4	0,63						Anh
8					43,4			56,6							Anh
9					44,2			55,8							Anh
10	1,11	0,22	0,93	0,93	40,7	6,81	0,72	48,2						0,46	Anh

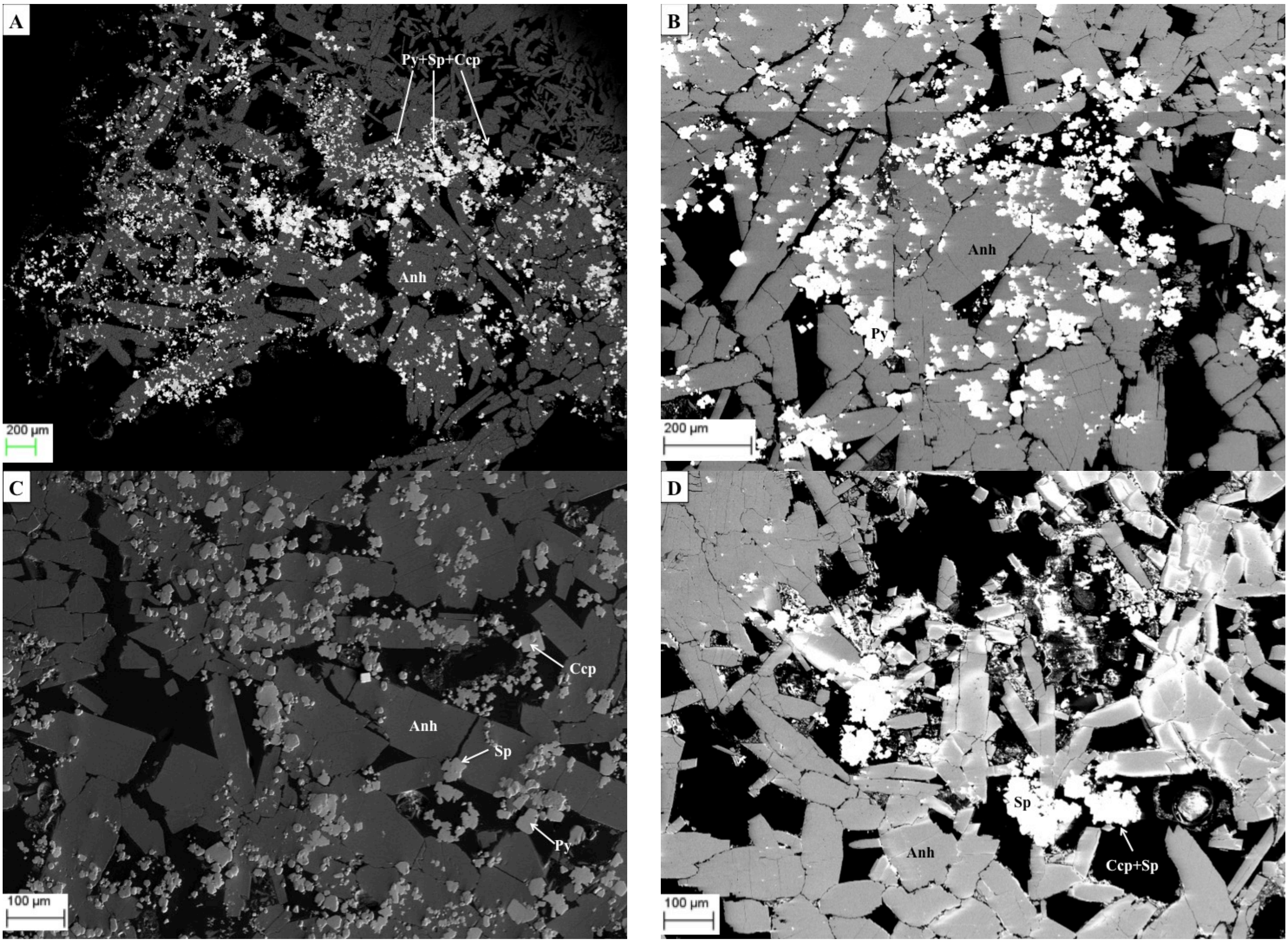

Figure 19: As seen in the thin section GS14-ROV8-R1A-1 pictures A,B,C,D illustrate the same relationship between the sulphate anhydrite and the sulphide phases. Pyrite, chalclopyrite and sphalerite were determined to be amongst the sulphide phases. From optical microscopy small amounts of galena was also observed.

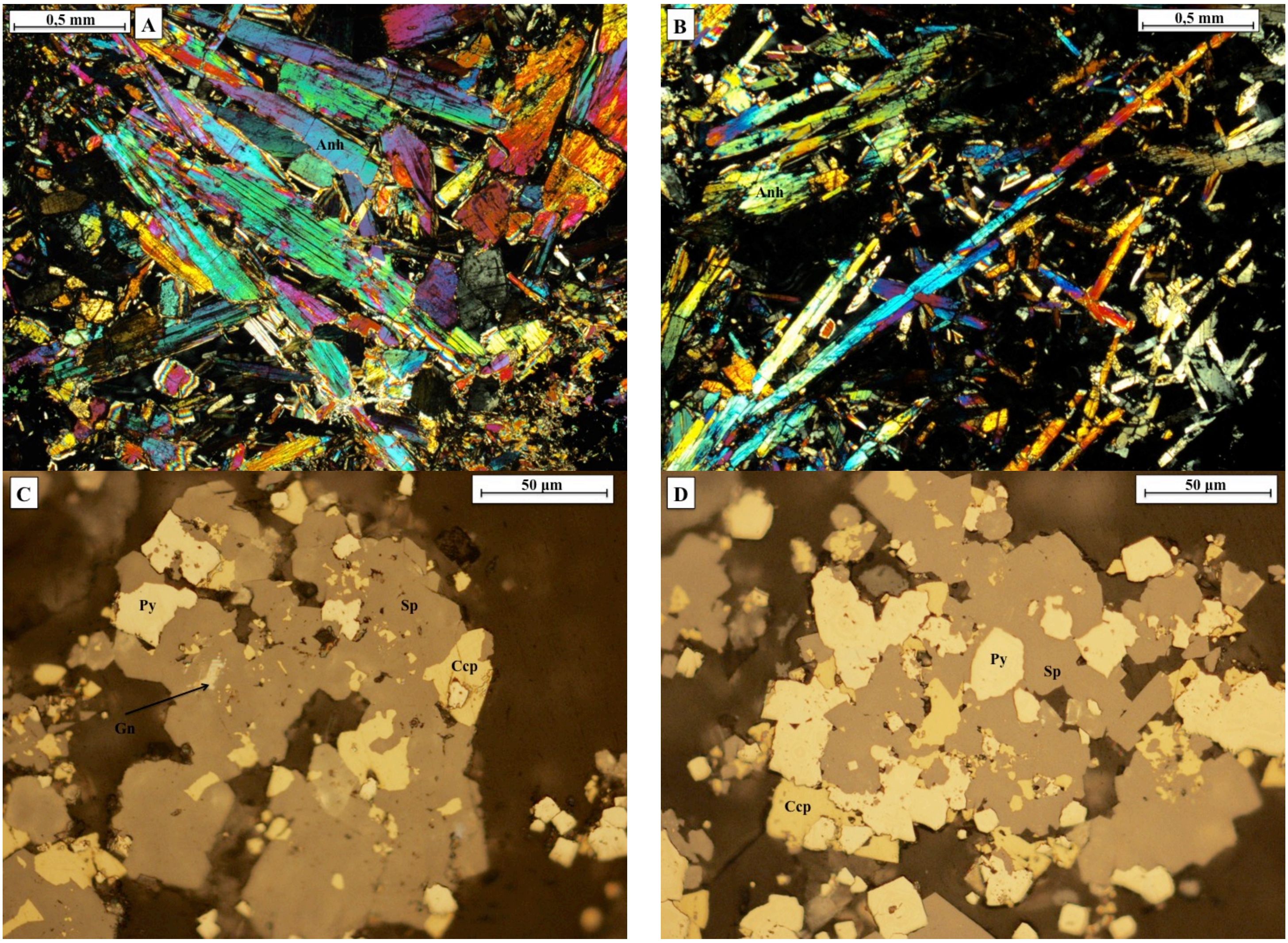

Figure 20: Picture A and B shows euhedral to subhedral anhydrite crystals, which are tabular or acicular. Picture C and D shows the sulphide phases in this thin section with pyrite, chalcopyrite, sphalerite and small amounts of galena.

GS14-ROV8-R1A-3: The main mineral phase in this thin section is anhydrite followed by sulphides and small amounts of barite mixed with silica. The anhydrite is euhedral tabular or acicular. The crystals can be up to 2.6 mm long. The sulphide content is estimated to be less than 1%. The dominant sulphide phase in this sample is pyrite followed by sphalerite and chalcopyrite. The pyrite crystals are rounded and up to 40 micron thick. The relationship between the sulphide phases in this thin section is similar to GS14-ROV8-R1A-1.

Photo A:

shot nr:	Al	Si	S	Cl	Ca	Fe	Cu	Mo	Zn	Int
1			37,48			28,28	34,24			Ccp
2			46,17		53,83					Anh
3			46,21		53,79					Anh
4			49,72		50,28					Anh
5			45,17		54,83					Anh
6			54,47	21,8	23,72					Anh
7	0,98	2,73	50,56		0,91	33,45			11,38	Sp
8			41,67		0,41	10,31			47,61	Sp
9			45,74		54,26					Anh
10			51,32			40,27		8,41		Py

Photo B:

shot nr:	Mg	Si	S	Cl	Ca	Ba	Fe	Int
1	1,05	56,65	10,92		3,23	28,15		Si
2	1,72	22,84	17,87		5,36	48,07	4,14	Brt
3	1,41	27,82	18,5		5,83	46,44		Brt
4		77,72	6,72		2,3	13,27		Si
5			45,61		54,39			Anh
6			45,95		54,05			Anh
7			18,03	16,38		65,59		Brt
8		0,58	46,28		53,13			Anh

Photo C:

shot nr:	Mg	Al	Si	S	Cl	Ca	Ba	Fe	Zn	Int
1	2,09		8,13	28,47	2,74	16,35	42,22			Brt
2		6,2	15,92	20,23	3,1	15,44	39,12			Brt
3			1,23	26,14	2,55	16,17	9,37	18,97	25,58	Sp
4				45,59		54,41				Anh
5	23,06	20,61	36,98	9,97	9,39					Si
6				55,31				44,69		Py
7			0,98	45,98		53,04				Anh
8				46,25		53,75				Anh

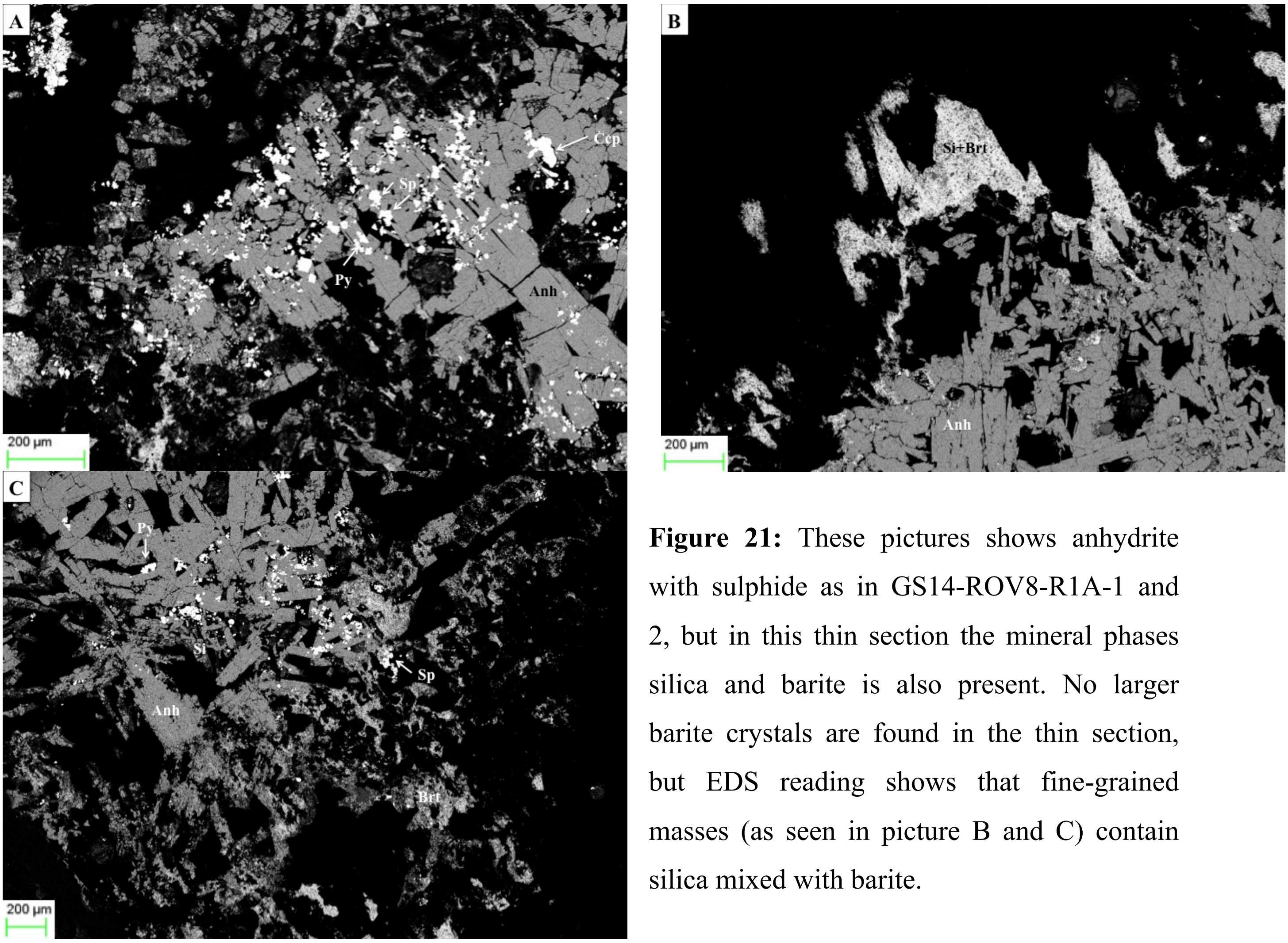

Figure 21: These pictures shows anhydrite with sulphide as in GS14-ROV8-R1A-1 and 2, but in this thin section the mineral phases silica and barite is also present. No larger barite crystals are found in the thin section, but EDS reading shows that fine-grained masses (as seen in picture B and C) contain silica mixed with barite.

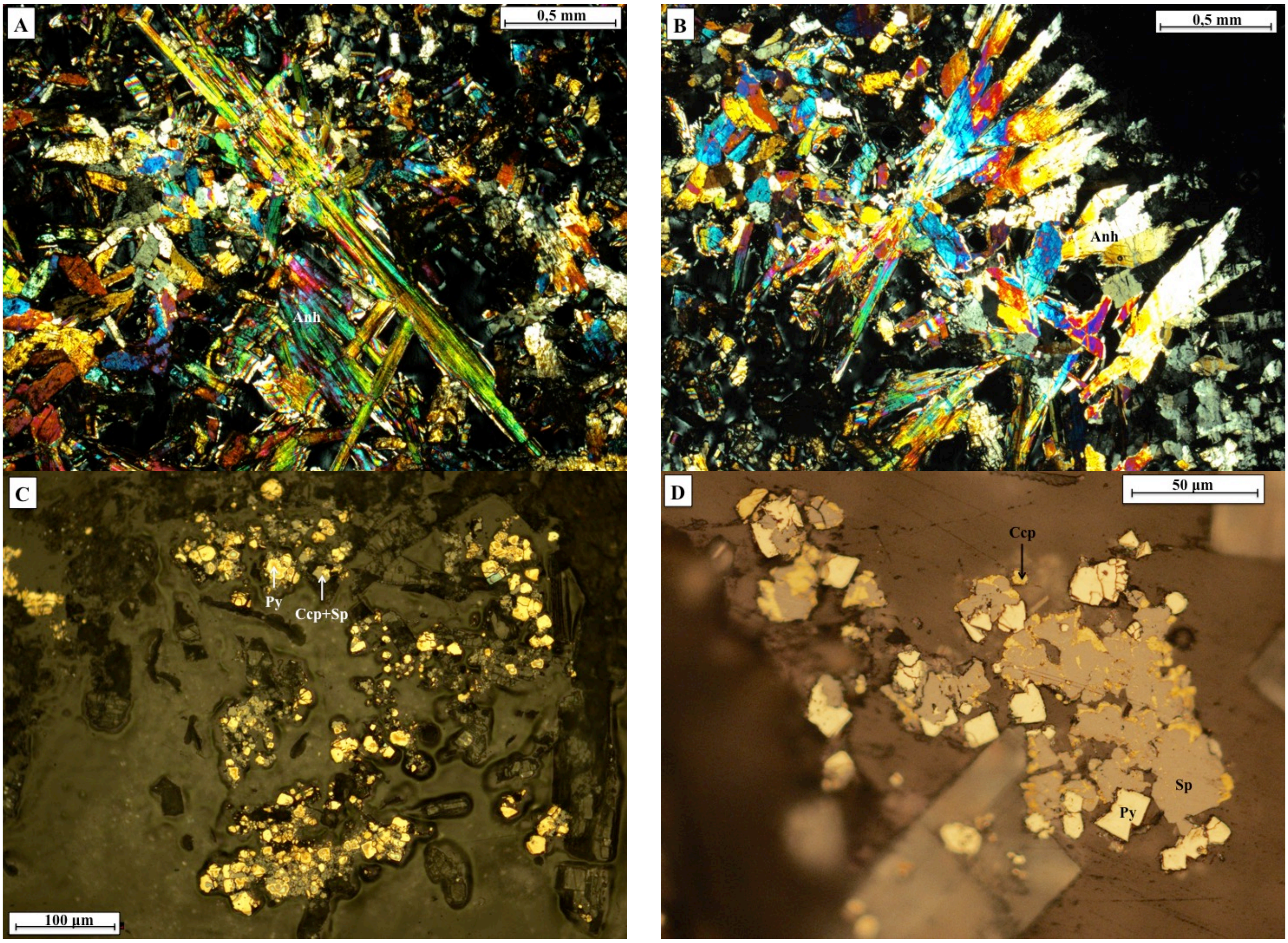

Figure 22: Picture A and B shows euhedral to subhedral anhydrite crystals, which are tabular or acicular. Picture C and B shows the sulphide phases of the thin section, which are pyrite, chalcopyrite and sphalerite.

5.1.1.2 Perle mound rubble (GS14-ROV8-Shuffle)

At the base of Perle's actively venting chimneys, hydrothermal mound material with inner temperatures around 95ºC (F. Marques, personal communication) was sampled using the ROV's shuffle box. The material is fresh, porous, has a greyish colour, and is mainly composed of sulphate.

Figure 23: Photo of the sampled material from the Perle mound. Sample sizes vary, and amongst the finer particles larger pieces that resemble clasts from collapsed chimneys are found.

<u>GS14-ROV8-Shuffle:</u> Barite is the dominant sulfate mineral in this sample followed by minor amounts of sulphide and silica. The barite crystals are euhedral and grow either as radiating clusters of up to 200 μm long acicular or dendritic crystals, or as large tabular crystals in micro orifices or veins that are up to 3.4 mm long. Varying thickness of the thin polished sections results in the barite crystals showing a large range of interference colours in crossed polars, from grey to yellow/orange to purple and greenish blue. Sulphides are scarce in the sample, and occupy less than 1 % of the surface area. Nonetheless, the sulphide phases found are pyrite, chalcopyrite and sphalerite. It is not possible to see the textural relation between the sulphides as the sulphide phases are small, isolated crystals but they share similarities to the chimney sample GS14-ROV8-R1A-1.

Photo A:

shot nr:	Mg	Al	Si	S	Cl	K	Ca	Sr	Ba	Fe	Mn	Int
1	0,17	0,47	8,72	16,84	0,61	0,09	3,15		69,28	0,66		Brt
2	0,34	1,16	58,12	6,09	0,6		5,98		26,96		0,76	Si
3	0,39	8,94	31,99	10,7	1,07		5,15		41,75			Brt
4		0,1		19,39				1,03	79,49			Brt
5				19,51			0,18	5,33	74,98			Brt
6	0,71	1,17	10,91	17,84	2,47	0,32	4,7		60,23	1,65		Brt
7				20,53				1,91	77,55			Brt
8				19,33			0,17	4,67	75,83			Brt

Photo B:

shot nr:	S	Sr	Ba	Int
1	23,57		76,43	Brt
2	22,2		77,8	Brt
3	22,35		77,65	Brt
4	22,32	4,1	73,58	Brt
5	23,49		76,51	Brt

Photo C:

shot nr:	Na	Mg	Al	Si	S	Cl	Ca	Ba	Ti	Fe	Int
1				65,75	9,19		2,02	19,76		3,28	Si
2		1,79		24,67	16,75		4,63	43,68		8,49	Brt
3		2,67		24,79	16,45		8,31	42,13		5,66	Brt
4		2,5	1,09	22,2	18,55		4,46	47,73		3,46	Brt
5		1,34	2,18	19,67	16,52		9,64	43,82		6,84	Brt
6				61,32	9,81		2,01	26,86			Si
7	2,11			21,23	19,54		4,23	52,09	0,8		Brt
8			1,32	30,63	17,78		5,15	43,42	1,7		Brt

Photo D:

shot nr:	Na	Mg	Al	Si	S	Cl	K	Ca	Ba	Ti	Fe	Zn	Int
1		1,81	1,16	29,96	16,18			5,12	45,78				Brt
2		1,96	0,98	28,46	15,03			3,89	41,47	2,81	5,42		Brt
3		1,57	1,81	8	16,5		1,19	18,67	48,94		3,33		Brt
4					4,34		1,75	14,17	79,74				Brt
5	4,83		5,85	27,47	13,52			11,45	34,84	2,05			Brt
6				10,28	24,43	4,96			60,33				Brt
7				18,89	12,01	6,72			62,39				Brt
8			1,12	51,19	10,54			5,53	29,34			2,29	Si
9		1,14	1,27	20,91	17,53			2,43	42,64	4,51	9,57		Brt

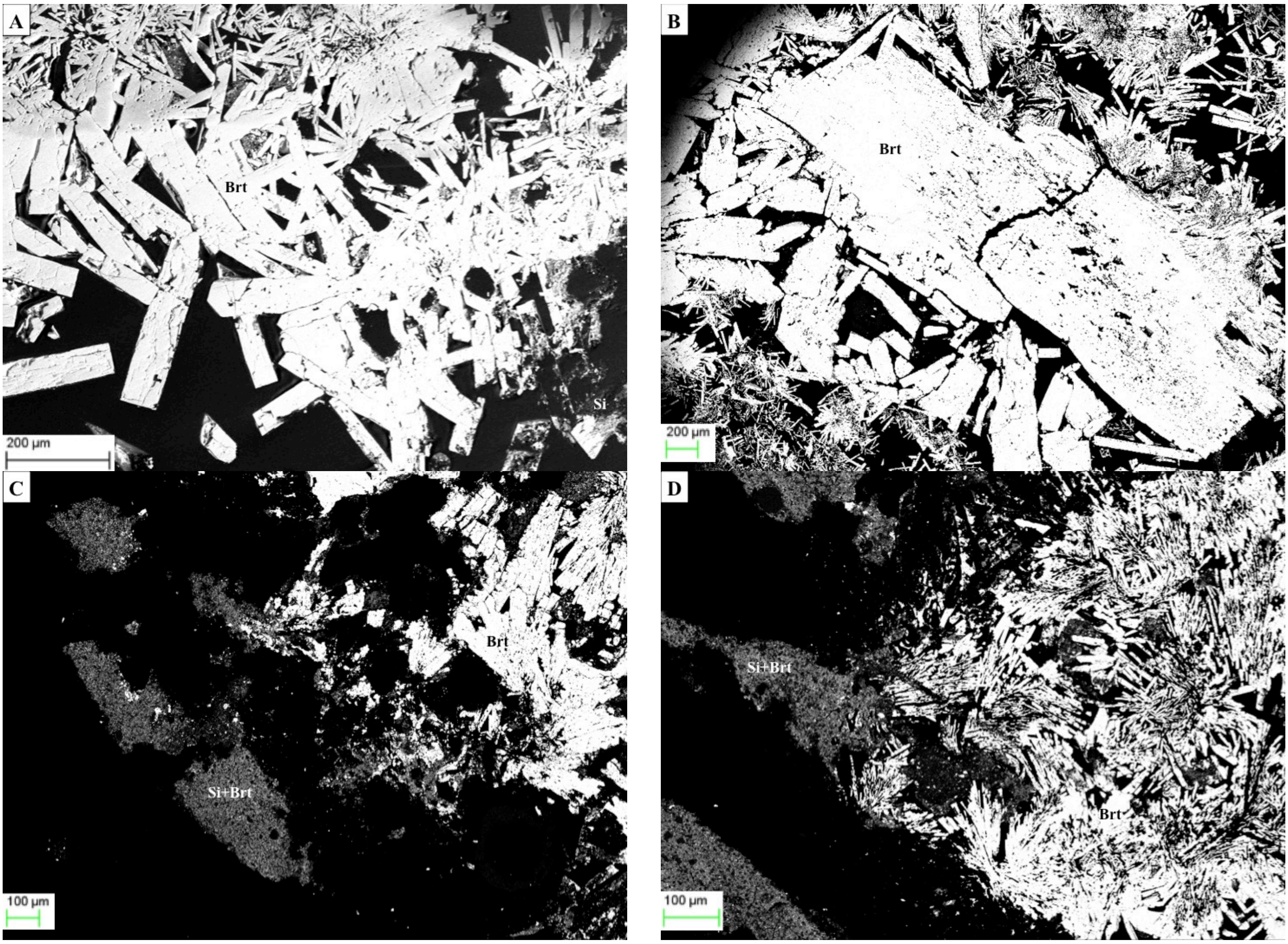

Figure 24: From the SEM pictures it is possible to see only the barite and silica, the small amounts of sulphide is very difficult to localize amongst the barite crystals. Picture A and B shows acicular and tabular barite crystals, picture C and D shows masses of silica mixed with barite. In picture D it is also small barite crystals that are dendritic.

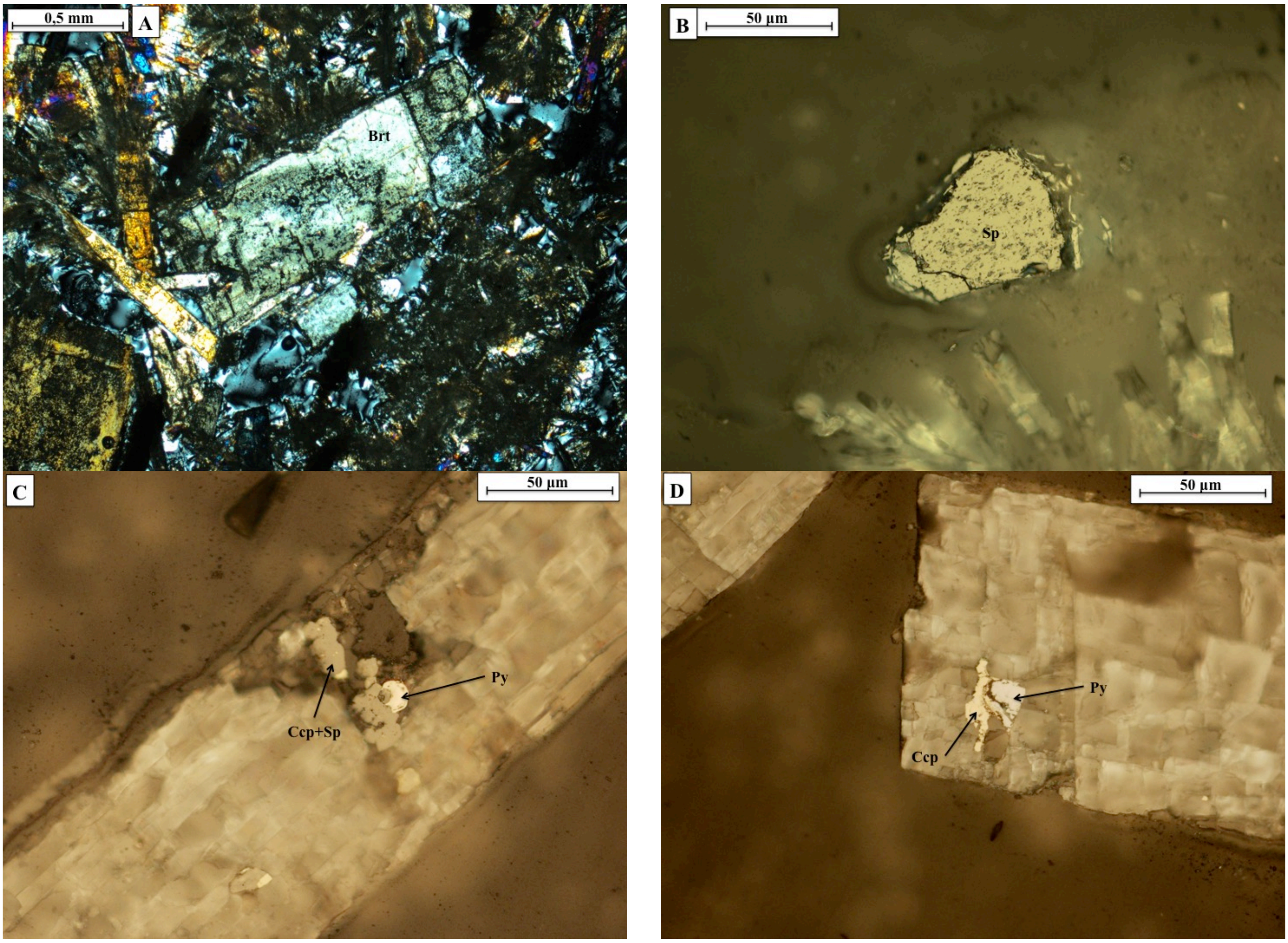

Figure 25: Picture A shows a large tabular barite crystal surrounded by smaller acicular and tabular crystals. Picture B,C and D shows the sulphide phases found in this thin section, which are pyrite, chalcopyrite and sphalerite.

5.1.2 Bruse vent field

Samples GS14-ROV7B-R01 and GS14-ROV7B-R02 were taken from the Bruse area. From these samples a total of 7 thin sections were made, with a total of 3 thin sections for the GS14-ROV7B-R01 sample, and 4 for GS14-ROV7B-R02. Whole-rock powders were made from both samples.

5.1.2.1 Feeder system (GS14-ROV7B-R1)

Sample GS14-ROV7B-R1 was taken from a dark-brown linear ridge extending towards the chimney GS14-ROV7B-R2. This structure may represent a feeding conduit or a hardened fallen chimney although its shape and well-preserved interior suggesting on-going hydrothermal activity agrees with the feeding conduit. The hydrothermal material consists of outer material that is whitish grey (GS14-ROV7B-R1A) making a sharp contrast with its interior that is dark in colour (GS14-ROV7B-R1B).

Figure 26: Picture of the sampled feeder system. In the big piece in the upper left of the frame it is clearly seen that there is a sharp contrast in colour between the outer parts that is light in colour, and the darker interior.

GS14-ROV7B-R1A-1: The dominant mineral phase is barite, followed by sulphides. The barite crystals are euhedral, and grow either as radiating clusters of acicular or dendritic crystals, or as isolated large tabular crystals in veins or micro orifices. The radiating crystals are up to 70 µm long. The larger isolated crystals are up to 500 µm long. The dominant sulphide phase is pyrite followed by chalcopyrite, sphalerite and covellite. There is very little sulphide in the sample, covering less than 1% of the surface area. The sulphide crystals appear to be partly dissolved. The largest pyrite crystals are up to 50 µm thick. Pyrite and chalcopyrite formed first followed by sphalerite as both of these mineral phases can be found as inclusions inside sphalerite. Chalcopyrite is also found spatially associated with sphalerite. Covellite formed last, replacing chalcopyrite.

Photo A:

shot nr:	Na	Mg	Al	Si	S	Cl	K	Ca	Cr	Sr	Ba	Int
1				64,02		24,36			11,62			Si
2				2,2	26,1						71,7	Brt
3	1,32	0,86	36,39	59,86		1,57						Si
4	2,71		1,9	89,5		4,21	1,68					Si
5					23,21			0,53			76,26	Brt
6					22,57					3,68	73,74	Brt

Photo B:

shot nr:	S	Cl	Sr	Ba	Int
1	22,7			77,3	Brt
2	20,31	2,46		77,22	Brt
3	22,68			77,32	Brt
4	22,39			77,61	Brt
5	23,89			76,11	Brt
6	22,87			77,13	Brt
7	23,82			76,18	Brt
8	22,28			77,72	Brt
9	22,51			77,49	Brt
10	22,16		4,54	73,3	Brt

Photo C:

shot nr:	Mg	Si	S	Cl	Ba	Fe	Cu	Zn	Int
1		1,36	39,12			1,11		58,41	Sp
2			23,95		76,05				Brt
3		1,52	41,8			23,46	33,22		Ccp
4	1,27	7,73	21,87		69,13				Brt
5			41,49			25,45	33,06		Ccp
6			21,64		78,36				Brt
7			23,09		76,91				Brt
8		1,82	35,21		11,5	5,25	14,97	31,26	Sp
9			40,15					59,85	Sp
10			57,53			42,47			Py
11			58,36			41,64			Py
12			57,08			42,92			Py

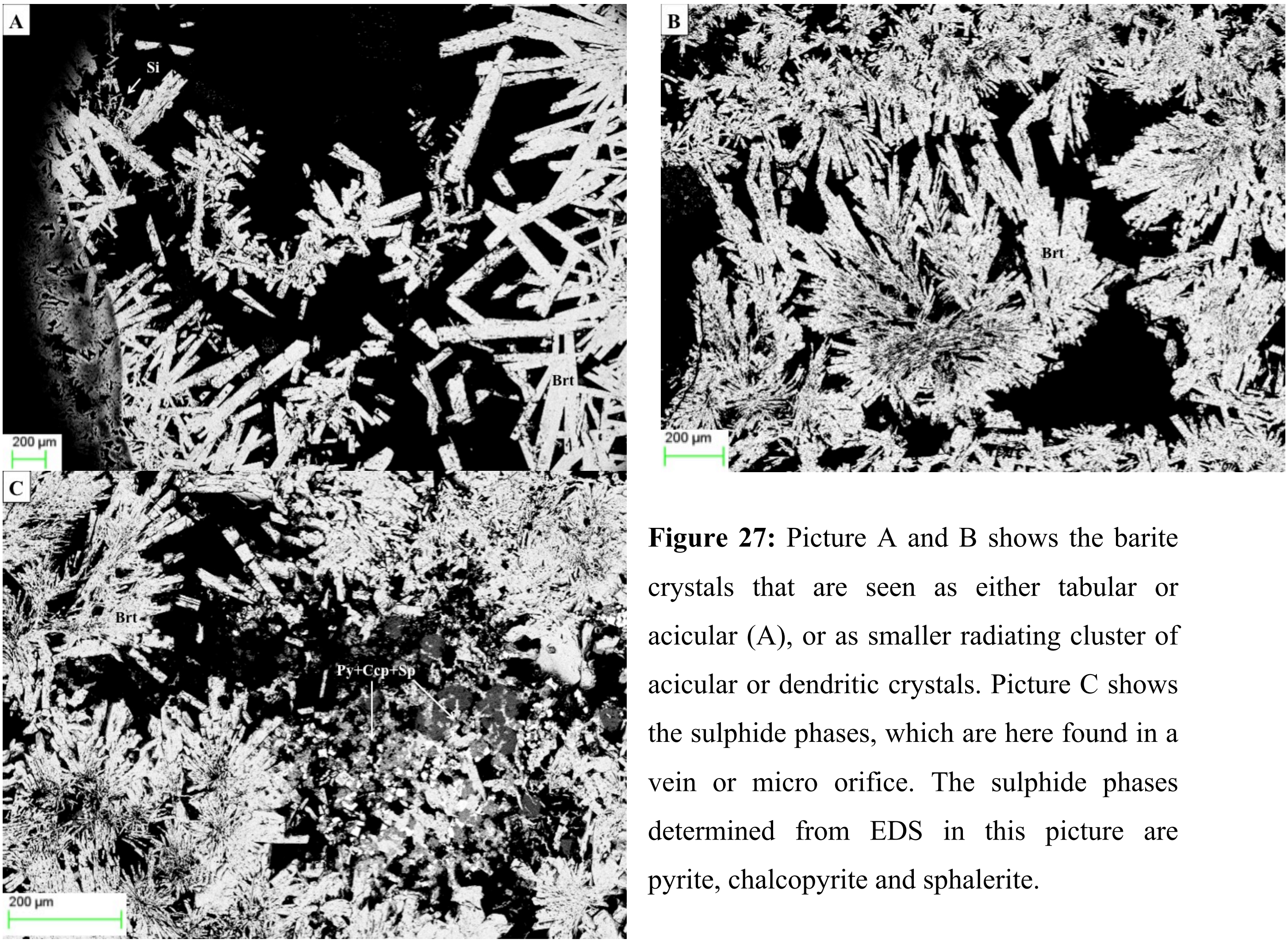

Figure 27: Picture A and B shows the barite crystals that are seen as either tabular or acicular (A), or as smaller radiating cluster of acicular or dendritic crystals. Picture C shows the sulphide phases, which are here found in a vein or micro orifice. The sulphide phases determined from EDS in this picture are pyrite, chalcopyrite and sphalerite.

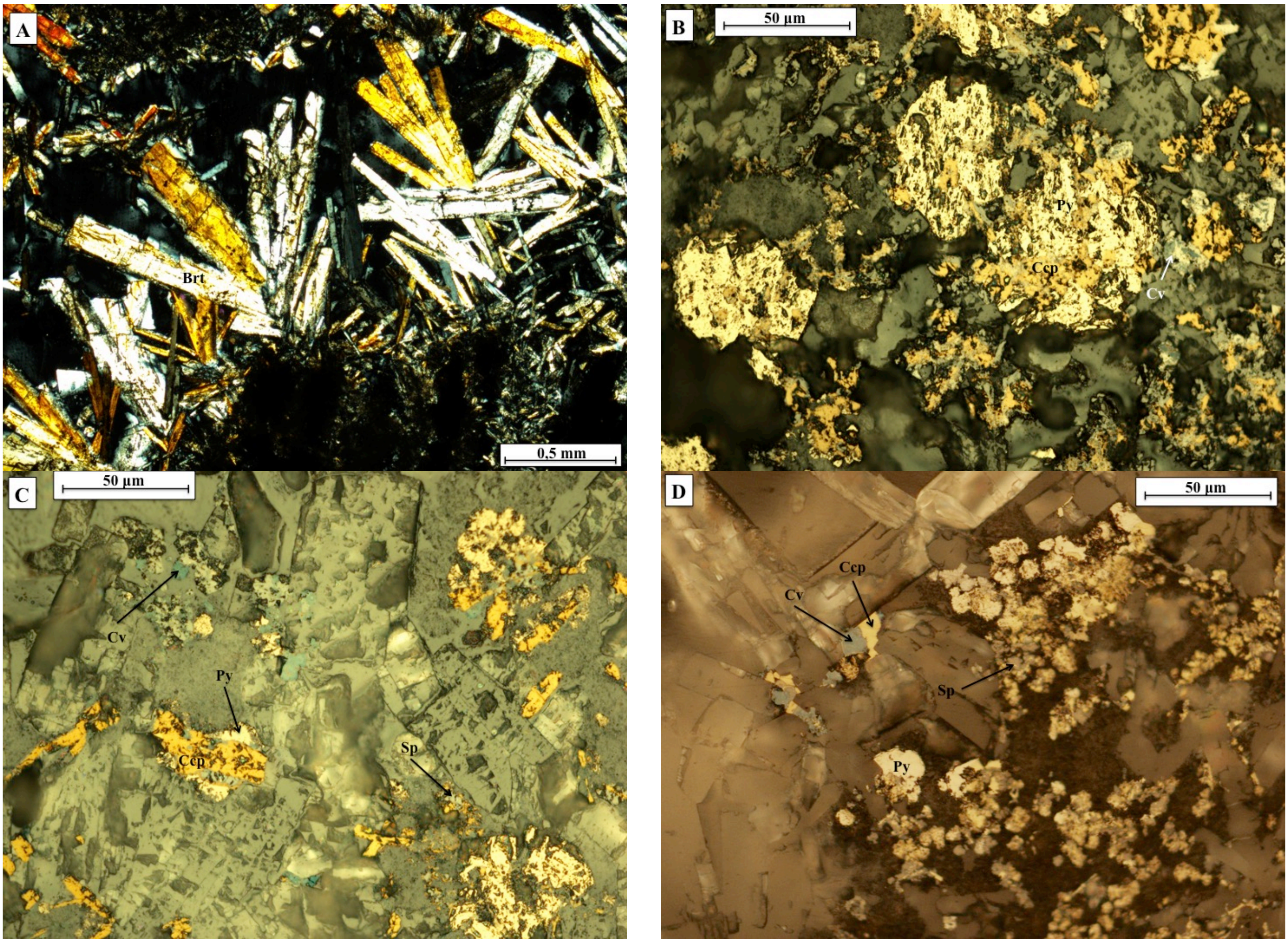

Figure 28: Picture A shows large euhedral barite crystals found in veins and micro orifices. B,C and D shows anhedral pyrite and chalcopyrite that are partly dissolved and minor amounts of covellite formed from reworking of chalcopyrite.

GS14-ROV7B-R1A-2: The dominant mineral phase in this sample is barite followed by sulphide. The barite is euhedral tabular and grows either as single large crystals in veins or micro orifices, or as radiating clusters of dendritic or acicular crystals. The radiating crystals are around 50 μm long, the larger single ones are up to 400 μm long. Sulphides occupy less than 1% surface in the thin section. The relation between the sulphide phases is similar to GS14-ROV7B-RA-1. The pyrite crystals are rounded and up to 20 μm thick.

Photo A:

hot nr:	Na	Mg	Al	Si	S	Cl	K	Fe	Cu	Tc	V	Ag	Int
1			0,02	2,26	50,55			42,83	4,17		0,16		Py
2	0,53		0,02		52,57			46,06	0,82				Py
3	0,60			0,17	52,36		0,11	45,93	0,84				Py
4	0,30				53,70			46,00					Py
5	0,79	1,28	19,33	65,76	2,82	0,83		1,19	5,59	2,41			Si
6		0,18	2,17	20,77	36,83		0,27	28,75	11,04				Ccp
7	0,30			0,59	54,29			44,83					Py
8	1,60	1,56	23,76	64,45	2,39	1,01	0,85		4,38				Si
9				0,43	46,99	1,00		29,61	20,72			1,24	Ccp
10					52,17			43,48	4,35				Py

Photo B:

hot nr:	Na	Mg	Al	Si	S	Cl	K	Ca	Ba	Fe	Cu	Zn	Cd	Pb	Int
1			0,05											99,95	Gn
2														100	Gn
3				0,48	19,53			1,10	78,89						Brt
4			0,68	2,36	19,45	9,58		0,53	67,40						Brt
5			0,51	1,97	17,59	2,34		0,31	77,27						Brt
6					31,83					0,70		63,17	4,30		Sp
7					33,21					5,25		58,09	3,45		Sp
8					31,87					0,89		64,68	2,56		Sp
9					31,10					0,90		64,40	3,60		Sp
10	2,52	1,04	28,66	59,59	1,43	1,21	1,19			0,94	3,43				Si

Photo C:

shot nr:	Na	Mg	Al	Si	S	Cl	K	Ca	Sr	Ba	Fe	Int
1	0,88	1,47	28,97	66,54		1,38	0,76					Si
2	1,22	3,20	20,37	64,63	1,47	1,16	1,79			4,52	1,63	Si
3	1,08	0,92	18,60	76,50		1,03	0,74				1,12	Si
4					18,85				3,25	77,90		Brt
5					19,91				1,92	78,16		Brt
6			0,08	0,80	4,54		0,36	0,31		93,91		Brt
7					18,44				1,81	79,74		Brt

Photo D:

shot nr:	Na	Mg	Al	Si	S	Cl	K	Ca	Sr	Ba	Int
1	1,47				17,95		0,19	0,25	1,46	78,68	Brt
2			0,22	1,81	17,99	1,35		0,37		78,26	Brt
3			0,86	3,80	17,91	9,42		2,26		65,76	Brt
4				1,28	17,66	9,66		2,23		69,16	Brt
5	1,74	1,53	34,35	58,69		2,11	1,58				Si
6	2,44	1,27	28,77	63,96		2,04	1,15	0,38			SI
7	1,37	1,57	13,95	80,95		2,15					Si
8		2,73	35,24	61,06		0,97					Si
9					18,49			0,40	3,50	77,61	Brt
10					18,45			0,42	2,86	78,27	Brt

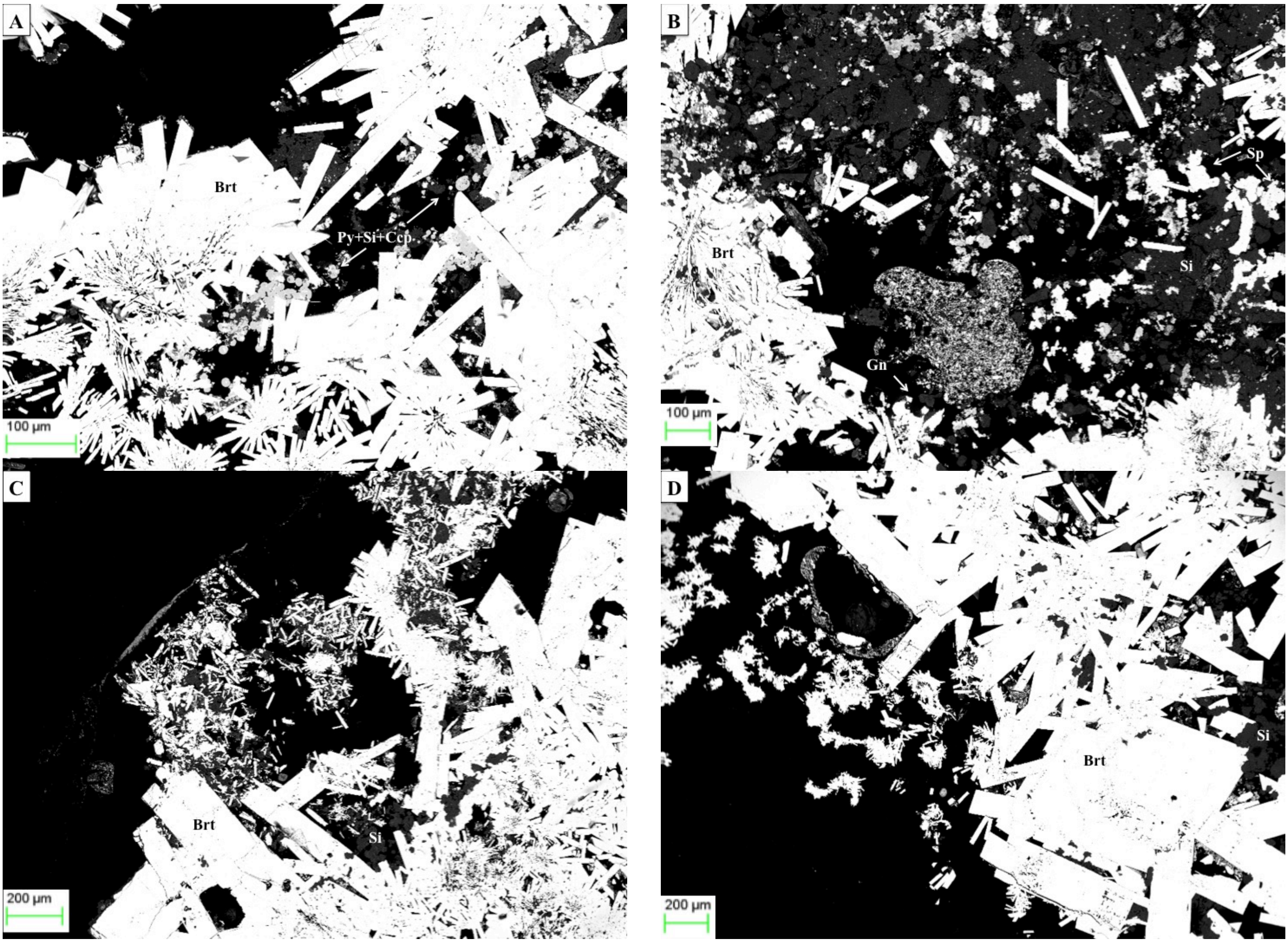

Figure 29: Picture A shows large tabular or smaller acicular barite crystals with pyrite, chalcopyrite and silica precipitated in the pore space. B shows sphalerite and galena amongst the silica and barite crystals. C and D show barite crystals and small amounts of silica in the pore spaces.

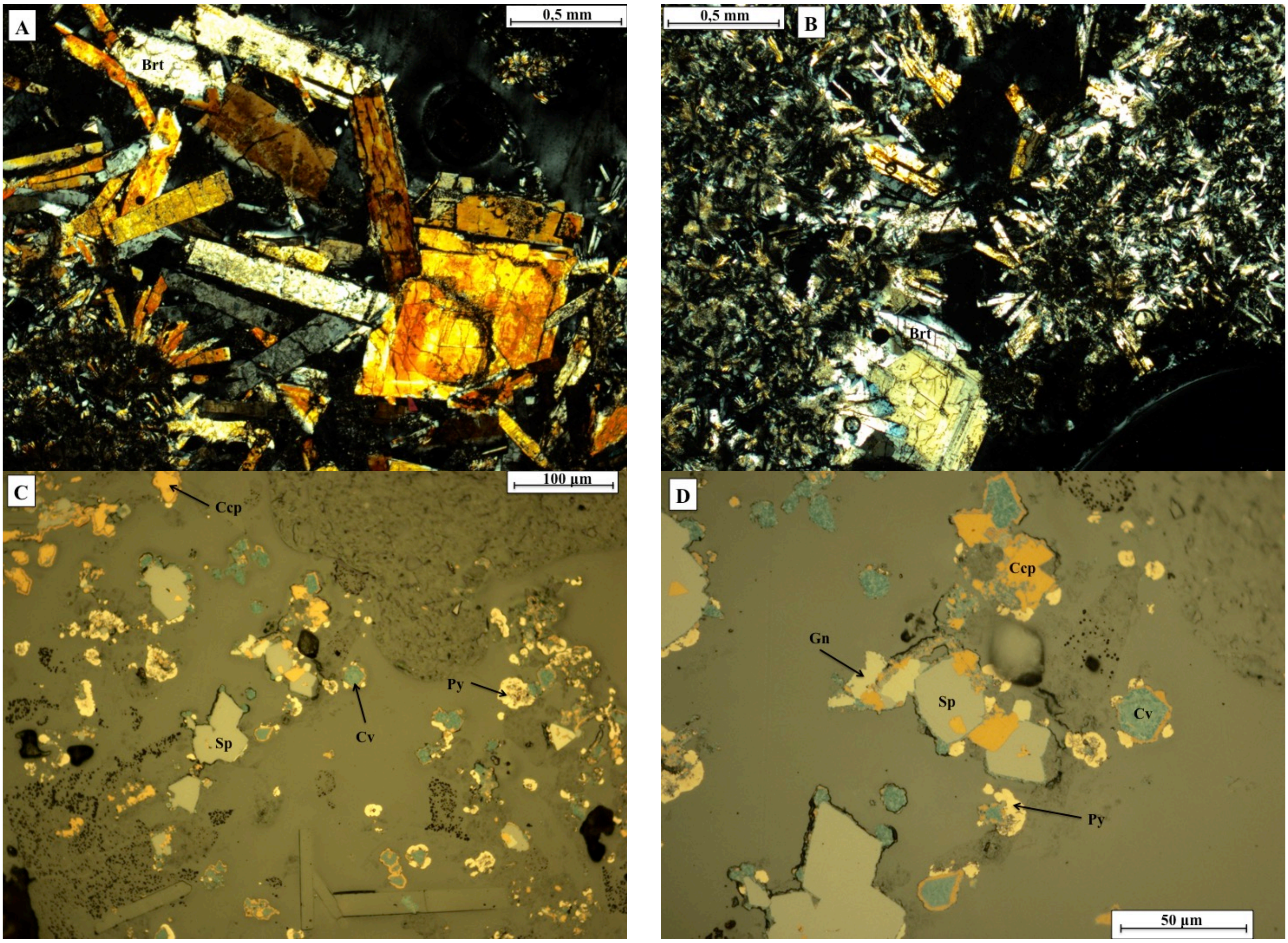

Figure 30: Picture A and B shows large barite crystals formed veins or micro orifices. Picture C shows the sulphide phases sphalerite, pyrite, chalcopyrite and covellite. D shows the same sulphide phases with the addition of galena. This picture clearly shows the replacement of chalcopyrite by covellite.

GS14-ROV7B-R1B: Barite is the main mineral phase found in this sample followed by sulphides. Barite crystals are euhedral, tabular and grow in radiating clusters of dendritic or acicular crystals. The crystals are up to 300 μm long, the largest crystals are found in veins or micro orifices. The main sulphide phase in the sample is pyrite followed by sphalerite, chalcopyrite, covellite and galena. There is an estimate of 4-5% sulphides in the sample, slightly superior to previous samples and conferring the visible dark colour in hand specimen. The pyrite crystals are up to 40 μm and show rounded rims. The pyrite and chalcopyrite seem to be the first sulfides to precipitate followed by sphalerite that commonly rims pyrite and chalcopyrite. The occurrence of galena is associated with sphalerite. Late covellite replaces chalcopyrite.

Photo A:

shot nr:	Mg	Al	Si	S	K	Ca	Sr	Ba	Mo	Int
1				22,35				77,65		Brt
2				20,99		0,96	4,33	70,55	3,17	Brt
3				23,7				76,3		Brt
4				22,2			3,36	74,44		Brt
5				22,72				77,28		Brt
6				21,7				78,3		Brt
7				22,58				77,42		Brt
8	1	33,78	61,52		3,7					Si

Photo B:

hot nr:	Al	Si	S	K	Ca	Sr	Ba	Fe	Cu	Mo	Zn	Cd	Int
1			20,8		0,61	3,25	73			2,29			Brt
2			23				77						Brt
3			36,9	0,18							59,1	3,8	Sp
4			37,4					1,4			57,9	3,35	Sp
5			40,8					26,8	32,4				Ccp
6			39					28,4	32,6				Ccp
7	0,52	7,35	36,2					26,2	29,8				Ccp

Photo C:

shot nr:	Si	S	Cl	K	Sr	Ba	Fe	Cu	Zn	Cd	Int
1	10,53	32,6	9,65			36,25	10,96				Brt
2	42,22	48,85	8,93								Si
3		22,75			2,43	74,82					Brt
4	0,84	35,32		0,18			1,07		59,58	3,02	Sp
5	78,6	15,11							6,29		Si
6	96,72	3,28									Si
7		38,86					26,01	35,13			Ccp
8		38,88					25	29,58	6,53		Ccp

Photo D:

shot nr:	Si	S	Cl	K	Ba	Fe	Cu	Zn	Cd	Int
1		38,2						57,97	3,83	Sp
2		40,17				28,04	31,79			Ccp
3		35,89		0,12		2,89	2,98	55,62	2,5	Sp
4		22,21			77,89					Brt

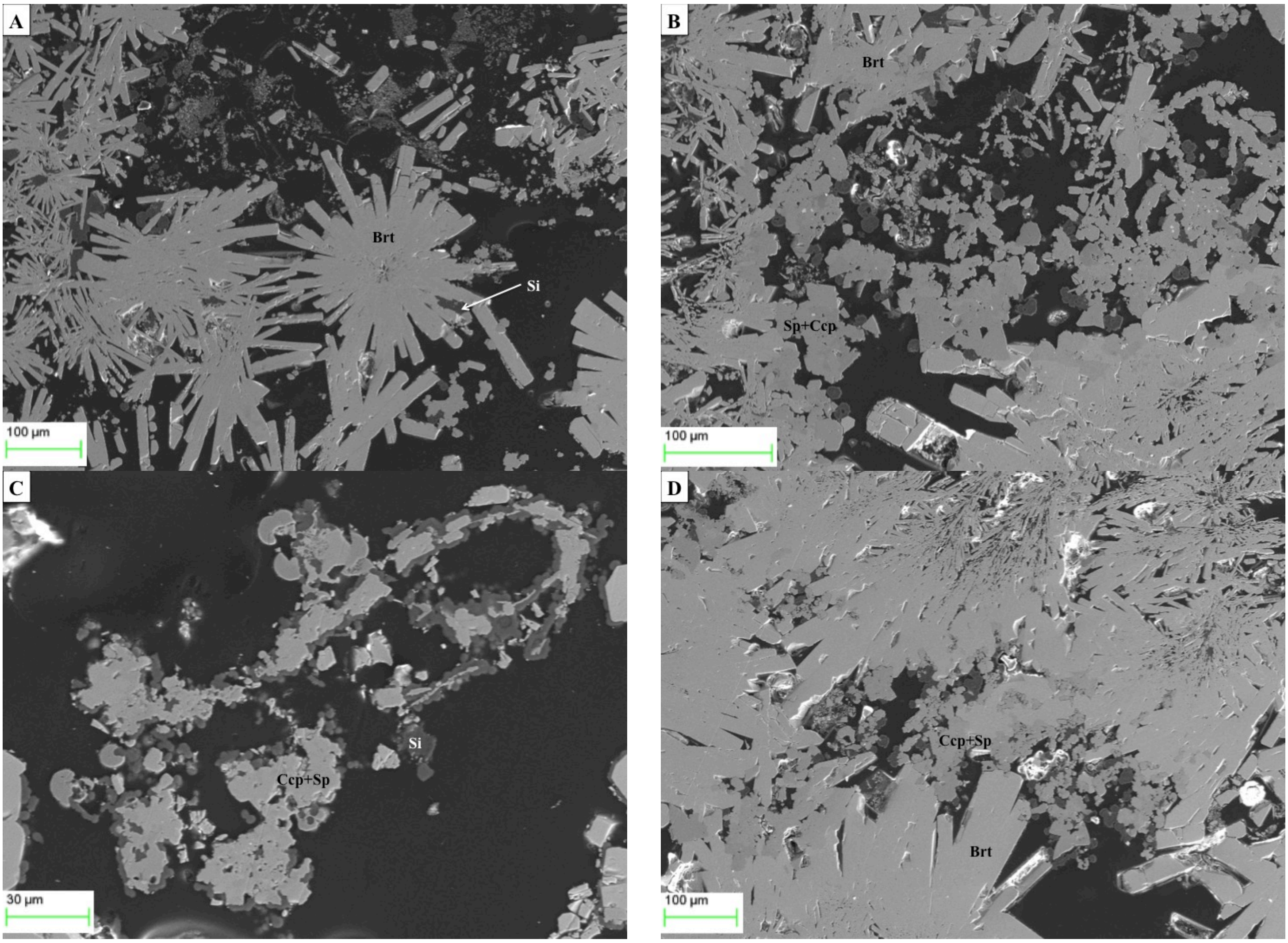

Figure 31: Picture A shows radiating clusters of acicular barite crystals with silica between the barite crystals. Picture B,C and D shows the sulphide phases sphalerite and chalcopyrite which has formed in veins and micro orifices.

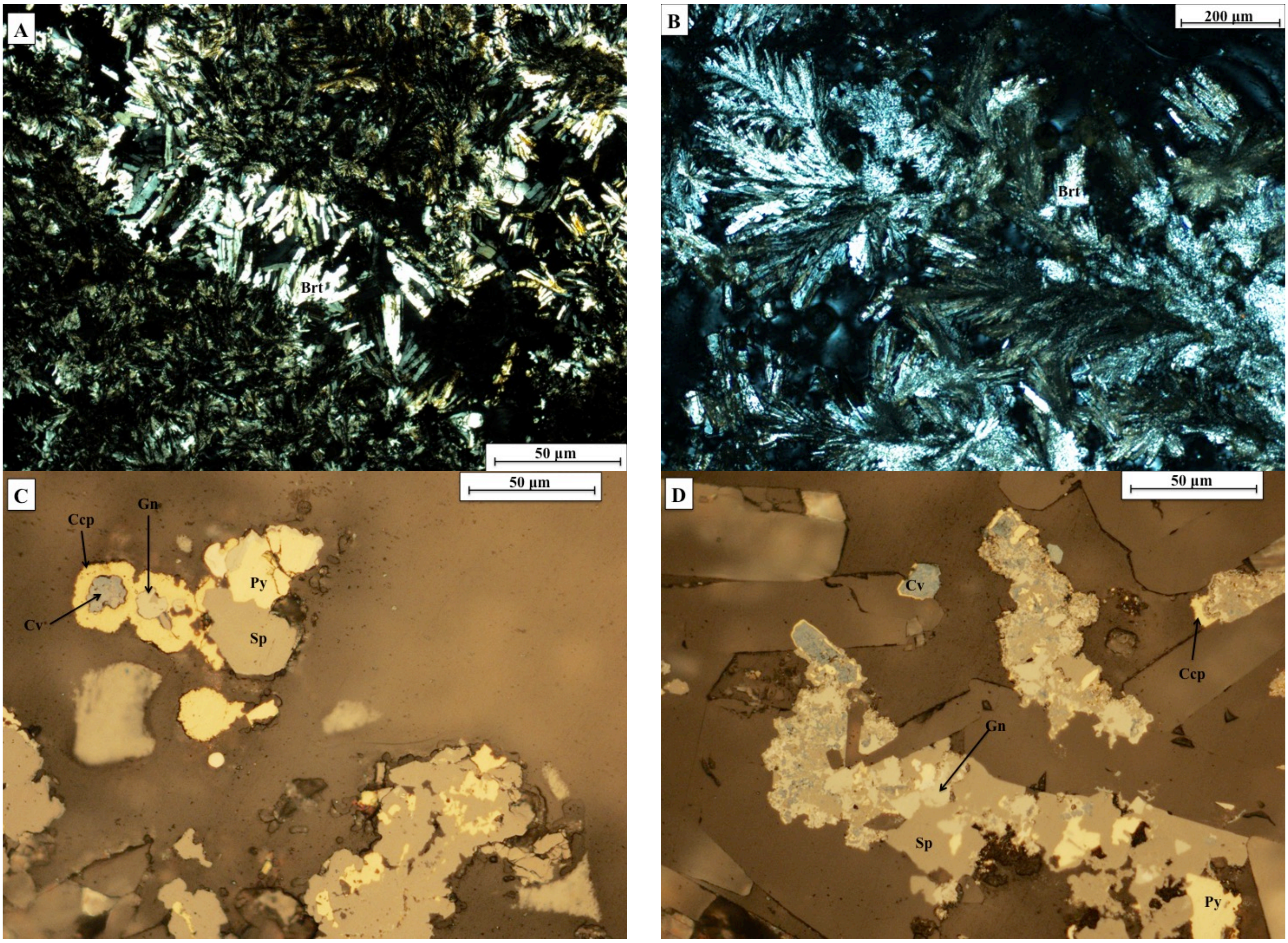

Figure 32: Picture A shows tabular and acicular barite crystals formed in a vein. B shows dendritic barite crystals. C and D show the relationship between the sulphide phases found in the thin section which is identical to GS14-ROV7B-R1A-1 and 2.

5.1.2.2 Active chimney (GS14-ROV7B-R2)

The top of a large active hydrothermal chimney was sampled showing a well-defined central orifice and concentric colour zoning from a whitish grey colour on the outer layer mostly due to the presence of anhydrite, to a darker grey interior. The chimney is composed of mainly sulphate and minor amounts of sulphides.

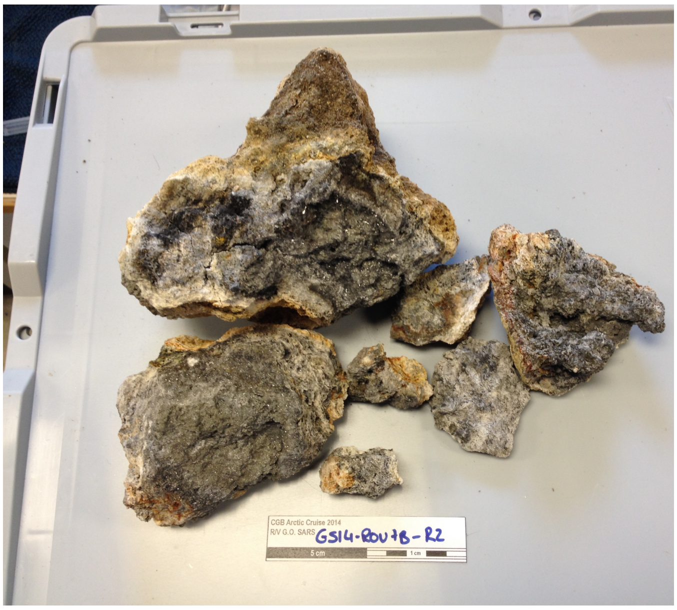

Figure 33: Picture of the active chimney sampled at the Bruse vent field.

GS14-ROV7B-R2-1: The dominant mineral phase in this sample is barite, followed by anhydrite and sulphides. The barite crystals are euhedral, and grow either as single tabular or as radiating clusters of dendritic or acicular crystals. The barite crystals are up to 350 μm long and occupy approximately 75% of surface area. It is estimated to be 20% anhydrite in the sample.Anhydrite is subhedral to anhedral and tabular. The majority of the anhydrite crystals have been partly dissolved and crystals are up to 1100 μm long. It is estimated to be 5% sulphides in the sample. The dominant sulphide phase is pyrite, followed by sphalerite, chalcopyrite and galena. The pyrite crystals are rounded and up to 240 μm wide. Pyrite and chalcopyrite formed first followed by sphalerite. Chalcopyrite is also present as inclusions within sphalerite. Galena is found associated with sphalerite often as inclusions in the sphalerite crystals.

Photo A:

shot nr:	Na	S	Ca	Sr	Ba	Int
1		23,23			76,77	Brt
2	1,04	45,74	53,22			Anh
3		46,95	53,05			Anh
4		22,6		5,06	72,34	Brt
5		45,87	54,13			Anh
6		46,21	53,79			Anh
7		42,46	49,34		8,2	Anh
8		44,68	55,32			Anh
9		46,49	53,51			Anh
10		45,61	54,39			Anh

Photo B:

shot nr:	Na	Mg	Al	Si	S	Cl	K	Ca	Ba	Fe	Cu	Zn	Ti	Int
1					45,32			54,68						Anh
2					46,36			53,64						Anh
3					36,73	11,26				26,59	25,42			Ccp
4		13,51	31,38	46,29	8,82									Si
5					45,59			54,41						Anh
6					19,77			2,02	78,21					Brt
7		14,57	28,21	38,74	5,13				13,35					Si
8		8,78	14,35	16,61	15,26				43,27				1,73	Brt
9	10,93		4,65	37,61	9,97	11,43	3,4	5,46	16,53					Brt
10					53,9					30,74		15,37		Sp
11					21,87				78,13					Brt

Photo C:

shot nr:	Na	Mg	Al	Si	S	Cl	K	Ca	Ba	Fe	Ti	Int
1	0,05				57,9					42,05		Py
2					57,83					42,17		Py
3					22,5				77,5			Brt
4		2,67	29,06	58,35		3,18	2,63	2,03		2,09		Si
5					22,17				77,83			Brt
6					45			55				Anh
7					21,89				76,54		1,58	Brt
8		2,35	12,3	16,92	18,15				50,29			Brt
9					23,63				76,37			Brt

Photo D:

shot nr:	Mg	Al	Si	S	Cl	K	Ba	Fe	Cu	Zn	Int
1				22,01			77,99				Brt
2	5,62	18,51	26,99	27,03	2,91	1,38		17,56			Py
3		1,33	1,46	51,42				32,37		13,42	Sp
4				22,29			77,71				Brt
5				58,02				41,98			Py
6				22,52			77,48				Brt
7	8,71	35,36	55,93								Si
8			1,14	39,01				28	31,85		Ccp

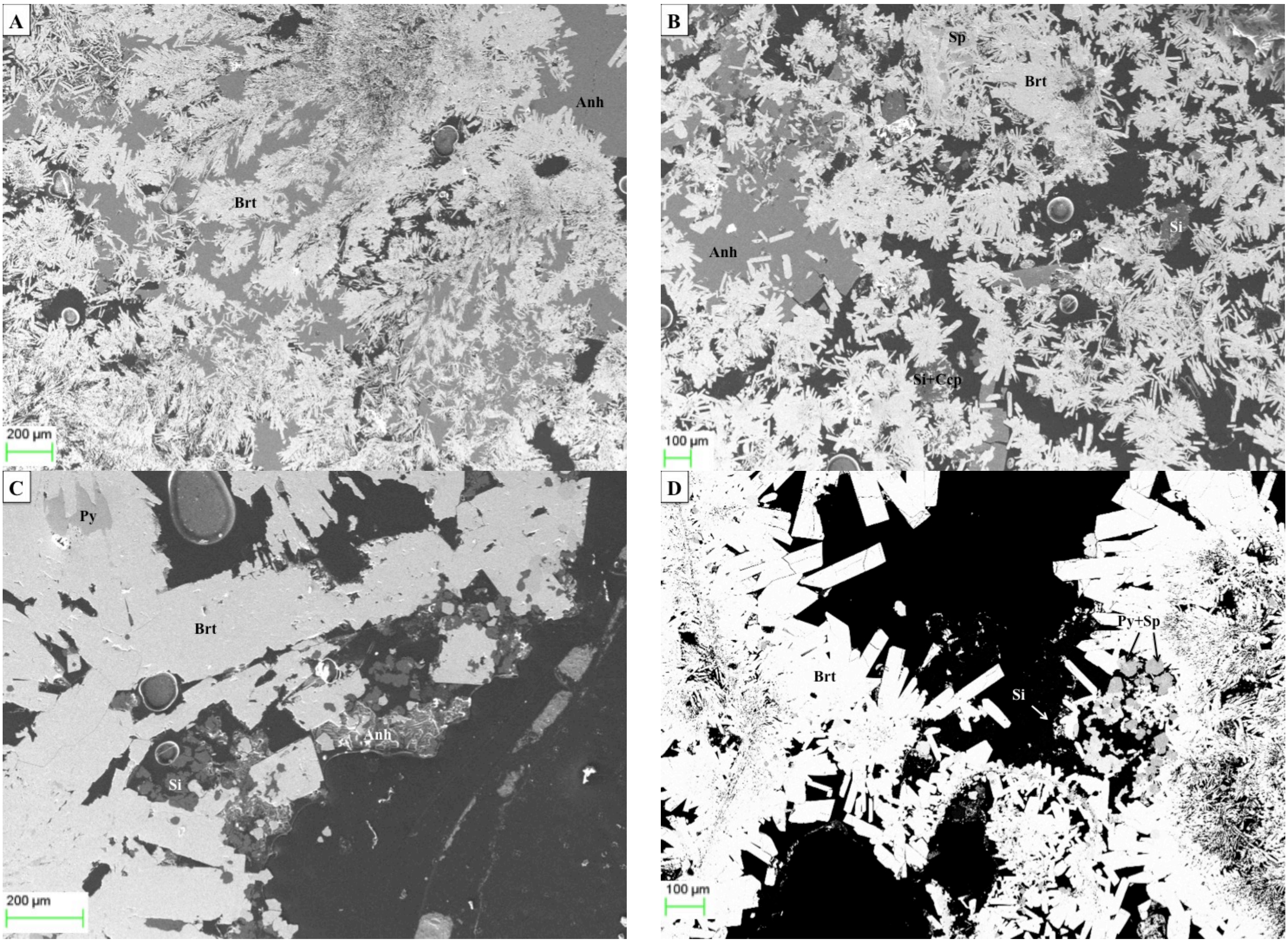

Figure 34: Picture A shows dissolved anhydrite with radiating clusters of acicular barite crystals inbetween. B shows the same relationship between barite and anhydrite, and also silica, chalcopyrite and sphalerite formed in the open pore space. C shows the same relationship between barite, anhydrite and silica and pyrite formed in the open pore space. D shows silica, pyrite and sphalerite formed in a vein found between barite crystals.

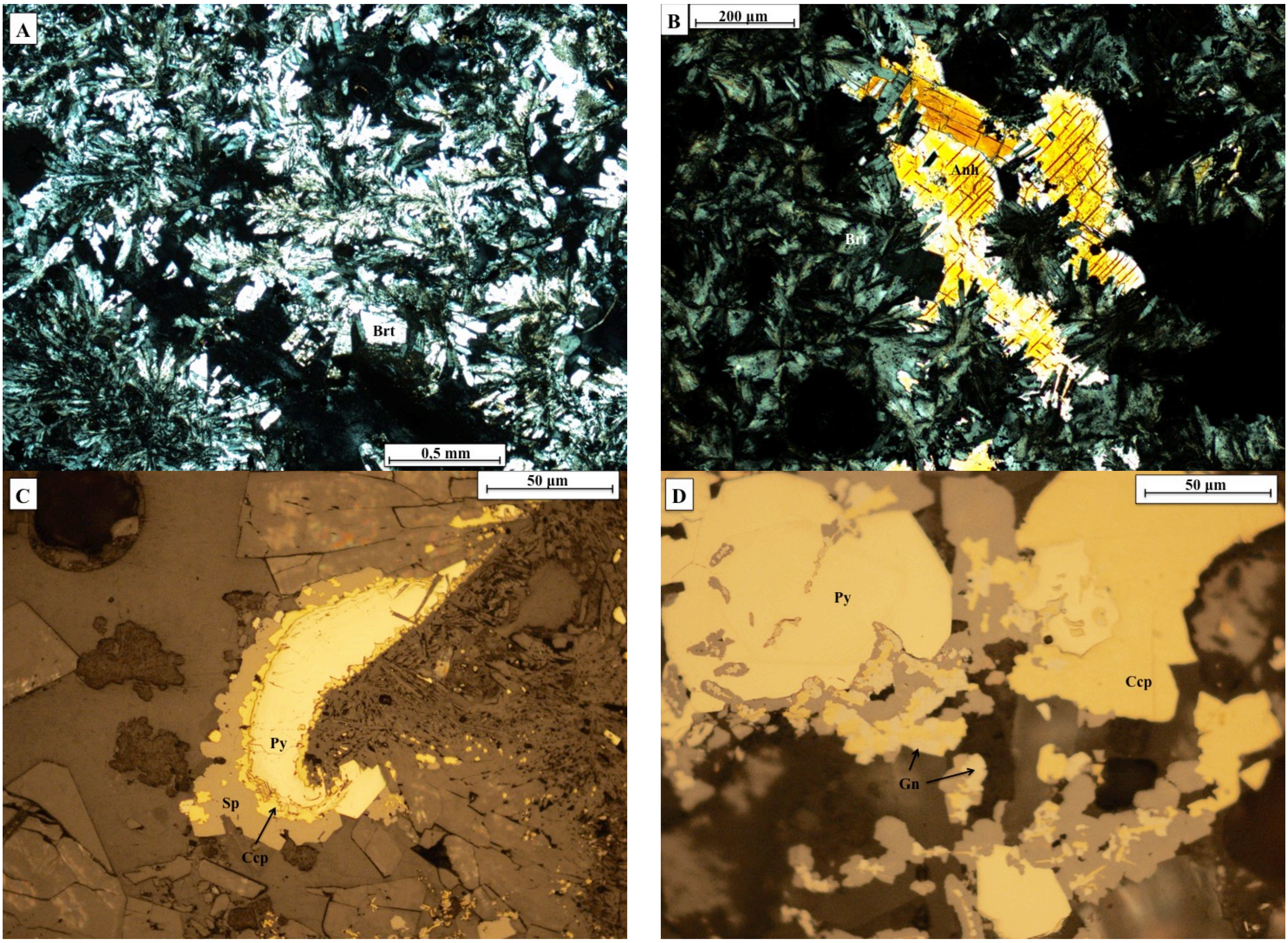

Figure 35: Picture A shows acicular and dendritic barite crystals. B shows partly dissolved anhydrite crystals with barite crystals formed around the dissolved parts of the crystal. C showcases the formation sequence of sulphides with pyrite formed initially, chalcopyrite second and sphalerite last, or parallel with chalcopyrite. D shows the same sulphide phases as in C with the addition of galena, which is found in relationship with sphalerite.

GS14-ROV7B-R2-2: The dominant phase in this sample is barite, followed by sulphides. The barite is euhedral, and is either single tabular or grows in radiating clusters of dendritic or acicular crystals. The largest barite crystals are up to 600 μm and are found in veins or micro orifices. However, the majority of the barite crystals in the sample are around 40 μm long. The sulphide phases found in this thin section are pyrite, followed by chalcopyrite and sphalerite and do not exceed 1-2% of surface area. The pyrite crystals are rounded and up to 370 μm wide. The sulfide paragenesis is the same as in GS14-ROV7B-R2-2, except for galena that is lacking in this section.

Photo A:

shot nr:	S	Fe	Cu	Mo	Zn	Int
1	53,1	41,28		5,62		Py
2	56,61	43,39				Py
3	55,48	42,76		1,76		Py
4	53,53	42,54		3,93		Py
5	54,67	40,97		4,36		Py
6	57,95	42,05				Py
7	36,66	29,3	28,22	5,82		Ccp
8		6,55	7,52	68,43	17,5	Sp
9	37,36				62,64	Sp

Photo B:

shot nr:	Al	S	Ba	Fe	Mo	Int
1		52,76		42,92	4,33	Py
2	0,15	55,22		42,51	2,12	Py
3		51,7		39,11	9,2	Py
4		57,14		42,86		Py
5		51,27		40,58	8,15	Py
6		56,52		43,48		Py
7		51,86		41,79	6,35	Py
8		52,59		40,95	6,45	Py
9		22,26	77,74			Brt
10		23,24	76,76			Brt

Photo C:

shot nr:	Al	Si	S	Cl	Ba	Fe	Mo	Int
1			58,02			41,98		Py
2			57,11			42,89		Py
3			56,67			43,33		Py
4			56,34			43,66		Py
5			57,6			42,4		Py
6			49,48			43,4	7,12	Py
7			48,67			41,52	9,81	Py
8		4,26	19,68	3,78	72,27			Brt
9			22,67		77,33			Brt

Photo D:

shot nr:	Si	S	Ba	Fe	Cu	Mo	F	Zn	Int
1		56,99		43,01					Py
2		39,12		27,6	31,91		1,38		Ccp
3	0,1	49,92		41,52		8,46			Py
4		45,11		37,13		17,76			Py
5		56,65		43,35					Py
6		52,55		41,73		5,72			Py
7		57,84		42,16					Py
8		53,66		42,06		4,28			Py
9		44,99	17,03	32,5		5,48			Py

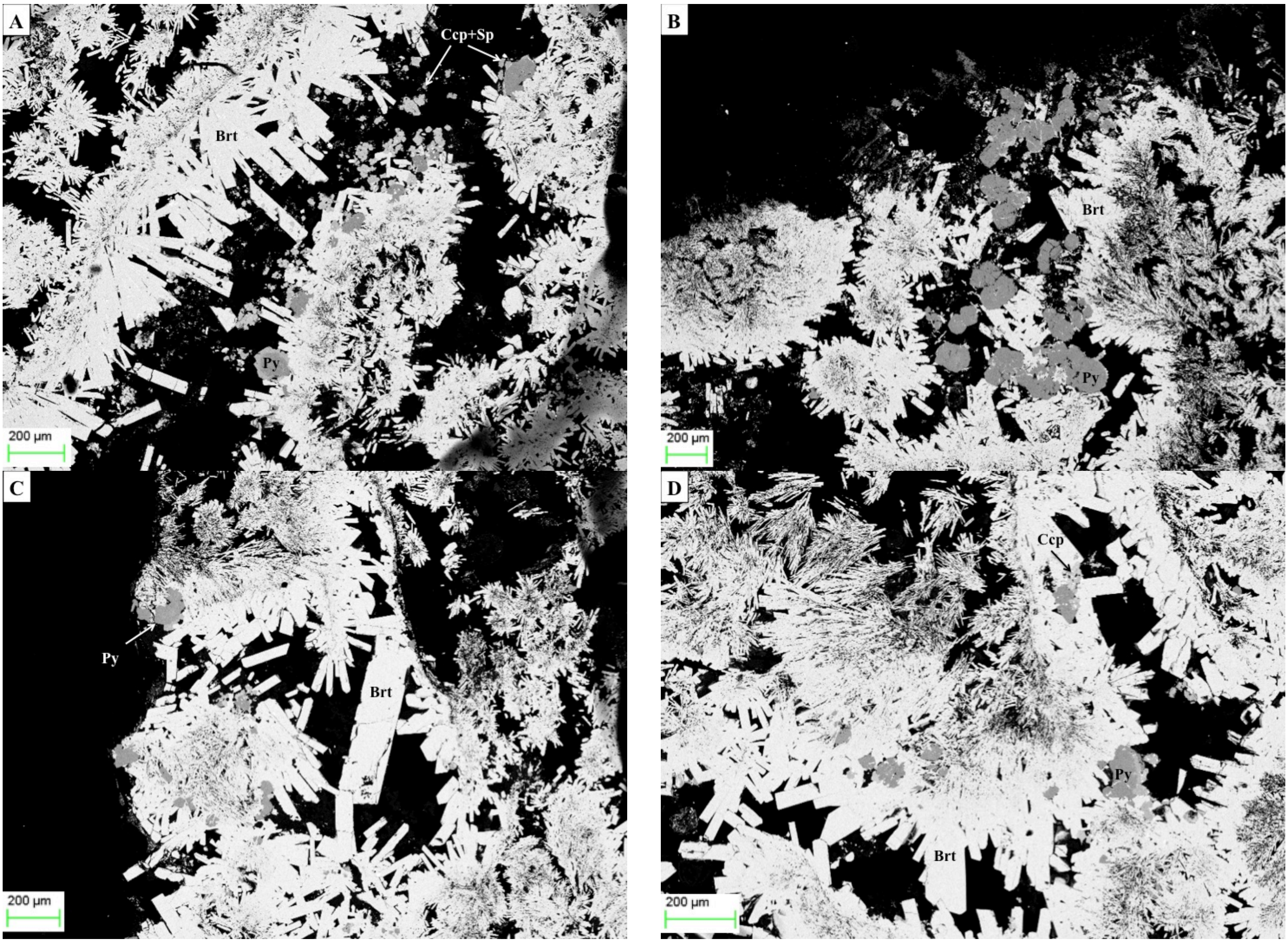

Figure 36: Pictures A,B,C and D shows the same pattern of mineralization with tabular or acicular crystals of barite with sulphides formed in the open pore spaces of veins or micro orifices.

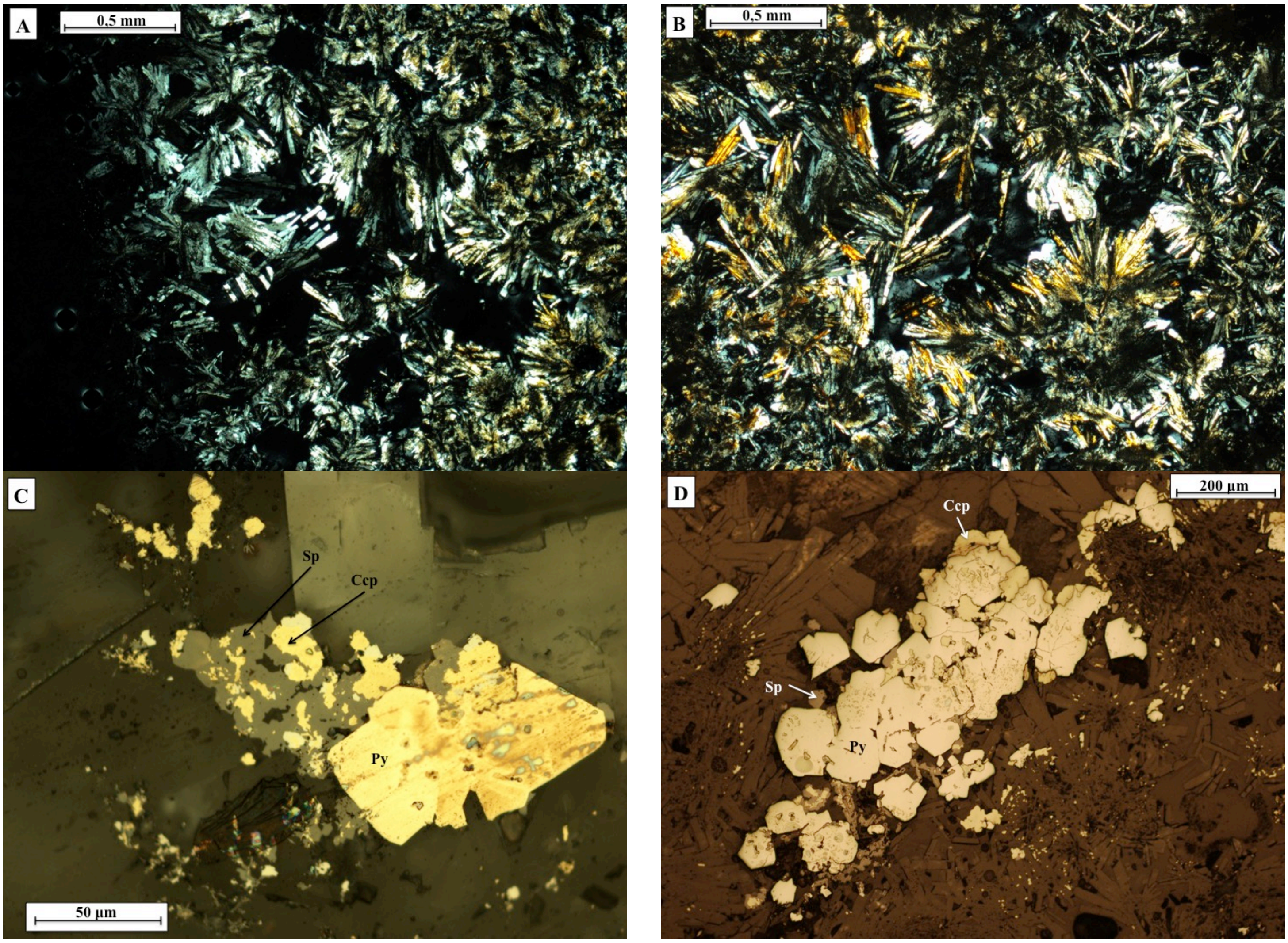

Figure 37: Picture A and B shows tabular or acicular barite crystals, with bigger crystals formed in veins. Picture C shows the sulphide assemblages found in this thin section. D shows one of the large pyrite crystals found in this thin section.

GS14-ROV7B-R2X2-1: The most dominant mineral phase in this sample is barite followed by anhydrite and sulphides. The barite is euhedral and grows as radiating clusters of dendritic or acicular crystals. The content of barite in the sample is about 70%, and the crystals range from 20 to 400 µm. The barite crystals are larger in veins and in micro orifices. The habit ranges from anhydrite if subhedral to anhedral. The anhydrite crystals are tabular, and range from 80 µm to 1.8 mm long. They are partly dissolved, and some anhydrite crystals have barite crystals growing in dissolved cavities. There are approximately 1-2% sulphides in the sample. Pyrite dominates the sulphide phase followed by sphalerite and chalcopyrite. The pyrite is dominantly rounded and is up to 400 µm wide. Pyrite and chalcopyrite formed first followed by sphalerite.

Photo A:

shot nr:	Mg	Al	Si	S	Ca	Ba	Mo	Int
1				46,04	53,96			Anh
2				45,44	54,56			Anh
3				47,4	52,6			Anh
4				46,87	53,13			Anh
5				21,46		78,54		Brt
6				22,56		77,44		Brt
7				19,69		76,62	3,69	Brt
8				22,37		77,63		Brt
9	4,82	5,51	6,49	19,25		63,93		Brt
10	6	5,12	6,61	20,99		61,27		Brt

Photo B:

shot nr:	Si	S	Cl	Ca	Ba	Fe	Cu	Mo	Zn	Int
1		23,14	3,05	7,78	66,03					Brt
2		39,53			9,58	19,84	22,36		8,68	Ccp
3		22,68			77,32					Brt
4		24,9			75,1					Brt
5		28,39				2,19		20,85	48,57	Sp
6	0,14	47,02		52,84						Anh
7		46,51		53,49						Anh
8		46,28		53,72						Anh
9		22,68			77,32					Brt

Photo C:

shot nr:	Si	S	Cl	Ca	Sr	Ba	Fe	Mo	Int
1		57,6					42,4		Py
2		57,24					42,76		Py
3		58,71					41,29		Py
4		57,42					42,58		Py
5		46,7		53,3					Anh
6		22,65			4,05	73,3			Brt
7		23,89				76,11			Brt
8		45,5		54,5					Anh
9		45,49		52,75				1,75	Anh
10	11,4	20,41	4,9			63,29			Brt

Photo D:

shot nr:	Mg	Si	S	Cl	Ca	Cr	Ti	Fe	Zn	Int
1			56,39					43,61		Py
2	1,12	1,96	55,13		1,08		1,07	39,64		Py
3			57,81					42,19		Py
4			58,22					41,78		Py
5			56,78					43,22		Py
6			51,23					25,97	22,8	Sp
7			57,82					42,18		Py
8			37,97			0,49			61,54	Sp
9			39,62						60,38	Sp

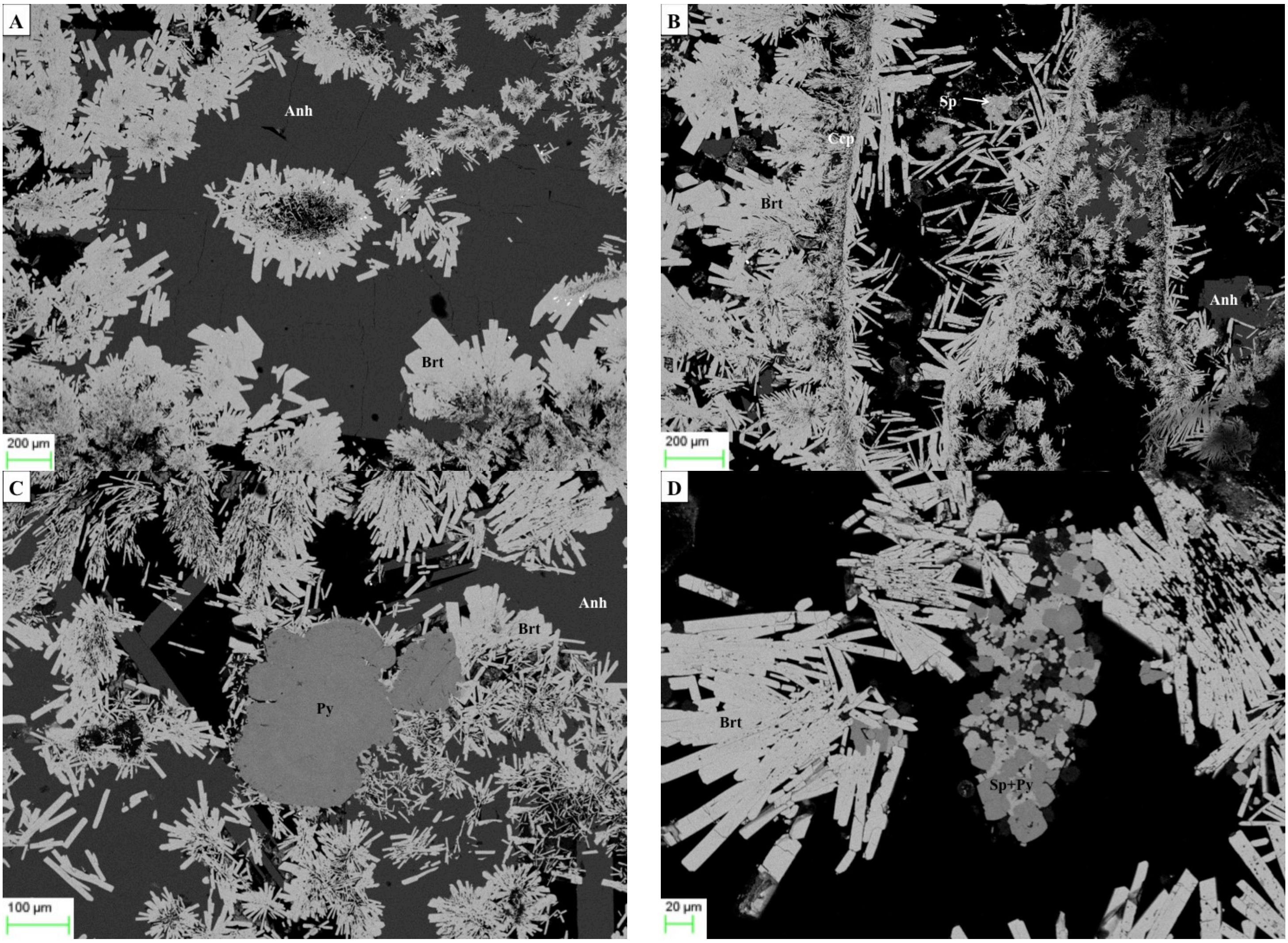

Figure 38: Picture A shows a partly dissolved anhydrite crystal with precipitated barite crystals forming in the open spaces which forms as it dissolves. B,C and D shows the relationship between the partly dissolved anhydrite crystals that gives way to barite crystals and sulphides forming in open pore spaces.

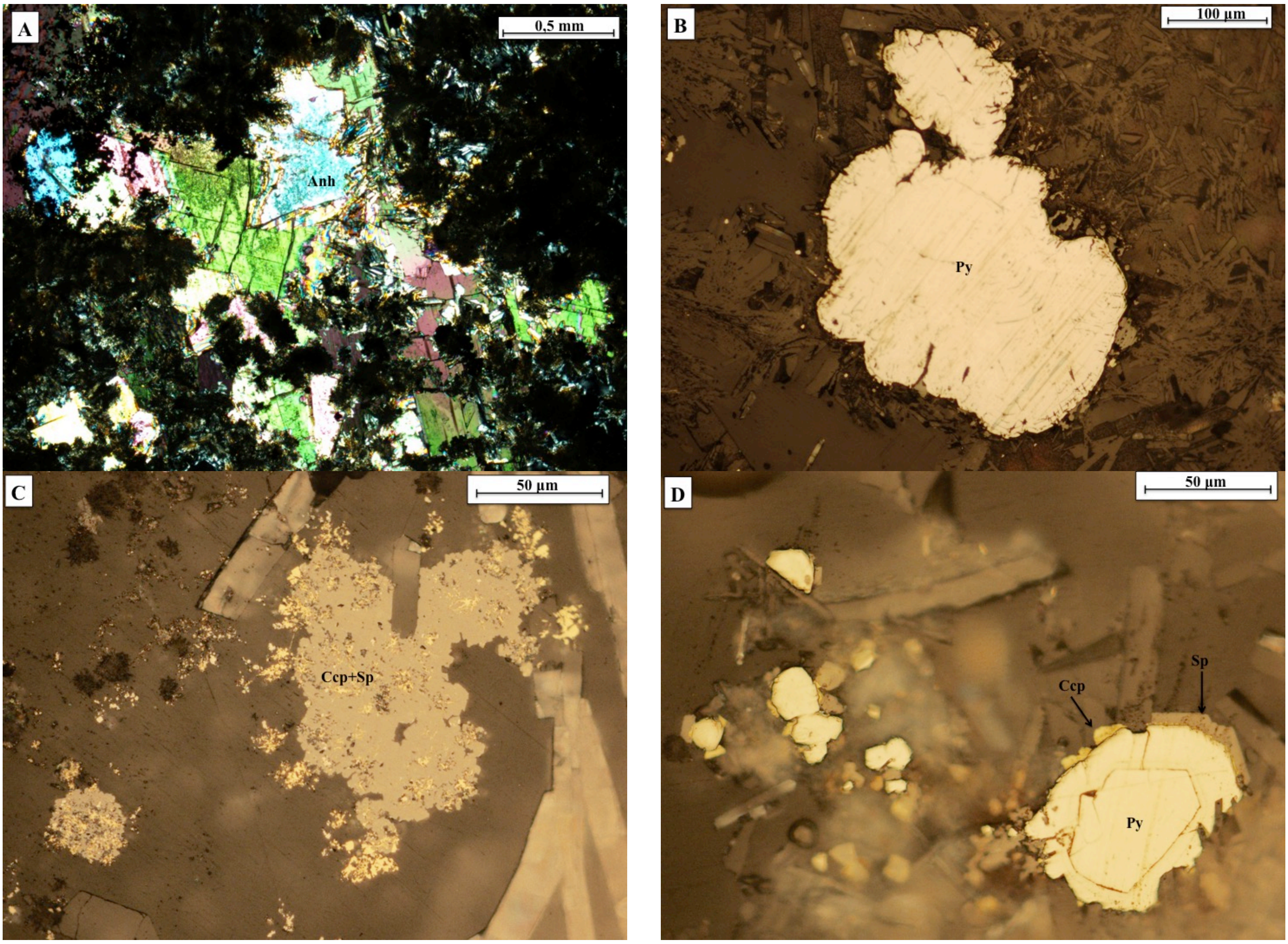

Figure 39: Picture A shows a dissolving anhydrite crystal, giving way to barite crystals. B shows a large pyrite crystal. C shows sphalerite with chalcopyrite inclusions. D shows the different sulphide phases found in this section; pyrite, chalcopyrite and sphalerite.

GS14-ROV7B-R2X2-2: The predominant mineral phase in this thin section is barite, followed by sulphide. The barite is euhedral, and grows either as single tabular crystals or in radiating dendritic or acicular clusters. The crystals range from 20 to 500 µm. The larger crystals tend to be located in veins or micro-orifices. The dominant sulphide phase is pyrite followed by sphalerite, chalcopyrite and galena. There are approximately 1% sulphides in this sample. The pyrite crystals are rounded and up to 200 µm. The relationship between the sulphide phases is similar as in GS14-ROV7B-R2X2-1. But in this thin section galena also is found. Galena is found associated with sphalerite and as inclusions inside the sphalerite crystals.

Photo A:

shot nr:	Na	Mg	Al	Si	S	Cl	K	Ca	Ba	Fe	Cu	Zn	P	Int
1	0,29		0,01		53,92		0,13			45,65				Py
2	0,33		0,01		53,06		0,18			46,39			0,03	Py
3	0,39		0,04		53,05		0,22			45,77	0,52			Py
4			0,54	0,89	16,98	3,15		0,45	78,00					Brt
5		1,55	1,25	13,97	14,06	2,12	0,17	4,29	61,33	1,25				Brt
6			1,21	1,48	21,98	0,67			1,98	6,47	6,47	59,73		Sp
7	0,42		0,04		52,69		0,34			46,46			0,04	Py
8	2,07	2,03	23,52	39,26	5,74	18,31	1,76	0,84	6,47					Si
9	0,97	1,52	39,22	56,79	0,99	0,51								Si
10			0,09		34,39					31,03	34,48			Ccp

Photo B:

shot nr:	Mg	Si	S	Ca	Sr	Ba	Fe	Int
1			21,28	0,44	1,82	74,33	2,13	Brt
2		100						Si
3		1,24	21,13	0,21		76,85	0,57	Brt
4	0,59	22,57	15,42	2,36		59,07		Brt
5		10,95	19,07			69,98		Brt
6	0,67	21,36	16,54	1,52		58,83	1,07	Brt
7	5,31	87,21	2,59			4,89		Si
8	1,75	15,56	17,44			65,25		Brt
9			19,98	1,31	2,67	76,04		Brt
10		1,13	20,78	1,19		76,9		Brt

Photo C:

shot nr:	Na	Mg	Al	Si	S	Cl	K	Ca	Sr	Ba	Fe	Cu	Zn	P	Sb	Be	Int
1					49,65						42,32	0,57		0,032		7,424	Py
2	0,76				53,40						44,60	1,24					Py
3	0,33				52,91						46,76						Py
4	0,19				53,50		0,13				46,19						Py
5					50,89						44,46	0,63				4,019	Py
6					35,52				1,58	43,87	19,03						Py
7		1,64	36,96	60,20		0,46					0,73						Si
8		2,94	36,81	58,61	0,82	0,52		0,30									Si
9		0,41	14,81	21,12	17,70	2,49					0,90	0,91	41,66				Sp
10					33,80						0,68		64,65		0,873		Sp
11	0,18				49,31						42,69					7,821	Py

Photo D:

shot nr:	Na	Mg	Si	S	Ca	Sr	Ba	Int
1				19,76		5,05	75,2	Brt
2				19,78	0,48	4,75	74,99	Brt
3			100					Si
4		0,34	99,66					Si
5				20,62		2,29	77,09	Brt
6	0,32		99,68					Si
7			1,61	22,55	0,52		75,33	Brt

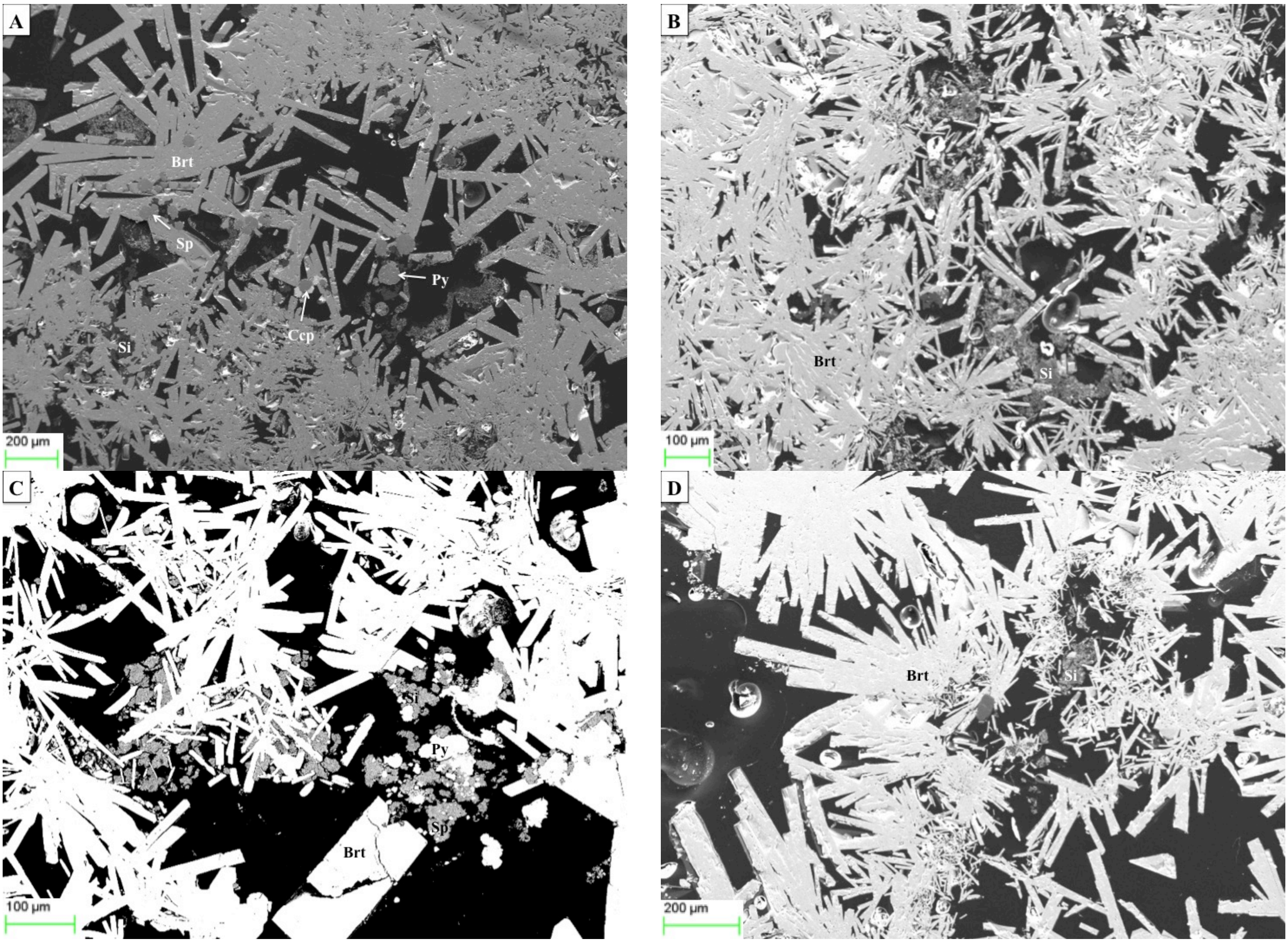

Figure 40: Picture A, B, C and D shows tabular or acicular barite crystals with the sulphide phases found in the open pore space inbetween crystals.

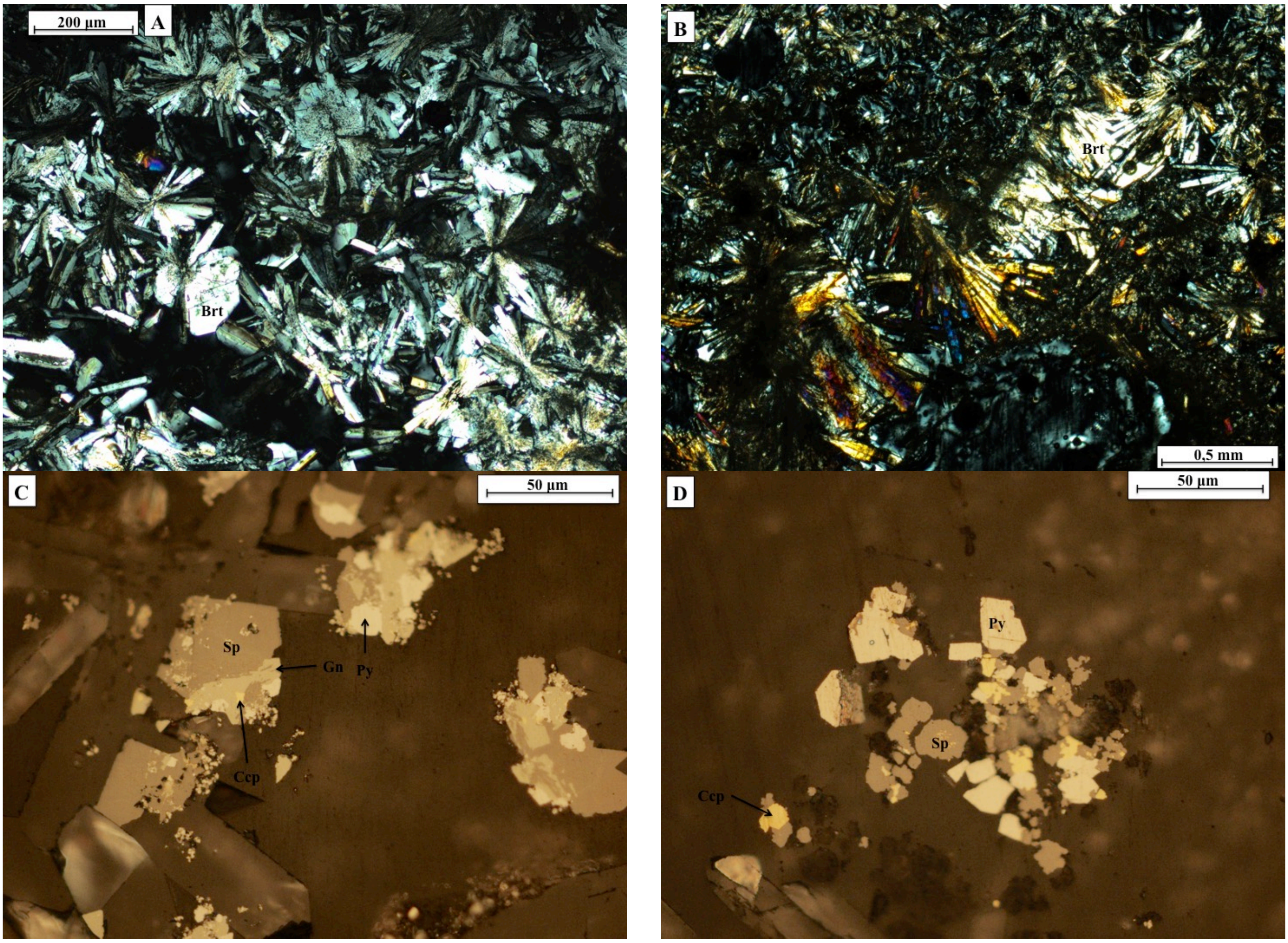

Figure 41: Picture A shows radiation clusters of acicular barite crystals. B shows large barite crystals that have formed in a vein. C and D show the relationship between the sulphides found in this thin section with the initial precipitation of pyrite, following chalcopyrite and sphalerite formation. Galena is also found in this thin section and is found in relationship with sphalerite.

5.1.3 Aegir vent field

A total of 4 hydrothermal chimneys from the Aegir vent field have been sampled and studied, namely GS15-AGR10-R2, GS16B-ROV7-R01, GS16B-ROV7-R02, and GS16B-ROV9-R01. A total of 7 representative thin polished sections were made from these samples. Two thin sections were made for GS15-AGR10-R2, GS16B-ROV7-R02, GS16B-ROV9-R01 and one for GS16B-ROV7-R01. Whole-rock powders were made for all samples for further geochemical studies.

5.1.3.1 Fallen inactive chimney (GS15-AGR10-R2)

This sample represents a fallen down inactive chimney collected next to an actively venting chimney. The material is very brittle and porous and consists of anhydrite and minor amounts of sulphides. In hand-specimen the sample is greyish, ranging from light grey on the outer parts of the chimney and dark grey in the interior part.

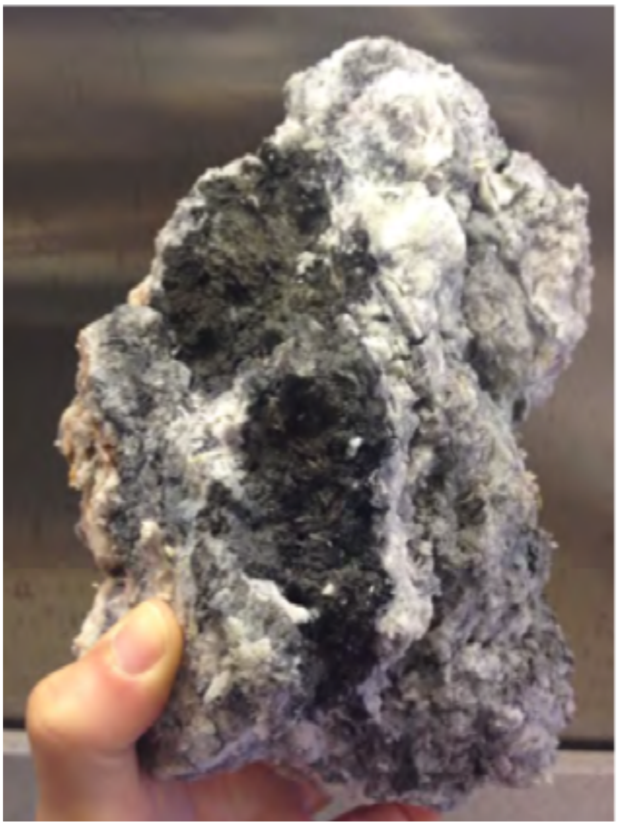

Figure 42: Shows the sampled fallen inactive chimney material from Aegir. The sample is composed of an lightly coloured outer part, and an darker inner part.

GS15-AGR1O-R2-1: Anhydrite is the dominant mineral phase in the sample, followed by globular colloform silica mixed with minor amounts of sulphides. The anhydrite crystals are euhedral to subhedral, with tabular or acicular habit. They are up to 1 mm long. Microcrystalline silica occupies approximately 15-20% of surface area and is found in high abundance in veins and micro-orifices throughout the sample. It displays layered, colloform growth with layers up to 0.5 mm thick. This chimney has an estimate of 1-2% sulphides that occur as irregular anhedral masses. Sphalerite is the most abundant sulphide phase, followed by pyrite, chalcopyrite and galena. Sphalerite is up to 150 μm long. Chalcopyrite and pyrite are found spatially associated with sphalerite, forming first being later rimmed by sphalerite. Chalcopyrite is also present as inclusions within sphalerite. Chalcopyrite and pyrite phases display textural features that suggest being formed contemporaneously because crystals of chalcopyrite can be found inside pyrite and vice a versa. Galena is found in relation with sphalerite as it only can be found inside sphalerite crystals.

Photo A:

Shot nr:	Na	Mg	Si	S	Ca	Sr	Fe	Zn	Mn	Int:
1		33,08	64,76				2,16			Si
2		33,29	64,86				1,84			Si
3				43,37	55,46	1,17				Anh
4				43,91	56,09					Anh
5		32,14	64,04		0,59		3,22			Si
6		32,23	65,04		0,45		2,29			Si
7				32,81			5,43	61,17	0,6	Sph
8				33,14			4,84	62,02		Sph
9		32,86	64,8		0,38		1,95			Si
10	0,61	32,83	64		0,45		2,11			Si

Photo B:

Shot nr:	Na	Mg	Si	S	Ca	Fe	Cu	Zn	Mn	Se	Pb	Int:
1			0,45	43,63	55,92							Anh
2			0,26	41,5	57,04	1,2						Anh
3			0,69	42,1	57,22							Anh
4				34,43		3,13		61,94	0,5			Sph
5	0,22				0,8	1				0,97	97,01	Gn
6		33,2	63,68		0,47	2,65						Si
7		32,76	63,99		0,44	2,14			0,67			Si
8				43,96	56,04							Anh
9			0,38	31,86	0,15	4,32		63,29				Sph
10				34,45		31,09	34,46					Ccp

Photo C:

Shot nr:	Na	Mg	Si	S	Ca	Sr	Fe	Zn	Mn	Int:
1		32,04	65,41		0,38		2,17			Si
2	0,54	31,92	61,78		1,81		3,95			Si
3			0,42	43,62	55,96					Anh
4			0,28	32,22	0,15		7,19	59,77	0,38	Sph
5				32,95			6,67	59,83	0,55	Sph
6				34,19			4,26	61,55		Sph
7				43,64	54,86	1,5				Anh
8				32,68	0,11		5,89	60,8	0,52	Sph
9				43,48	56,52					Anh
10		32,08	63,2		1,23		3,48			Si
11				32,31			4,84	62,44	0,41	Sph
12				43,42	56,58					Anh

Photo D:

Shot nr:	Na	Mg	Si	S	Ca	Sr	Fe	Cu	Mo	Zn	Mn	Int:
1				43,58	56,42							Anh
2				43,02	54,93	2,05						Anh
3		5,33	6,41	28,01			3,05			56,74	0,46	Sph
4			0,18	33,92			24,11	25,14		16,64		Sph
5				32,21			4,99			62,19	0,6	Sph
6		33,21	64,39		0,41		1,98					Si
7	0,6	32,52	62,88		0,27		2,76		0,96			Si
8				43,46	56,54							Anh
9				43,3	55,83	0,86						Anh
10		1,32	1,98	42,39	54,31							Anh

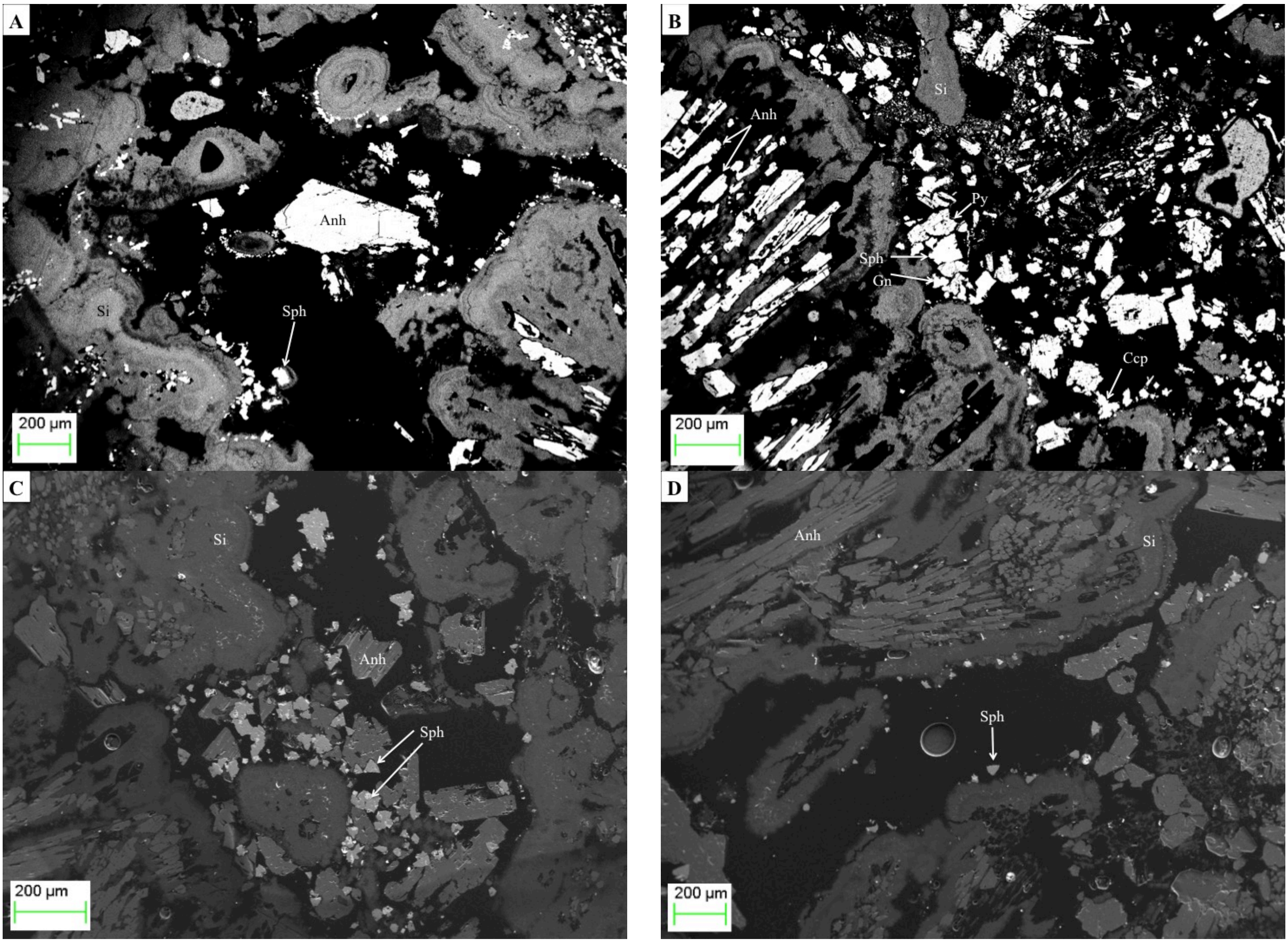

Figure 43: Picture A,B,C and D chows initially formed anhydrite crystals covered by colloform silica, and sulphide crystals formed either inside the silica or in the pore space.

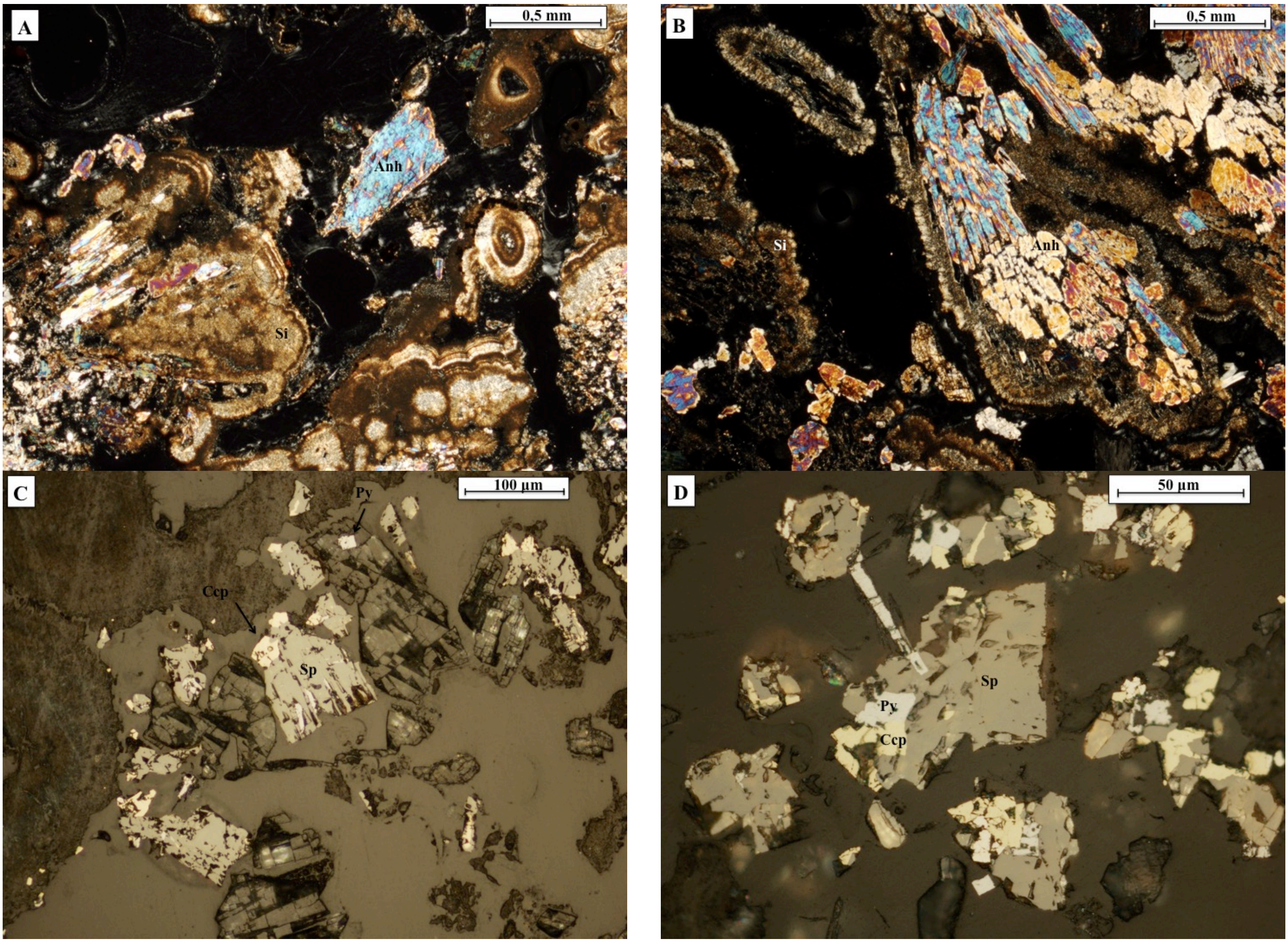

Figure 44: Picture A and B shows anhydrite crystals covered in colloform silica. C and D shows the sulphide phases found in the thin section, with the exception of galena that is found in smaller amounts.

GS15-AGR1O-R2-2: The dominant mineral phase in this thin section is anhydrite followed by silica combined with minor amounts of sulphide. Anhydrite crystals are acicular, euhedral to subhedral, and show large variation in size and shape, the longest crystals can be up to 2000 μm long. The silica is found in veins and micro-orifices. The layer of silica can be up to 150 μm thick, and show colloform growth banding. The sample has an estimate of 10-15% silica. There are minor amounts of sulphides in the sample, occupying less than 1% of surface area. Sulfide paragenesis is identical to GS15-AGRIO-R2-1, but there is not found galena.

Photo A:

shot nr:	Mg	Al	Si	S	Cl	Ca	Fe	Cu	Zn	Mn	Int
1				34,16		0,16	7,61		57,61	0,46	Sp
2				32,76		0,1	6,96		59,78	0,4	Sp
3	2,09	6,06	2,72	39,1	1,3	48,73					Anh
4		1,79	0,39	39,8	3,08	54,94					Anh
5				35,67			5,58		58,21	0,54	Sp
6				34,61			8,39		56,51	0,49	Sp
7	0,18		0,38	43,38		56,07					Anh
8				33,45		0,13	7,64		58,3	0,48	Sp
9	0,23	0,71	0,66	34,06		0,13	30,74	33,47			Ccp
10	25,42	2,3	51,18	8,33	10,74	0,38	1,66				Si
11		1,96	0,53	35,23	0,15	0,31	5,33		56,14	0,35	Sp
12	20,03	0,85	36,48	18,98	5,22	17,42	1,02				Si

Photo B:

shot nr:	Na	Mg	Al	Si	S	Cl	K	Ca	Fe	Mo	Zn	Mn	Int
1		27,27	1,47	39,87	1,17	0,19	0,11	0,23	26,09		3,6		Si
2		28,03	1,1	58,82	0,79	9,39			1,88				Si
3		30,77	3,61	47,73				0,26	14,65	1,21	1,27	0,5	Si
4		33,49	4,24	53,1					6,39	0,75	1,52	0,51	Si
5	0,71	31,02	1,29	62,72			0,22	0,54	2,14	1,37			Si
6	0,81	30,13	1,08	63,21	0,73		0,2	0,61	3,24				Si
7	0,74	29,87	1,2	64,76	0,51		0,28	0,55	2,09				Si
8	0,69	10,37	40,53	36,31	1,36	5,64	0,54	2,6	1,96				Si

Photo C:

shot nr:	Na	Mg	Al	Si	S	Cl	K	Ca	Fe	Mn	Int
1					42,79			57,21			Anh
2			0,07		43,47			56,46			Anh
3		32,15	0,74	60,89	0,77	3,6		1,1	0,75		Si
4		34,58	0,98	61,65		1,07		0,5	0,82	0,4	Si
5		35,01	0,84	59,98		2,98		0,41	0,78		Si
6	1,07	31,3	0,67	58,82	1,7	4,14	0,21	1,07	1,03		Si
7		38,55	1,03	54,79		5,36		0,27			Si

Photo D:

shot nr:	Na	Mg	Al	Si	S	Cl	K	Ca	Fe	Cu	Mo	Zn	Int
1		29,54	2,82	48,34	6,85	0,81	0,82	2,45	4,79			3,58	Si
2		26,96	2,19	33,5	17,16	0,49	0,31	0,21	6,05			13,13	Si
3			0,08		38,58			0,16	18,28	16,6		26,29	Ccp
4	1,06	32,4	3,27	57,95		0,66	0,33	0,33	2,33		1,66		Si
5	1,19	32,22	3,68	57,25	1,34	1,36	0,15	0,27	2,54				Si
6		0,85		0,69	37,18			0,16	29,69	31,42			Ccp
7		23,71	1,67	25,77	20,68	3,06	0,25		4,14			20,72	Sp
8	0,92	32,35	3,45	54,04	1,32	4,66	0,41	0,52	2,33				Si
9	0,74	31,17	2,88	55		1,6	0,53	0,49	1,92		5,68		Si
10	0,9	32,81	3,04	58,67	0,76	0,56	0,62	0,59	2,06				Si
11					43,47			56,21					Anh

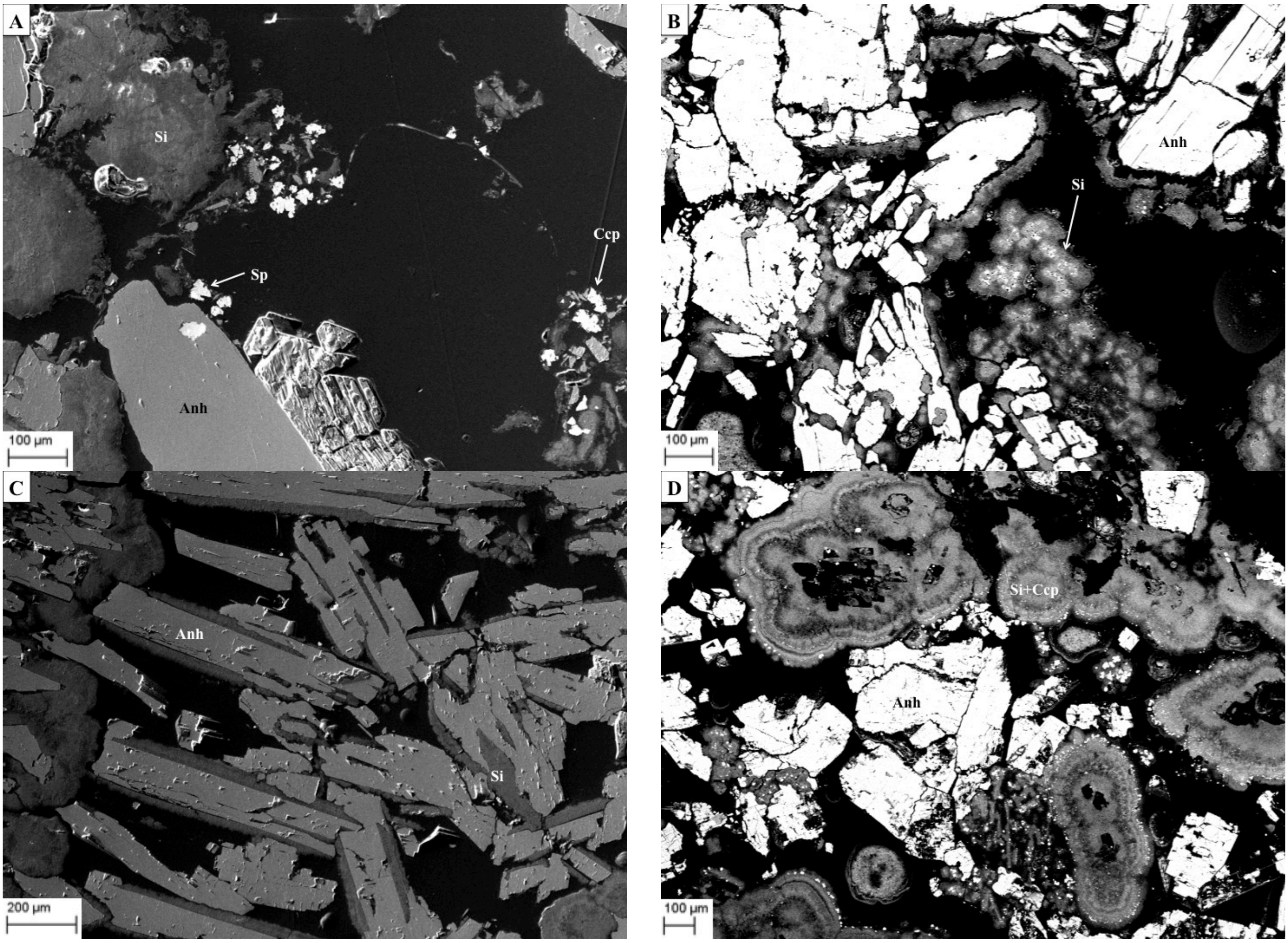

Figure 45: These pictures shows the same mineral assemblages and relationships as are found in figure 43 and 44, with the exception of galena which are not found in this thin section.

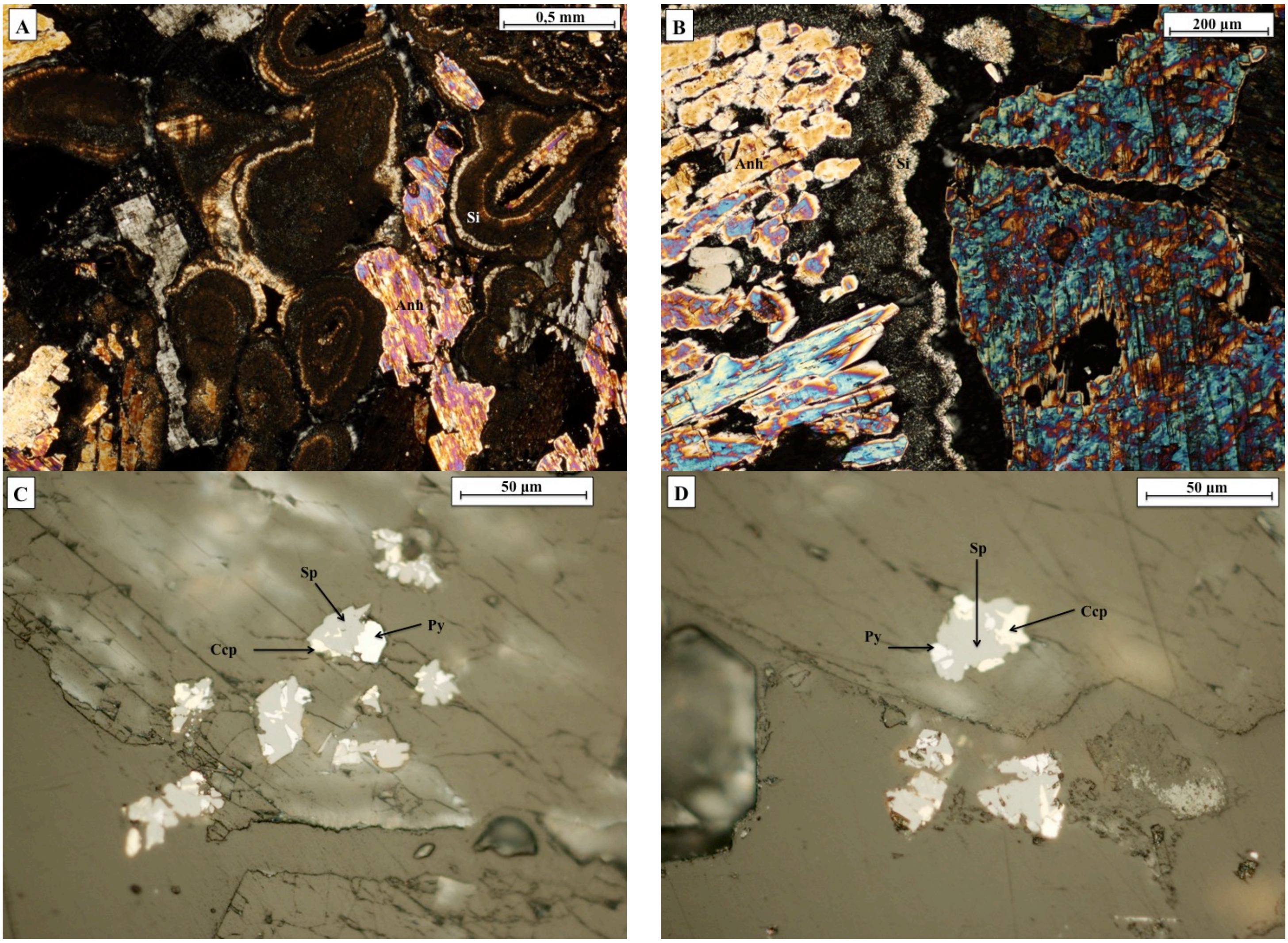

Figure 46: These pictures shows the same mineral assemblages and relationships as are found in figure 43 and 44, with the exception of galena which are not found in this thin section.

5.1.3.2 Fallen inactive chimney (GS16B-ROV7-R01)

Fallen down, inactive chimney material, sampled next to an active chimney. The material is brittle and porous and consists of anhydrite with minor amounts of sulphides. The material has some areas with high concentrations of anhydrite that are either white or pinkish. The remaining portions of the material are greyish to black.

Figure 47: Picture of the fallen inactive chimney material. The material is zoned and has areas abundant in anhydrite.

GS16B-ROV7-R01: The main mineral phase found in this thin section is anhydrite, followed by barite, amorphous silica, and sulphides. The anhydrite crystals are euhedral to subhedral with shapes that can be tabular or acicular reaching up to 800 μm long. Barite crystals are euhedral and grow as acicular radiating clusters of up to around 1 mm. The amorphous silica is colloform and is found in patches that are up to 1 mm thick or in veins or orifices where it has precipitated around anhydrite crystals. The thin section has a small amount of sulphides, estimated to be less than 1% distributed as clusters of sulphides around 30 μm in size. The main mineral phase is pyrite followed by sphalerite, chalcopyrite and galena. Pyrite and chalcopyrite formed first followed by formation of sphalerite, and these phases can be found inside the sphalerite crystals. Galena is only found associated to sphalerite.

Photo A:

shot nr:	Na	Mg	Al	Si	S	Cl	K	Ca	Fe	Cu	Zn	Se	Pb	Int
1		31,01	2,25	59,98	1,33	1,39		1,5	2,54					Si
2			0,2			5,17					1,23	0,63	92,77	Gn
3		18,24	1,15	29,03	27,17	3	0,41	0,82	3,59		16,59			Sp
4		29,61	1,98	53,61	6,84	0,64		0,78	1,94		4,61			Si
5		0,68		0,24	51,97				46,37	0,75				Py
6		8,96	0,22	16,44	28,45	1,06		0,46	21,99	19,77	2,65			Ccp
7		4,78	0,09	4,85	50,37	0,78			37,89	1,24				Py
8		16,38	1	26,44	23,76	0,84	0,28	0,62	16,01	14,67				Ccp

Photo B:

shot nr:	Na	Mg	Al	Si	S	Cl	K	Ca	Fe	Cu	Zn	Mn	Se	Pb	Int
1		5,26	0,12	5,06	49,03				35,7	1,22	3,61				Py
2		21,58	0,99	31,98	21,72	1,48	0,42	0,72	2,15		18,96				Sp
3					62,48	0			3,36		32,73		1,43		Sp
4		0		0,36	34,06				3,95		61,63				Sp
5		13,24		19,4	24,69	17,16	1,29		3,04		21,17				Sp
6					34,34				4,48		60,73	0,45			Sp
7		0,21		0,95	35,56				4,51		58,77				Sp
8		0,18		0,45	43,42			55,94							Anh
9		1,97	0,04	5,62	38,73	0,79		52,85							Anh
10	0,28				0	2,95		0,51						96,26	Gn
11			0,04	0,25	36,11			0,12	4,44		59,04				Sp
12		0,43		0,82	43,74			55,01							Anh

Photo C:

shot nr:	Na	Mg	Al	Si	S	Cl	Fe	Cu	Zn	V	Mn	Int
1					33,96		4,99		60,96	0,09		Sp
2					33,58		4,03		62,02		0,38	Sp
3					32,97		3,83		62,65		0,55	Sp
4					33,86		4,17		61,97			Sp
5			0,03	0,3	37,67		21,24	14,19	26,57			Sp
6					34,26		4,81		60,57		0,36	Sp
7			0,01	0,43	34,62		27,56	31,28	6,1			Ccp
8				0,26	34,82		6,32		58,06		0,54	Sp
9				0,12	35,43		5,3		58,64		0,51	Sp
10		11,43	0,52	17,46	40,13	3,93	3,76		22,76			Sp
11			0,08	0,71	36,43		3,85		58,57		0,35	Sp
12				0,44	37,42	0,46	3,35		57,82		0,51	Sp

Photo D:

shot nr:	Na	Mg	Al	Si	S	Cl	K	Ca	Fe	Cu	Zn	Mn	Pb	Int
1		2,76	0,14	3,34	34,87				28,69	30,21				Ccp
2		3,96	0,19	4,89	6,53	3,66		0,17	0,95				79,65	Gn
3		6,35	0,12	7,76	28,53			0,24	2,56		54,08	0,37		Sp
4	1,51	2,24	0,37	6,09	45,05	5,58		0,75	38,41					Py
5		31,57	2,85	59,01	0,88	1,11	0,23	0,93	2,89	0,52				Si
6		29,91	3,05	58,64	2,4	0,31		1,83	3,86					Si
7		20,92	1,52	28,97	19,24	0,44		0,61	14,48	13,82				Ccp
8		29,74	2,81	50,58	5,72	0,24		1,26	4,61		5,04			Si

Photo E:

shot nr:	Na	Mg	Al	Si	S	Cl	K	Ca	Fe	Cu	Zn	Int
1		0,99		1,47	47,86			0,67	44,17	2,17	2,68	Py
2		10,7		23,89	17,05	37,13			11,23			Py
3		5,77	0,13	7,2	45,01	0,81			39,42	1,66		Py
4	1,35	0,92		1,48	52,46	2,05	0,32	0,31	41,11			Py

Photo F:

shot nr:	Na	Mg	Al	Si	S	Cl	K	Ca	Fe	Cu	Zn	Int
1		0,99		1,47	47,86			0,67	44,17	2,17	2,68	Py
2		10,7		23,89	17,05	37,13			11,23			Py
3		5,77	0,13	7,2	45,01	0,81			39,42	1,66		Py
4	1,35	0,92		1,48	52,46	2,05	0,32	0,31	41,11			Py

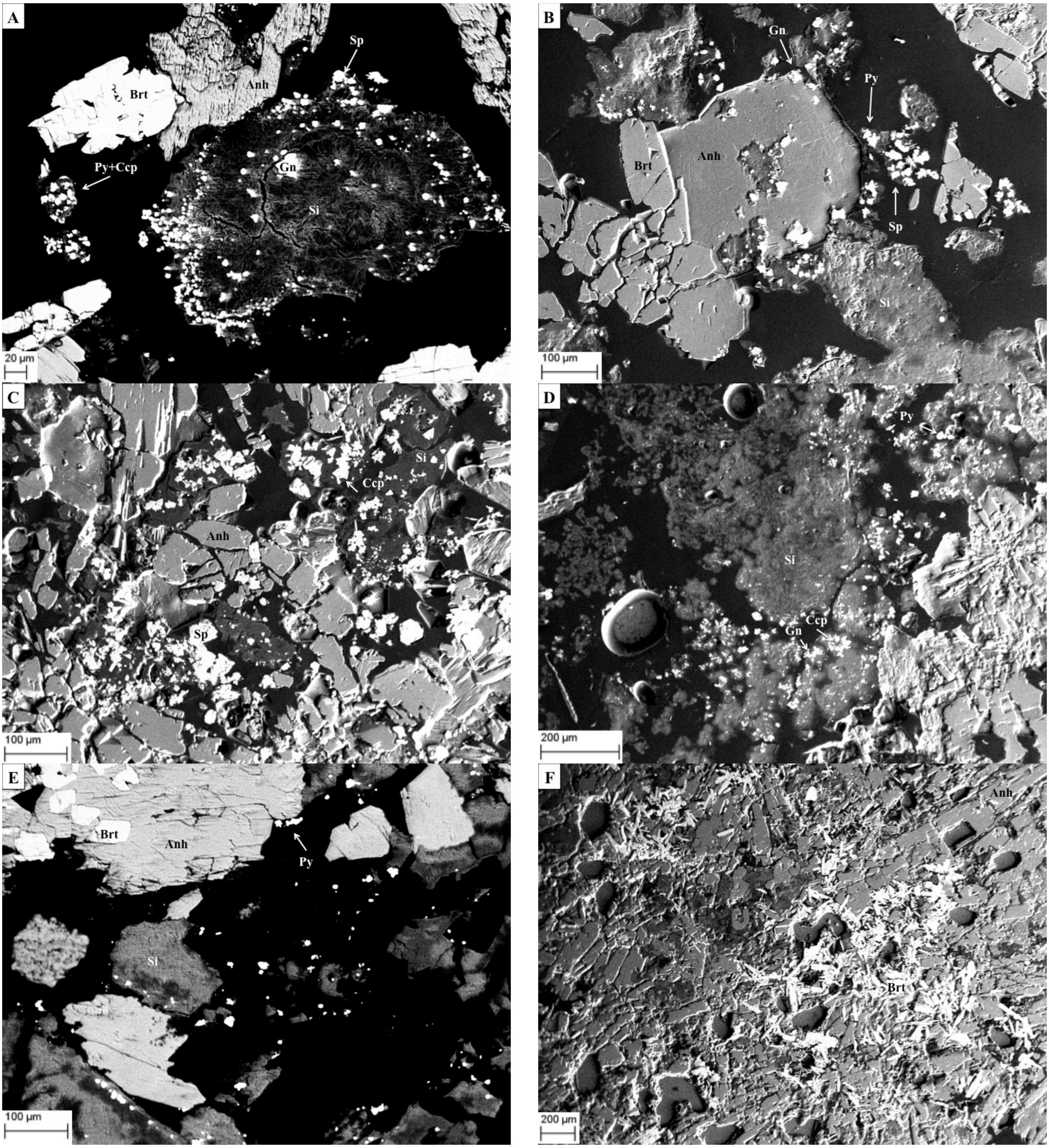

Figure 48: Picture A,B,C,D and E shows initial anhydrite crystals that are partly dissolved and replaced by barite. In the pore spaces abundant colloform silica have formed and are found in association with sulphides. E shows radiating clusters of acicular barite crystals.

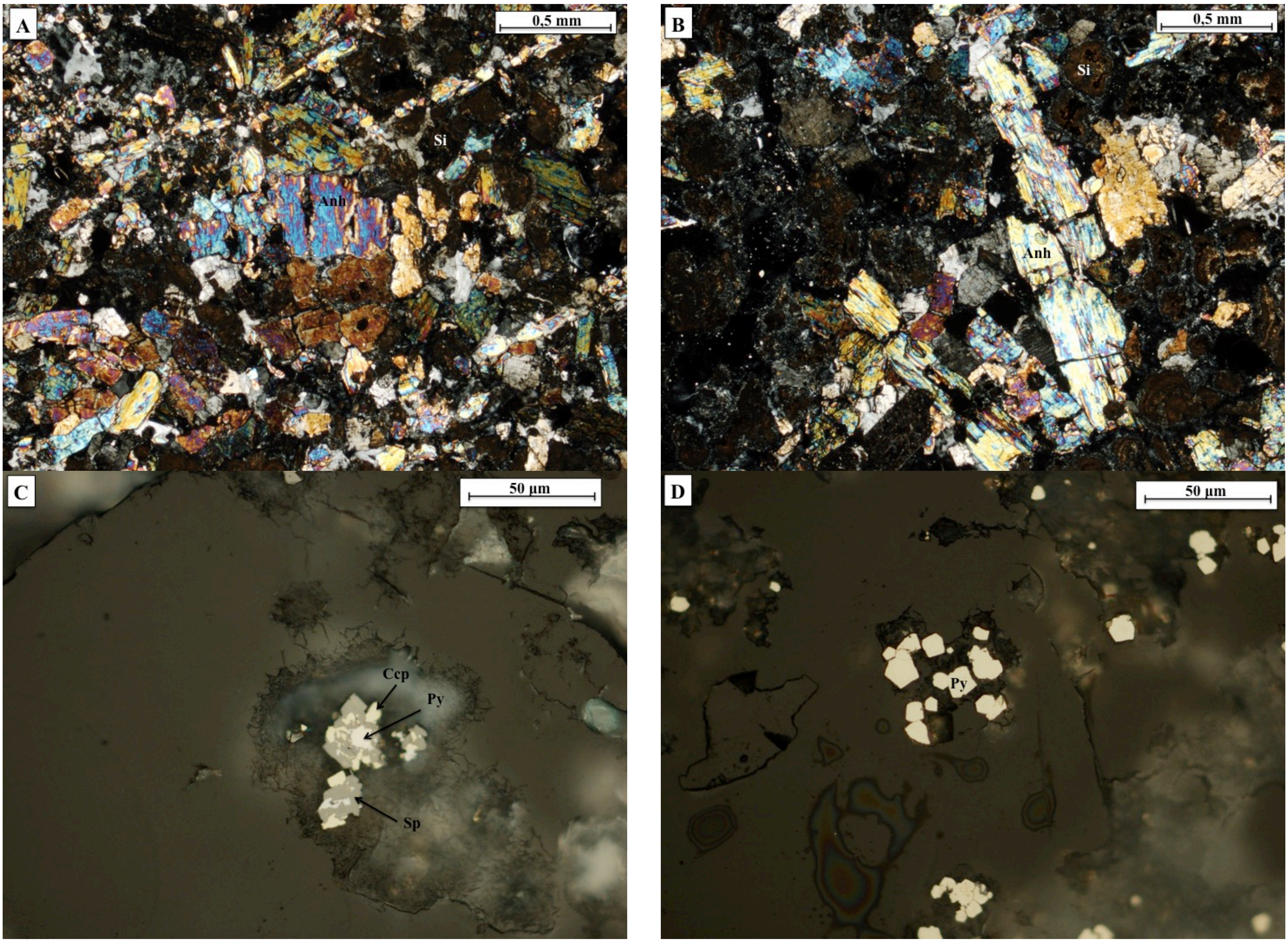

Figure 49: Picture A and B shows anhedral to subhedral tabular anhydrite crystals and patches of colloform silica. C shows the relationship between the sulphides in this sample initial formation of pyrite was followed by chalcopyrite and sphalerite. Galena is also found in this sample, and can be found in relations with sphalerite. D shows mineralizations of pyrite.

5.1.3.3 In-situ inactive chimney (GS16B-ROV7-R02)

This sample represents an inactive chimney still standing in-situ with no signs of venting. The chimney displays an outer rim of sulphide-sulphates that is light in colour, and a dark and sulphide-rich interior. Compared to all other samples in this study, this chimney is sulphide-rich as suggested by its dark colour and high density.

Figure 50: This picture shows the in situ inactive chimney. The material is dark and is relatively heavy compared to the other sampled material from this site.

GS16B-ROV7-R02-1: The main mineral phase in this thin section are barite followed by anhydrite, amorphous silica and sulphides. The barite crystals are euhedral and grow in either dendritic or acicular clusters of radiating crystals that are up to 0,7 mm thick, or as single well developed tabular crystals that are up to 0,5 mm long. The anhydrite crystals are subhedral to anhedral and are found as single grains amongst the barite crystals. They are around 250 µm long. The amorphous silica is colloform and forms large clusters that are up to 2 cm thick, or as concentrated nodules that are around 0,7 mm thick. Sulphide contents are estimated to be around 15% and are located mainly within the patches of silica. The dominant sulphide phase is pyrite followed by sphalerite, chalcopyrite and galena displayed in aggregates that occupy up to 50 µm. Pyrite and chalcopyrite formed first followed by sphalerite, as these phases can be found inside sphalerite crystals. Galena is occurs exclusively associated to sphalerite.

Photo A:

shot nr:	Mg	Al	Si	S	Cl	Ca	Sr	Ba	Fe	Cu	Mo	Zn	Ga	Int
1				20,14		1,06	3,43	75,37						Brt
2				19,19		0,25	1,77	78,78						Brt
3	9,7	0,39	88,51		0,27								1,13	Si
4	9,16	0,48	88,82		0,79				0,74					Si
5	7,43	0,31	83,76						2,31		6,19			Si
6				19,11		0,56	1,7	78,63						Brt
7	24,14	0,53	74,14			0,21			0,97					Si
8	22,77	0,63	75,45			0,28			0,87					Si
9	9,6	0,47	51,57	18,25		0,14			15,45	4,52				Py
10	8,51	0,22	51,63	13,97					12,82	1,65	9,09	2,1		Py
11	2,22	0,3	45,75	26,59					21,35	3,79				Py
12	3,98	0,14	30,45	22,14					2			41,29		Sp

Photo B:

shot nr:	Mg	Al	Si	S	Cl	K	Ca	Fe	Cu	Zn	V	P	Int
1	0,22	0,24	99,39		0,15								Si
2	4,08	0,36	95,02					0,55					Si
3	6,7	0,88	91,26		0,3	0,18		0,68					Si
4	0,29		0,95	52,39				46,12			0,25		Py
5	0,31		0,21	51,75				46,28	1,06		0,17	0,22	Py
6	0,15		0,64	51,58			0,08	45,65	1,67			0,23	Py
7	0,23		21,77	40,88				37,12					Py
8	0,33		0,22	52,68				44,88	1,66			0,22	Py
9	0,34	0,28	99,38										Si
10			0,52	45,95				33,17		20,36			Sp

Photo C:

shot nr:	Na	Mg	Al	Si	S	Cl	K	Ca	Sr	Ba	Fe	Int
1			0,06		19,52				1,45	78,97		Brt
2			0,45	95,46						4,08		Si
3	0,86	0,24	1,72	80,2	2,66	2,67	0,46	0,45		9,94	0,8	Si
4					19,31			0,84	2,07	77,78		Brt
5	1,12	0,13	0,92	67,42	5,55	1,2	0,35	0,68		22,64		Si
6			1,14	98,43			0,43					Si
7					19,66			0,5	2,24	77,6		Brt

Photo D:

shot nr:	Mg	Al	Si	S	Cl	K	Ca	Sr	Ba	Fe	Zn	Tc	Ga	Int
1	11,91	0,39	87,26		0,15	0,14	0,16							Si
2	17,87	0,56	80,47		0,14	0,3	0,14			0,53				Si
3	15,95	0,57	82,45			0,12	0,24			0,67				Si
4	4,82	0,34	81,05	3,27								9,72	0,81	Si
5	5,49	0,31	94,2											Si
6				18,76			0,31	1,76	79,17					Brt
7	14,41	0,38	82,61		0,68					0,6	1,32			Si
8	7,09	0,05	89,92							0,81	2,13			Si

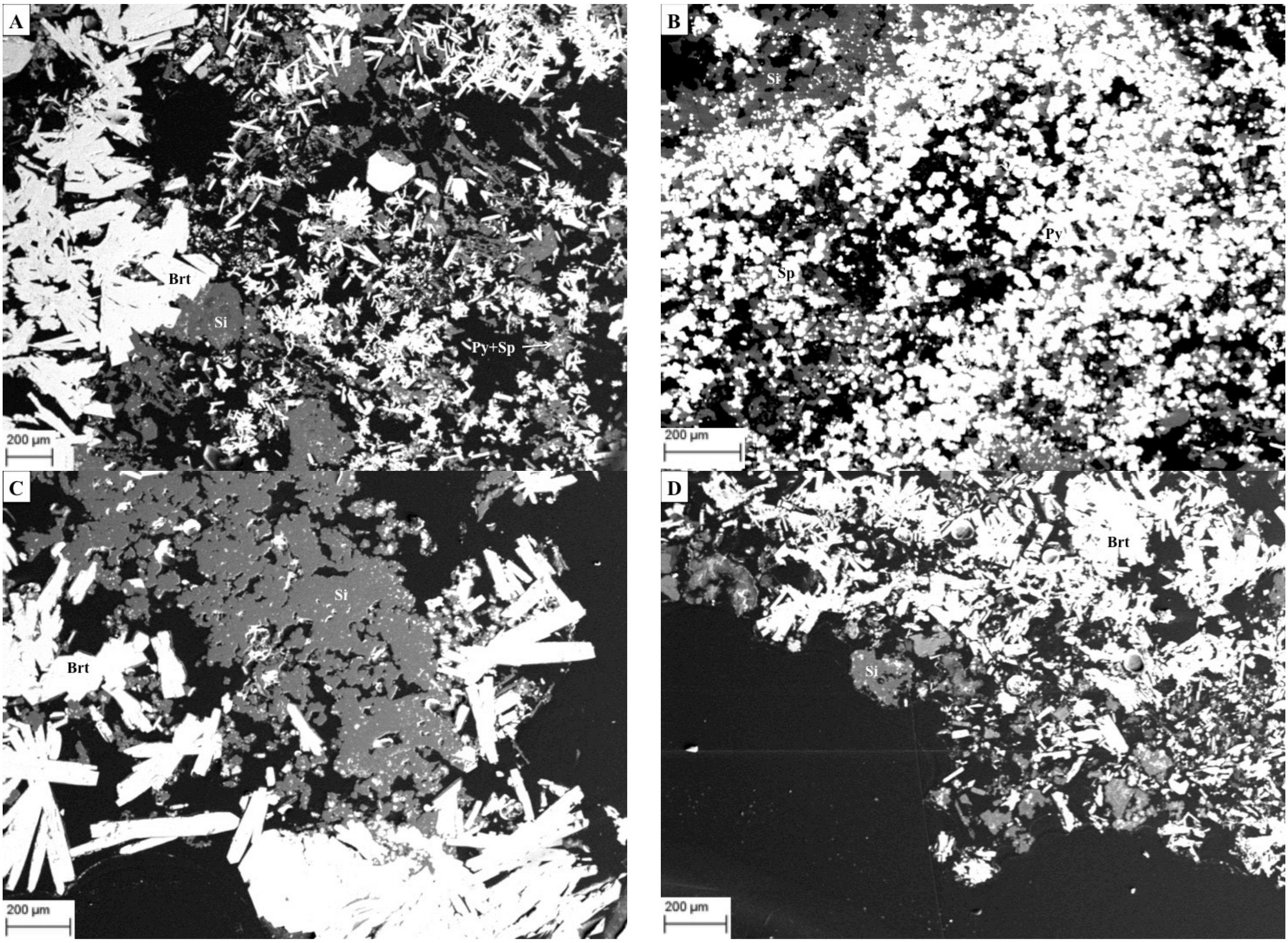

Figure 51: Picture A, C and D shows tabular or acicular crystals of barite, in the pore space abundant amounts of silica and sulphides have formed. B shows an area dominated by silica and abundant amounts of sulphides.

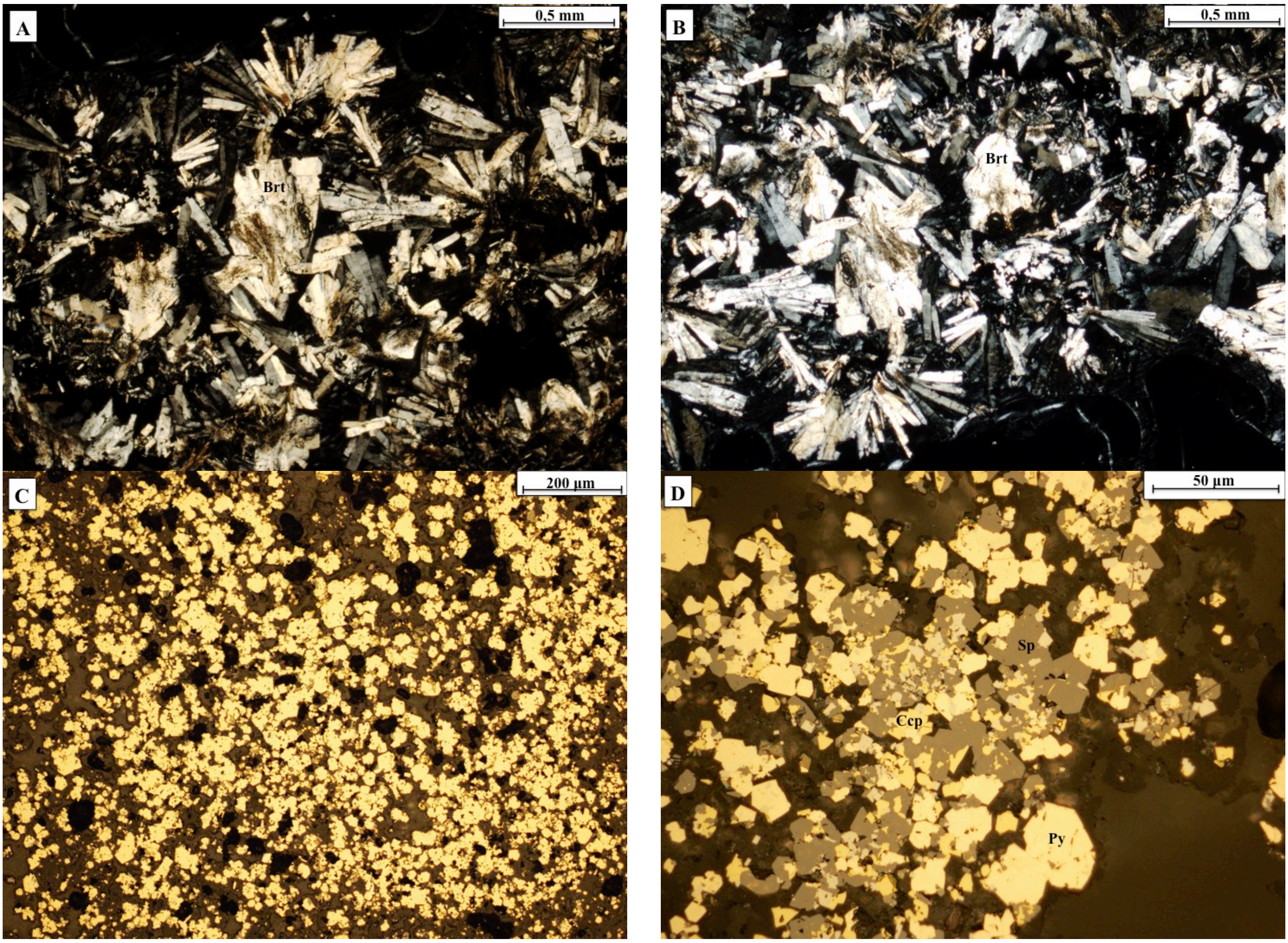

Figure 52: Picture A and B shows tabular or radiating cluster of acicular barite crystals. C shows one of the patches, which has abundant amounts of sulphides. D shows the relationship between the sulphides. Pyrite formed first followed by chalcopyrite and sphalerite, galena is found in association with sphalerite.

GS16B-ROV7-R02-2: The dominant mineral found in this thin section is amorphous silica followed by barite and sulphides. The amorphous silica displays colloform growth and makes up a continuous layer that stretches trough the thin section. Barite crystals are either dendritic or acicular and form radiating clusters that are up to 350 μm, or as single tabular crystals that are around 350 μm long inside the silica. The sulphides that represent approximately 10% of surface area in the thin section are found inside the silica layers, the main sulphide phase is pyrite followed by sphalerite, chalcopyrite and galena. Some of the single pyrite grains are up to 100 μm wide, and some of the clusters of different sulphide phases are up to the same size. In some areas sphalerite is the dominant sulphide phase .The sulfide paragenesis is identical to GS16B-ROV7-R02-1.

Photo A:

shot nr:	Mg	Al	Si	S	Cl	K	Ca	Fe	Cu	Tc	Zn	V	P	Mn	Int
1	30,98	0,52	66,26		0,57	0,34	0,23	1,11							Si
2	4,52	0,08	49,63	22,38	3,09			5,81	5,69	8,79					Ccp
3			0,22	53,46				45,31					0,24	0,76	Py
4	8,41	0,22	65,36	12,94	0,36			8,03	1,81		2,86				Si
5	0,91		0,18	51,07				47,45				0,17	0,21		Py
6	9,89	0,28	69,3	4,3	0,9			0,42		12,04	2,88				Si
7	5,71	0,19	92,05								2,05				Si
8	8,69	0,32	87,91		0,42			0,76			1,91				Si

Photo B:

shot nr:	Mg	Al	Si	S	Cl	Ca	Ba	Fe	Cu	Mo	Zn	Mn	Ga	Int
1	3,79	0,27	81,32	5,16							9,46			Si
2			0,76	18,49			80,76							Brt
3	4,96	0,12	91,47								2,02		1,43	Si
4				34,82				3,82			61,37			Sp
5				32,44				1,92			65,26	0,37		Sp
6	5,3	0,31	82,39	6,59		0,17		4,76	0,47					Si
7	2,49	0,36	96,38		0,19			0,58						Si
8	0,58	0,19	55,73	10,1	4,85		28,55							Si
9	4	0,28	91,66			0,2		1,2			2,65			Si
10	3,15	0,25	67,87	4,94				2,3	1,54	12,54	7,4			Si

Photo C:

shot nr:	Na	Mg	Al	Si	S	Cl	K	Ca	Ba	Fe	Cu	Mo	Zn	Se	Pb	Int
1	10,65	4,16	1,36	61,48	2,11		1,45	9,65	8,18	0,97						Si
2	9,22	3,54	1,25	55,69	4,06		1,35	8,84	14,84	1,22						Si
3			0,13	3,39	19,34			0,2	76,95							Brt
4		0,85	0,24	97,98		0,93										Si
5		5,65	0,34	93,5		0,51										Si
6					33,33					2,45			64,22			Sp
7		0,19		42,56	18,58	0,84				3,33	3,2	12,49	18,81			Ccp
8				7,2	10,18	1,02								0,52	81,08	Gn

Photo D:

shot nr:	Na	Mg	Al	Si	S	Cl	K	Ca	Sr	Ba	Fe	Zn	Int
1					18,71			0,15	1,11	80,03			Brt
2		23,26	0,56	70,38			0,19	0,48		4,05	1,07		Si
3		23,4	0,56	72,8		2,25	0,22				0,78		Si
4	0,82	21,41	0,33	73,86		3,31	0,27						Si
5		21,74	0,61	61,97	2,55	0,32		0,82		9,23	1,54	1,23	Si
6		24,47	0,29	71,57				0,39			1,13	2,15	Si
7		6,99		32,44	32,54	2,79				2,96	19,01	3,26	Py
8		4,32		71,8	5,68	18,2							Si
9		5,26		33,52	17,31	3,04				31,08	1,69	8,11	Brt
10		18,96	0,33	76,83				0,34			0,96	2,56	Si

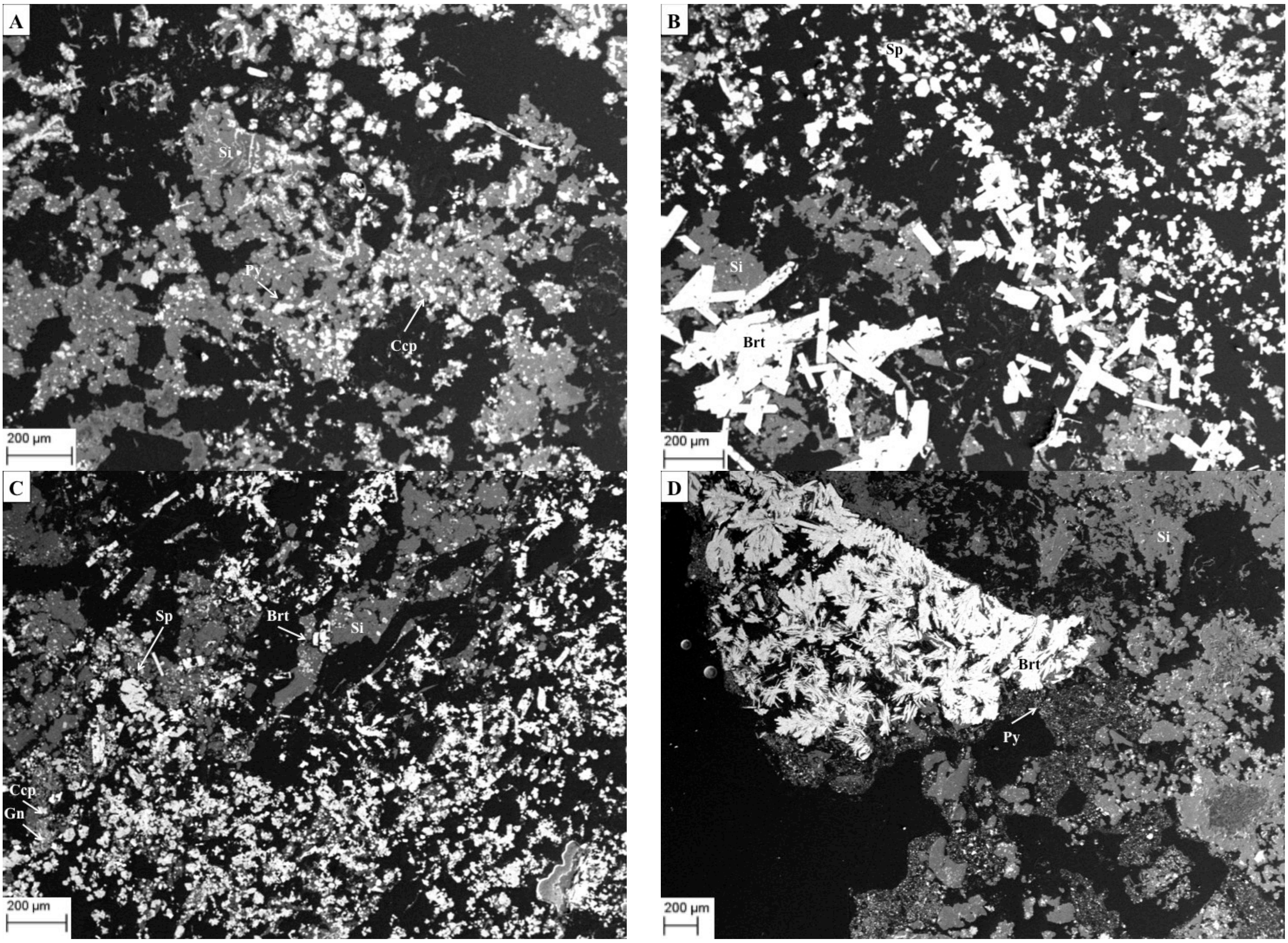

Figure 53: Picture A, B and C shows the same mineral assemblages as found in figure 52 and 51. D shows one of the patches with barite, which has clusters of acicular crystals.

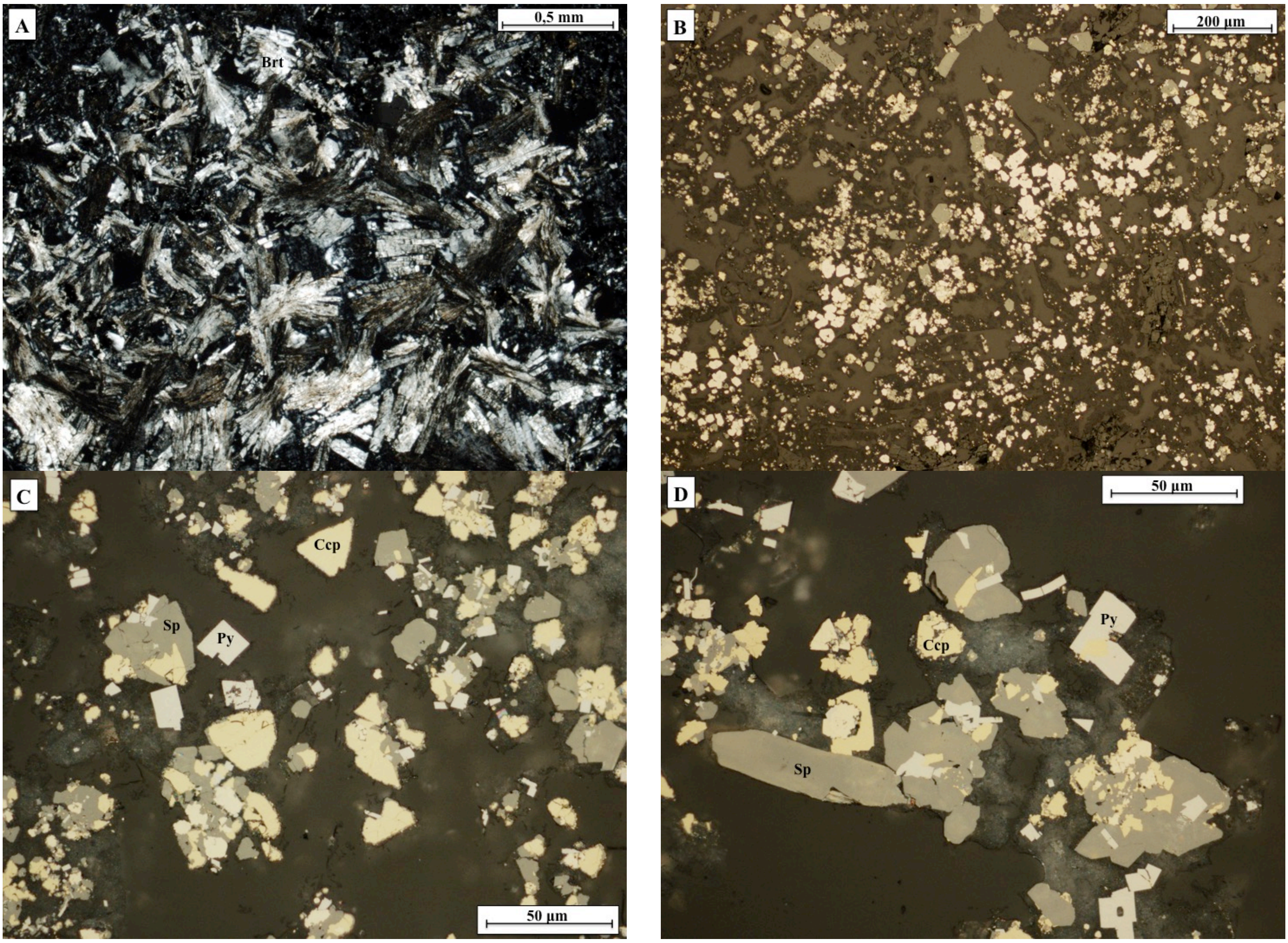

Figure 54: Picture A shows acicular or dendritic barite crystals. B shows a patch composed of silica and abundant sulphide. C and D show the sulphide assemblages which has the same relationship as seen in Figure 53 D.

5.1.3.4 Active chimney fragment (GS16B-ROV9-R01)

A portion taken from a large actively venting hydrothermal chimney has been sampled. The material is white to whitish grey, very porous and brittle. The sample is made up of mainly anhydrite and minor amounts of sulphides. Two representative thin polished sections were made from this active chimney.

Figure 55: Picture of a fragment taken from the sampled active chimney. The sample has a light colour and is mainly composed of anhydrite.

GS16B-ROV9-R01-1: The main mineral phase in this thin section is anhydrite followed by barite, amorphous silica and sulphide. The anhydrite crystals are euhedral to subhedral and mainly shows two dominant crystal sizes. One size has crystals of up to 200 µm and are found in grainy masses, the other grain size is found in veins or orifices is larger with well developed crystals of up to 4mm in length. Barite crystals are euhedral and grow as dendritic or acicular radiating clusters with a thickness of around 100 µm. The amorphous silica has colloform growth and is found in patches that are up to 2 mm thick. It can also be found in veins and orifices where it has precipitated around crystals. The sulphide content of the sample is very low with an estimate of less than 1%. Pyrite is the dominant sulphide phase followed by sphalerite, chalcopyrite and galena. Sphalerite is the dominant mineral phase in some areas of the sample, but the content does not exceed that of pyrite. Pyrite and chalcopyrite formed first followed by sphalerite, as these phases can be found inside sphalerite crystals. Galena is exclusively found included in sphalerite.

Photo A:

shot nr:	Mg	Al	Si	S	Cl	Ca	Sr	Fe	Int
1		0,03		44,32		55,64			Anh
2				43,46		56,54			Anh
3	32,26	2,68	59,76			2,15		3,15	Si
4				43,55		55,28	1,17		Anh
5	30,22	2	61,61		2,32	1,59		2,26	Si
6	31,35	2,46	60,71		2,57	1,05		1,85	Si

Photo B:

shot nr:	Mg	Al	Si	S	Cl	Ca	Ba	Fe	Cu	Zn	Mn	Int
1	0	0,1	0,49	36,22	0,3			3,71		58,71	0,47	Sp
2	10,47	1,33	15,85	28,71		0,6		23,69	19,34			Ccp
3			0,38	33,2	0,83			4,37		61,21		Sp
4	0,9	0,2	1,82	33,22	0,73			4,19		58,93		Sp
5			0,32	31,52				6,34		61,07	0,76	Sp
6				35,47				5,09		58,79	0,65	Sp
7	3,84		8,09	45,77	22,33			5,18		14,79		Sp
8	24,49	4,29	42,99	6,75		2,47		6,37	0,87	10,95	0,82	Sp
9	25,83	3,29	44,42	9,69		1,7		5,47	1,88	7,74		Si

Photo C:

shot nr:	Mg	Al	Si	S	Cl	K	Ca	Fe	Cu	Mo	Zn	Mn	Pb	Int
1				38,35				15,37			45,58	0,71		Sp
2				28,81				6,41		13,19	51,05	0,54		Sp
3	0,15		0,33	35,75				30,75	31,55		1,48			Py
4				38,93				14,44			46	0,63		Sp
5	11,48	1,06	15,61	1,47	6,67		0,48	2,13					61,1	Gn
6	24,05	3	56,8	1,65	7,35		1,93	5,22						Si
7	28,09	3,51	52,6		1,03		1,84	4,41		6,28	2,24			Si
8	27,26	3,9	51,33	5,9	2,65	0,27	2,23	6,46						Si

Photo D:

shot nr:	Mg	Al	Si	S	Cl	Ca	Sr	Fe	Cu	Zn	V	Se	Pb	Int
1	28,05	1,79	54,43	1,43	10,95	0,82		2,53						Si
2				38,12				19,07	17,49	25,32				Sp
3			0,41	58,11	4,22			2,88		34,38				Sp
4				51,74				5,03		43,23				Sp
5				33,97				5,07		60,79	0,16			Sp
6							0,54			1,82		0,6	97,03	Gn
7	0,54		1,41	44,26	1,45	1,27		2,68	0,69	47,7				Sp
8					0	0,19	0,39			1,54		0,76	97,13	Gn
9	0		0,28	35,63				6,19		57,89				Sp
10	26,67	2,51	57,5	3,1	5,67	1,43		3,12						Si

Photo E:

Shot nr:	S	Ca	Sr	Ba	Int
1	43,59	56,41			Anh
2	19,54	0,28	2,97	77,21	Brt
3	19,98	0,54	4,76	74,72	Brt
4	31,21	29,3	1,18	38,32	Brt

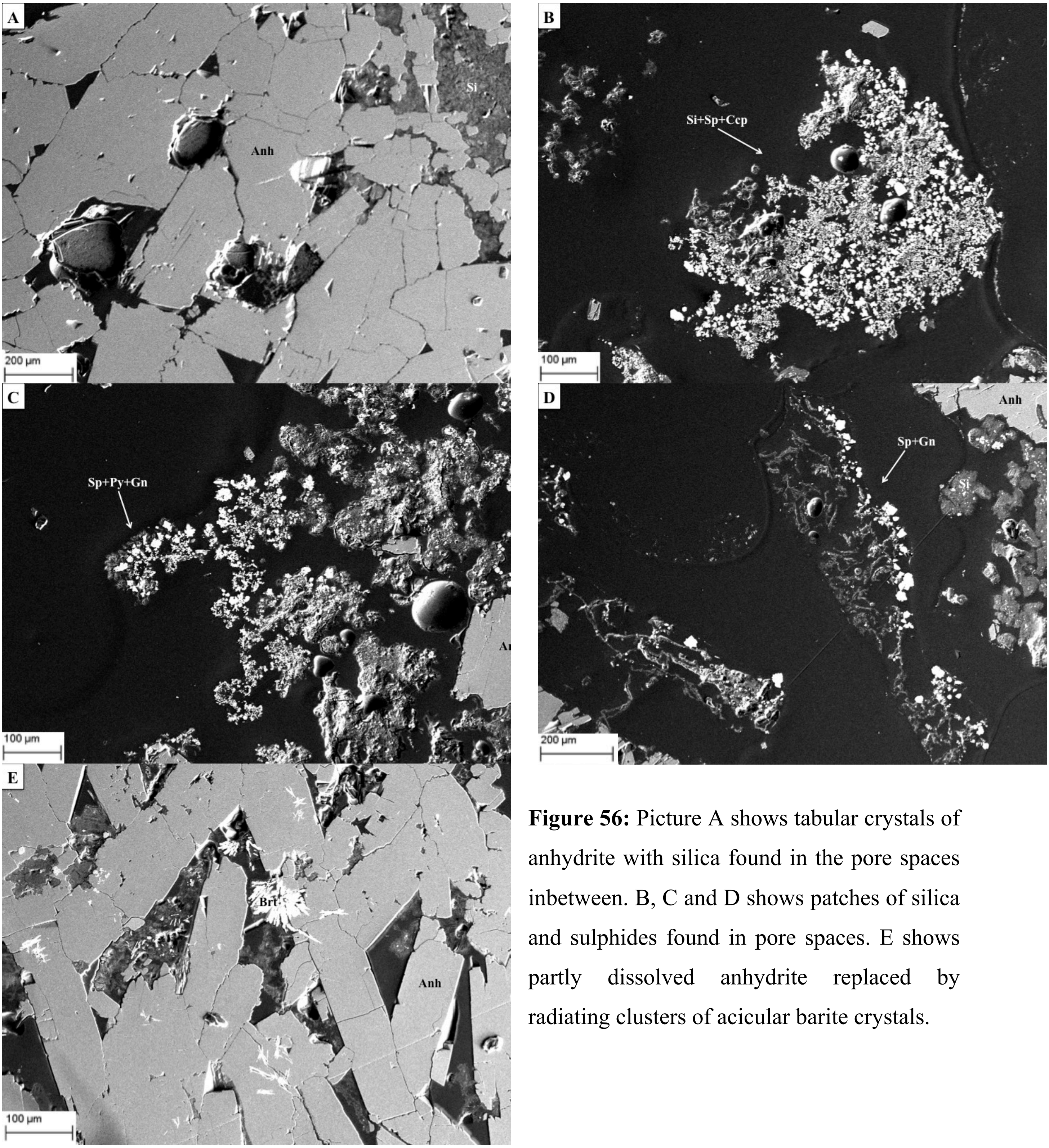

Figure 56: Picture A shows tabular crystals of anhydrite with silica found in the pore spaces inbetween. B, C and D shows patches of silica and sulphides found in pore spaces. E shows partly dissolved anhydrite replaced by radiating clusters of acicular barite crystals.

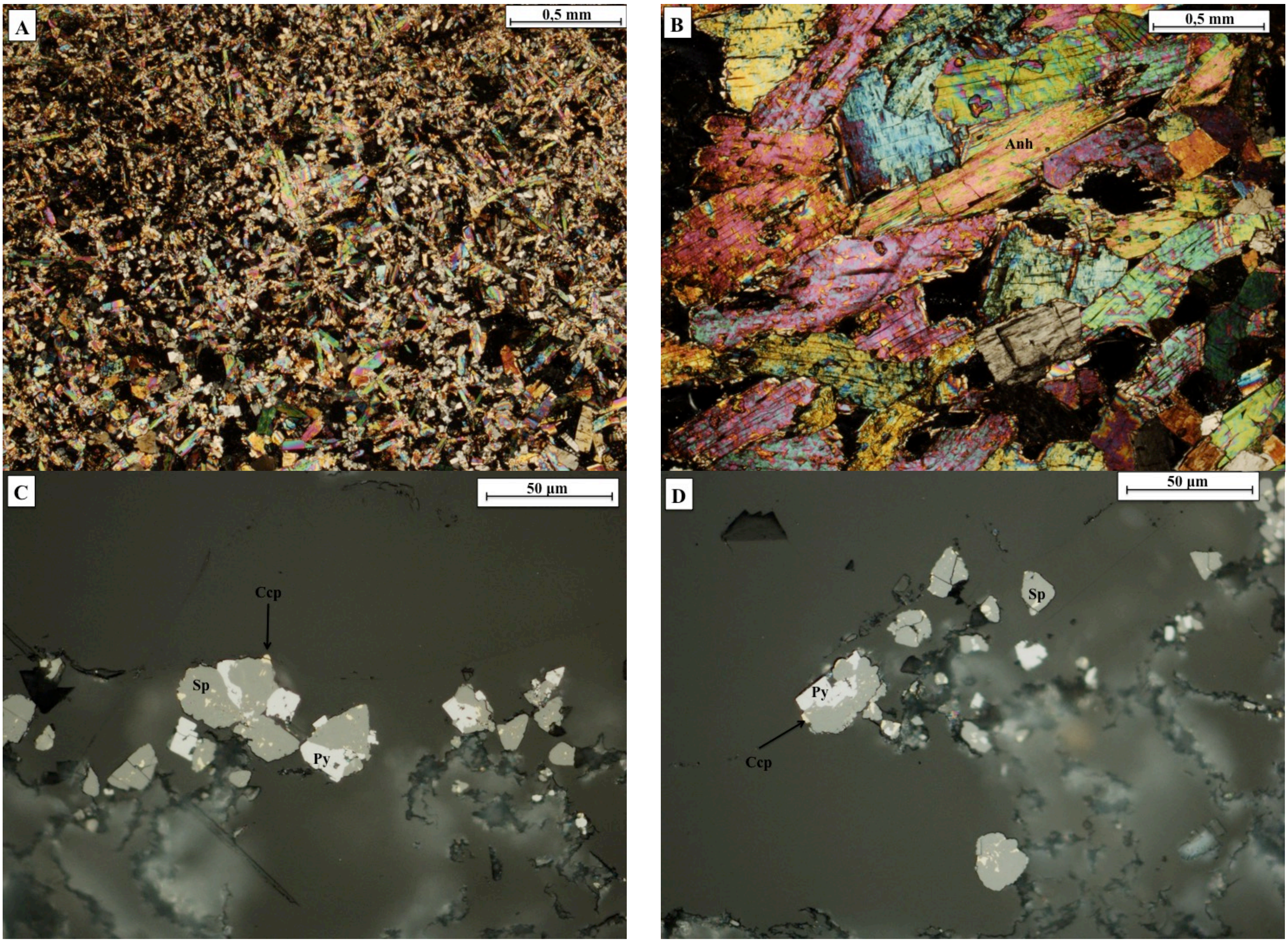

Figure 57: Picture A and B shows the difference seen in the size of the barite crystals. Picture C and D shows the relationship between the sulphides. Initial pyrite was followed by chalcopyrite and sphalerite, galena is exclusively found in association with sphalerite.

GS16B-ROV9-R01-2: The main mineral phase in this thin section is anhydrite followed by barite, amorphous silica and sulphide. The anhydrite crystals are euhedral to subhedral and are up to 3 mm long, while most of the crystals in the thin section are around 200-500 µm long. The barite crystals are either dendritic or acicular. Some of the crystals grow in radiating clusters that are up to 300 µm thick. Barite crystals are euhedral and grow as dendritic or acicular radiating clusters with a thickness of around 200µm. The amorphous silica is colloform, and is found in patches that are up to 0,5 cm or in veins or orifices where it is precipitated around anhydrite crystals. There is a small amount of sulphides in the sample, not exceeding 1% or surface area. These sulphides are predominantly pyrite with lesser amounts of chalcopyrite, sphalerite and galena. Some areas of the thin section contain sphalerite-rich domains, but the overall content of it does not exceed that of pyrite. The sulphides appear in clusters that are up to 20 µm thick. The sulphide paragenesis is identical to those in GS16B-ROV9-R01-1.

Photo A:

shot nr:	Na	Mg	Al	Si	S	Cl	Ca	Fe	Cu	Zn	Mn	Ta	Int
1		30,84	2,45	61,53		2,39	0,88	1,92					Si
2		30,95	2,34	61,77		2,55	0,6	1,79					Si
3		0,86		1,1	52,08			41,47	1,82	2,19		0,49	Py
4		3,95	0,15	4,68	48,62			40,69	1,42		0,49		Py
5		28,39	2,47	56,11	3,87	1,68	0,88	3,73		2,06	0,8		Si
6		18,43	1,21	25,51	19,06	0,69	0,81	6,59	2,47	25,24			Sp
7		1,27	0,13	2,06	43,83		1,33	28,03	3,53	19,23	0,58		Sp
8		11,29	0,81	14,99	23,58	0,45	0,6	11,46	4,19	31,88	0,74		Sp
9		29,82	2,86	58,48	0,64	0,65	1,49	3,41		1,95	0,7		Si
10	0,94	30,45	2,76	59,24		0,74	1,37	3,89			0,61		Si

Photo B:

shot nr:	Mg	Al	Si	S	Cl	Ca	Sr	Ba	Fe	Cu	Zn	Ta	Int
1				44,16		55,84							Anh
2				44,37		55,63							Anh
3				19,51		0,36	2,99	77,14					Brt
4				18,85		0,3	2,15	78,7					Brt
5	0,39	0,11		19,3			3,41	76,8					Brt
6	2,71		6,02	23,46	10,78	4,07		52,95					Brt
7	6,58	0,54	10,4	27,28	4,6	17,77		31,93	0,9				Brt
8	15,43	1,81	27,52	21,28	11,06	22,88							Si
9	6,62	0	8,07	47,21					33,16	1,68	2,49	0,78	Py

Photo C:

shot nr:	Na	Mg	Al	Si	S	Cl	Ca	Ba	Fe	Cu	Zn	Mn	Int
1					54,21				45,28			0,51	Py
2		0,83	0,26	1,66	51,13				41,45	1,77	2,89		Py
3	1,21	0,17			52,1				44,8	1,72			Py
4		0,19		2,83	50,06				46,02	0,89			Py
5		0,25		0,55	52,1				46,4	0,7			Py
6		0,97	3,36	6,85	50,42	5,57	0,78		32,04				Py
7		0,03		0,18	53,3				44,45	2,03			Py
8		0,84	0,65	5,66	47,55	2,02	0,46	5,42	35,18	2,21			Py
9				0,1	43,36				17,69		38,32	0,52	Sp
10		10,07	3,57	19,93	42,51	3,59	0,4		19,93				Py

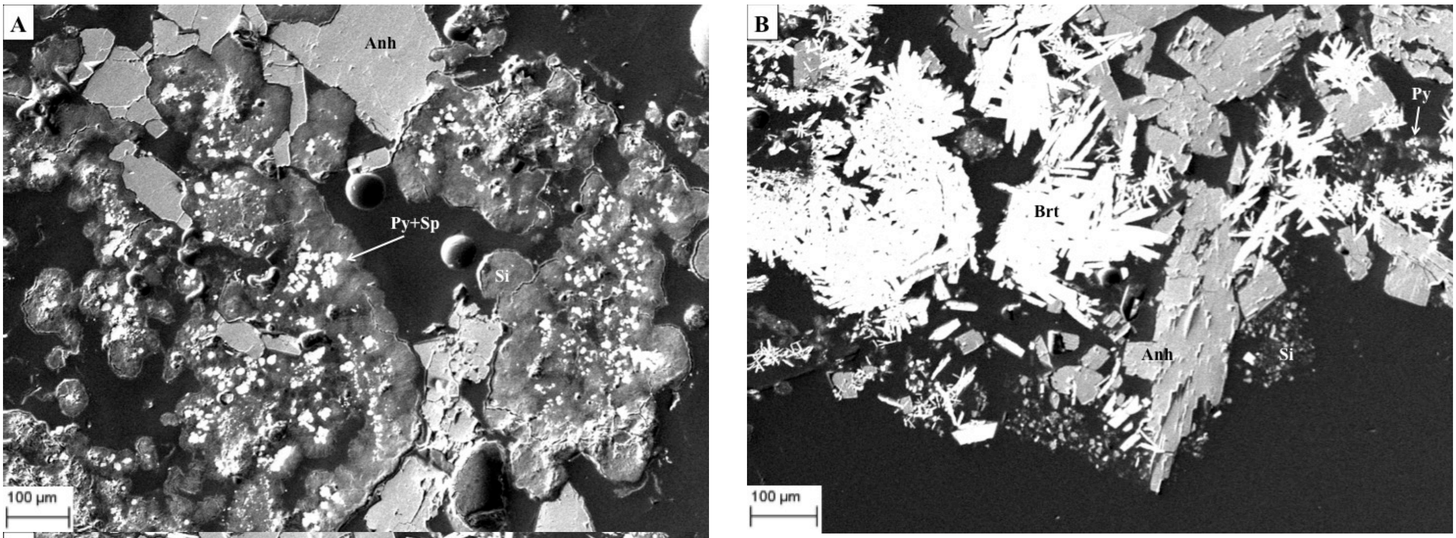

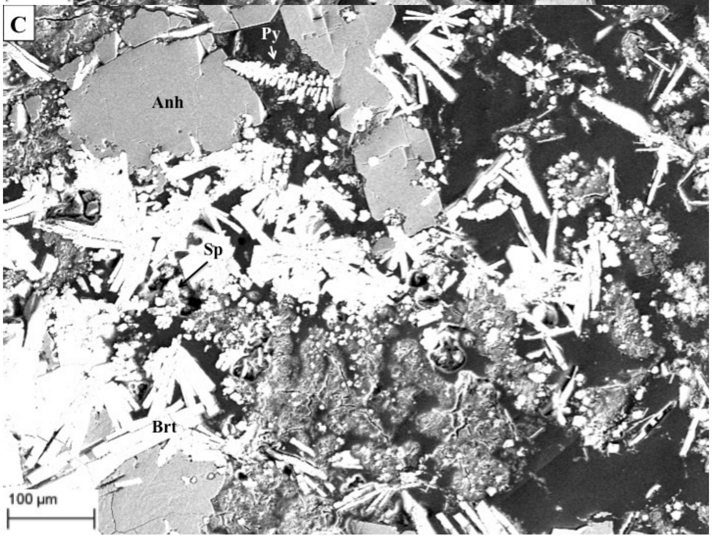

Figure 58: Picture A shows tabular anhydrite crystals coated by colloform silica. Sulphides are found in association with the silica and can be seen included. B and C show the mineral assemblages seen in A with the exception of radiation clusters of acicular barite crystals.

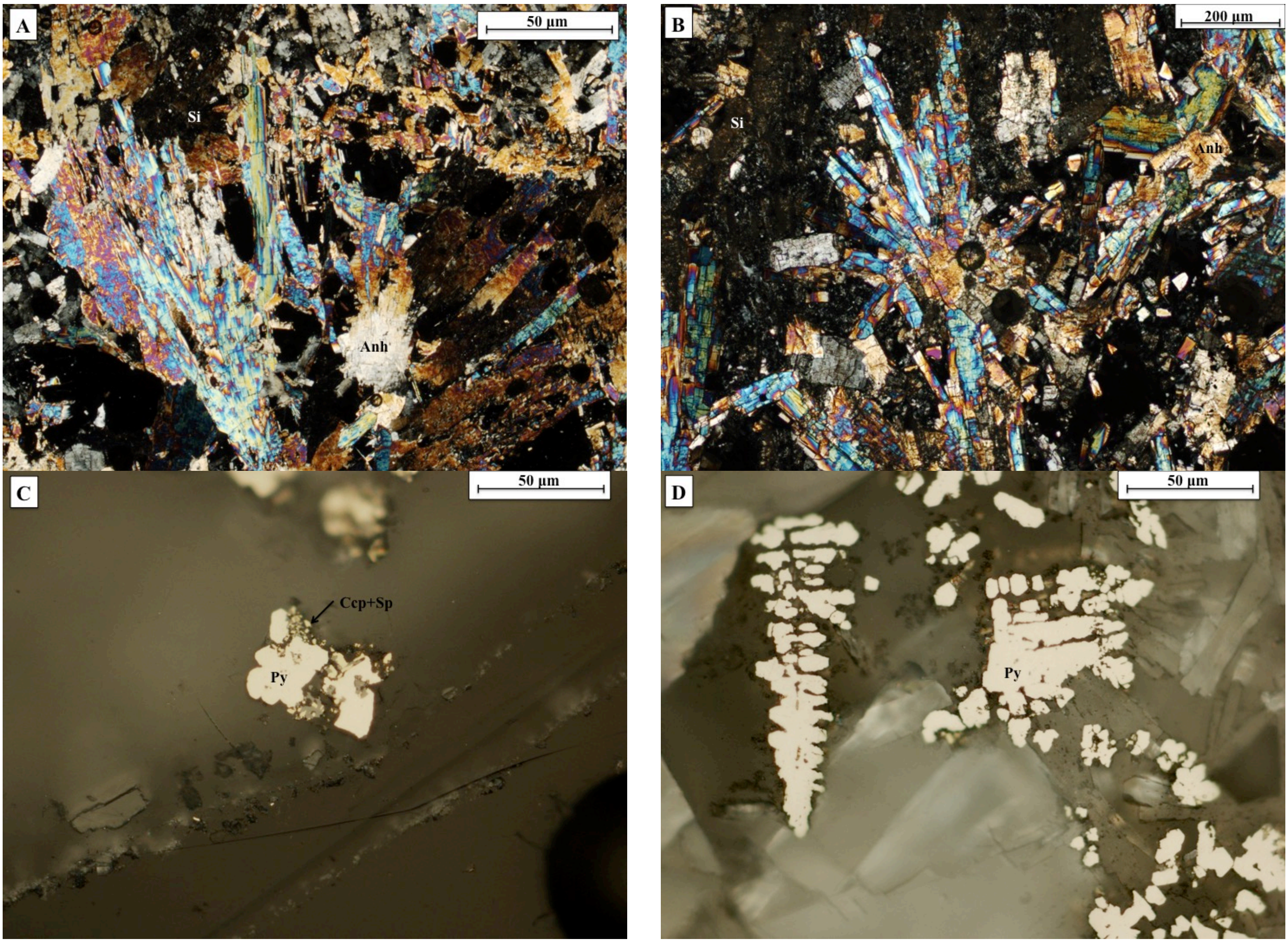

Figure 59: Picture A and B shows anhedral to subhedral tabular or acicular anhydrite crystals and patches of colloform silica. C and D show the sulphide assemblages found in the thin section, which is identical to that found in figure 57.

5.2 Geochemistry

Sample ID	δ34S (‰)	$^{87/86}$Sr	87/86Sr Error
GS14-ROV7B-R01	21,3	0,704322	0,000008
GS14-ROV7B-R02	20,7	0,704409	0,000009
GS14-ROV8-R01	21,5	0,705616	0,000009
GS15-AGR10-R2-Inner	-	0,707196	0,000007
GS15-AGR10-R2-Outer	-	0,707714	0,000009

Figure 60: Table with measured isotopic values for δ34S, and $^{87/86}$Sr isotopic ratios.

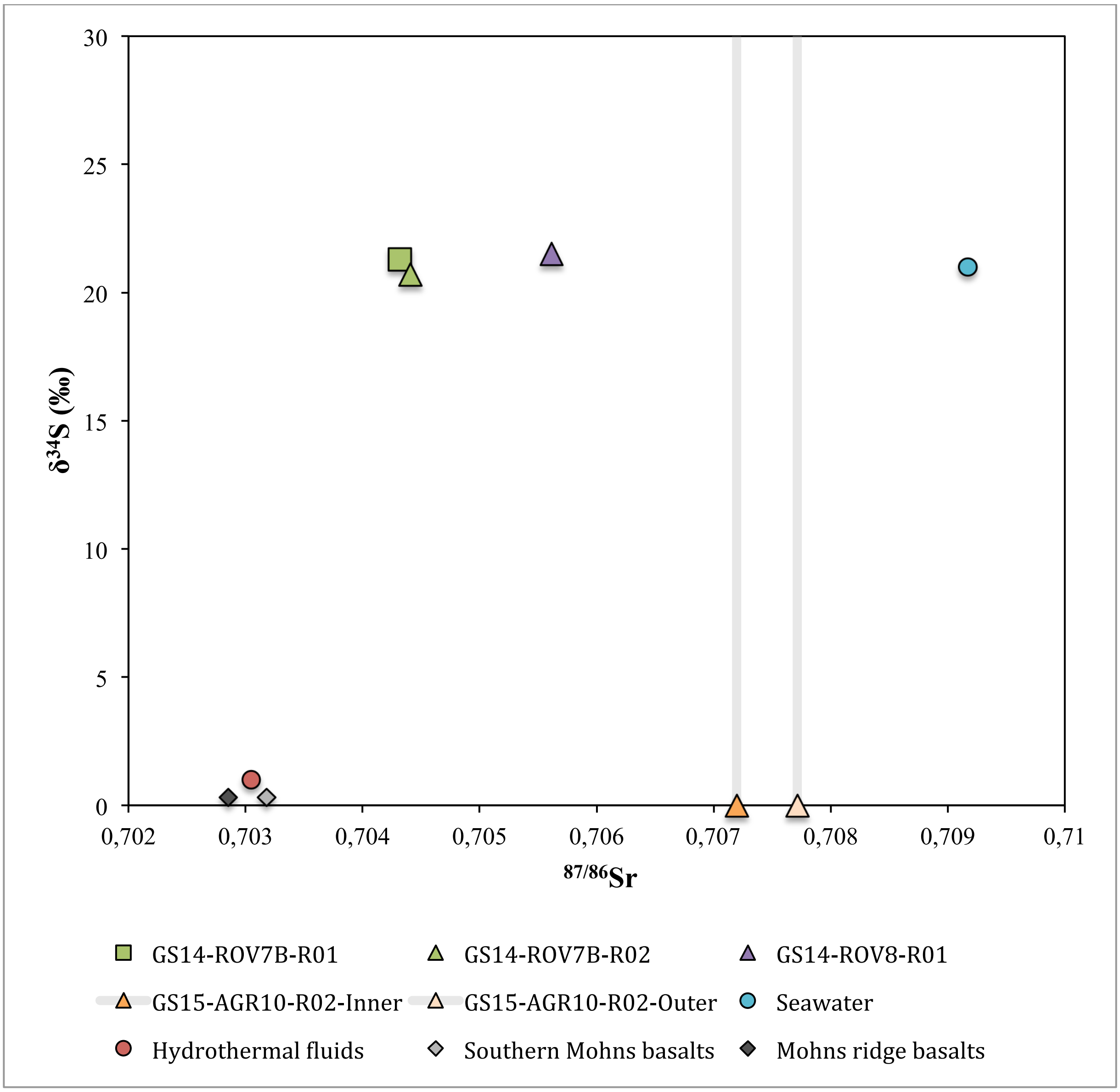

Figure 61 (Previous page): Figure with the plotted sample values of $\delta^{34}S$ (‰) versus $^{87/86}Sr$, as well as; Seawater values for $\delta^{34}S$ (21,5‰) (Kusakabe et al., 1990; De Ronde et al., 2003; Eickmann et al., 2014), and $^{87/86}Sr$ (0,70917) (Eickmann et al., 2014); End member hydrothermal fluids with $\delta^{34}S$ values of 1-2‰ (Griffith et al., 2012), and $^{87/86}Sr$ with an isotopic ratio of 0,70305 (Eickmann et al., 2014); Basalts of mid ocean ridge type with $\delta^{34}S$ values of 0,3±0,5 (Sakai et al., 1984), and $^{87/86}Sr$ values found on Southern segment of Mohns ridge 0.703505-0.703178 (Svellingen and Pedersen, 2003), and along Mohns ridge 0,702853-0,703212 (Schilling et al., 1999). GS15-AGR10-R02-inner and outer has not been analysed for $\delta^{34}S$ values, as indicated by the line telling it could be anywhere along the path. Error for $^{87/86}Sr$ analysis is thought to be equal to the size of the value mark.

5.2.1 Strontium isotopes

$^{87/86}Sr$ isotopes are used to determine the fluid composition of what the crystals precipitated from. Since you have two different end members of fluids, being the hydrothermal fluids with an $^{87/86}Sr$ value of 0,70305 and modern seawater with a value of 0,70917 (Eickmann et al., 2014). Since you have the two end members of fluids that can determine the $^{87/86}Sr$ values of the precipitated crystals in the hydrothermal deposits it is possible to determine the degree of mixture between seawater and hydrothermal fluids (Misra, 2012; Eickmann et al., 2014). The $^{87/86}Sr$ isotopic ratios in whole rock samples were determined for samples listed in figure 60, and are plotted against $\delta^{34}S$ values in figure 61. Plotted in this figure are also $^{87/86}Sr$ isotopic ratios for basalts in the Southern segment of Mohns ridge 0.703505-0.703178 (Svellingen and Pedersen, 2003), and along the Mohns ridge 0,702853-0,703212 (Schilling et al., 1999). The active chimney from Perle vent field has an $^{87/86}Sr$ value of 0.705616 (GS14-ROV8-R1). Bruse vent field samples show lower $^{87/86}Sr$ values of 0.704322 for the feeder structure (GS14-ROV7B-R1) and 0.704409 for the active chimney (GS14-ROV7B-R2). $^{87/86}Sr$ isotopic ratios from the fallen inactive chimney at Ægir gave $^{87/86}Sr$ values that are 0.707196 for the inner part, and slightly higher 0.707714 for the outer part of GS15-AGR10-R2. All the samples show a varying degree of mixture between hydrothermal fluids and seawater. The Perle and Bruse vent field show lower degree of mixing than the Aegir vent field. Aegir vent field show a higher degree of mixing with seawater with $^{87/86}Sr$ values closer to reference value of modern seawater. The outer parts of the Aegir sample has also values closer to seawater than the inner parts, which is most likely due to the minerals that are formed in the outer parts of the chimney being in contact with more seawater that could penetrate into the chimney walls. The inner parts on the other hand being less affected by this, reflected in $^{87/86}$Sr values closer to the hydrothermal fluid end member. The $^{87/86}$Sr isotopic ratio varies for the samples that were analysed. During the digestion steps of the samples barite would have to be removed, as it would not dissolve during the digestion steps. During the digestion of the samples barite was only in visible amounts in the Bruse samples (GS14-ROV7B-R1 and GS14-ROV7B-R2), but could be found in the other samples in trace amounts. This could influence the measured $^{87/86}$Sr isotopic values of the samples as Sr readily substitutes for Ba in the crystal lattice of the barite crystals as barite forms in solid solution between the end member barite $BaSO_4$ and $SrSO_4$ (Hanor, 2000). Since the barite fraction is removed from the Bruse samples the isotopic values might differ from the whole rock composition if barite was also measured.

5.2.2 Sulphur isotopes

Barite separates from Perle and Bruse samples have been analysed for sulphur isotopes to determine if the origin of the sulphur in the samples comes from hydrothermal H_2S or seawater SO_4. The feeder structure at Bruse has a $\delta^{34}S$ value of 21.3‰ (GS14-ROV7B-R1), slightly higher than the $\delta^{34}S$ 20.7‰ of the active chimney (GS14-ROV7B-R2). The active chimney at Perle has a $\delta^{34}S$ value of 21.5 (GS14-ROV8-R1). Seawater sulfate has $\delta^{34}S$ values of +21.5 ‰ (Kusakabe et al., 1990; De Ronde et al., 2003; Eickmann et al., 2014), and magmatic derived hydrothermal fluid with $\delta^{34}S$ values from 1-2 ‰(Griffith et al., 2012). Values in all samples are close to seawater sulphate indicating seawater sulphate as the main source of S in these phases. Slightly lower values observed in the Bruse active chimney suggest some degree of mixing with hydrothermal fluid.

5.2.3 Radiometric dating of barite

Sample ID	**Age (Years)**
GS14-ROV7B-R1-#1: Top	840±40
GS14-ROV7B-R1-#2: Centre	680±40
GS14-ROV7B-R1-#3: Grey core	1400±50
GS14-ROV7B-R1-#4: Grey spot	880±40
GS14-ROV7B-R2	8,7±0,3
GS14-ROV8-R1	7,4±0,4

Figure 62: Ages determined by radiometric dating of barite, given with the error for each respective sample. In Figure 63 it is illustrated where each dating is done in the GS14-ROV7B-R1.

Figure 63: Picture of the dated material from feeder structure, values for each spot is found in figure 62. Samples were taken from the chimney top, centre, grey core and a grey spot within the chimney. From ^{226}Ra/Ba dating it is found that the chimney top is 840±40 years old, the centre of the chimney is 680±40 years old, the grey core is 1400±50 years old and the grey spot is 880±40 years old.

Radiometric dating was done in barite-dominated samples from Perle og Bruse (GS14-ROV7B-R1, GS14-ROV7B-R2 and GS14-ROV8-R1) by using ^{228}Ra/^{226}Ra, ^{228}Th/^{228}Ra and ^{226}Ra/Ba. The sampled material falls into two groups, one with the oldest barite components and one with the most recent mineralizations. The sampled material consisted of barite and sulphides with the exception of GS14-ROV8-R1 that also contained anhydrite. Four samples were taken from the zoned feeder structure (GS14-ROV7B-R1) that overall shows a mineralization age around 800 years with the oldest barite being around 1400 years old. The feeder structure shows the oldest ages in the central parts of the sample, and decreasing ages outwards indicating that the structure has had a growth outwards (See figure 62 and 63). The age varies considerably from 1400±50 to 680±40, there are no recent mineralizations dated for this sample indicating a coherent age gradient from the inner parts and outwards. The active chimneys from Bruse (GS14-ROV7B-R2) and Perle (GS14-ROV8-R1) display the most recent mineralisation events with 8.7±0.3 and 7.4±0.4 years, respectively. With almost identical age these two vents shows different sizes.

5.2.4 Bulk chemical data

Sample ID	GS14-ROV7B-R1-Outer	GS14-ROV7B-R1-Inner	GS14-ROV8-R01	GS15-AGR10-R2-Inner	GS15-AGR10-R2-Outer	GS16B-ROV7-R01	GS16B-ROV7-R02	GS16B-ROV9-R01
	ppm	ppm	ppm	ppm	ppm	ppm	ppm	ppm
Al	1587	1566	221	2753	1143	2748	186	1308
Cu	899	887	1125	629	177	1037	2883	492
Fe	1959	1867	5730	3935	1496	3848	9535	2601
Zn	1886	1764	3340	1209	193	1500	9603	390
Pb	386	449	21	745	117	1540	2644	241
K	1583	1491	1589	2083	1796	1786	1787	1841
Mg	153	151	317	49436	26952	47335	6237	20968
Na	342	211	134	4195	2897	2653	1223	2458

Figure 64: Table over elements analysed with ICP-OES.

Sample ID	GS14-ROV7B-R1-Outer	GS14-ROV7B-R1-Inner	GS14-ROV8-R01	GS15-AGR10-R2-Inner	GS15-AGR10-R2-Outer	GS16B-ROV7-R01	GS16B-ROV7-R02	GS16B-ROV9-R01
	mg/kg	mg/kg	mg/kg	mg/kg	mg/kg	mg/kg	mg/kg	mg/kg
Mo	60,47	59,86	0,55	0,2	0,12	0,26	54,75	0,13
Ag	7,02	12,63	0,66	1,5	0,7	0,07	66,26	0,14
Sb	37,19	37,65	1,19	0,51	0,31	0,53	41,03	0,64
As	40,93	43,04	4,58	8,14	7,22	6,47	160,67	2,98

Figure 65: Table over elements analysed with HR-ICP-MS. The elements in the table are measured for the following isotope species; Mo98, Ag109, Sb123 and As75.

The bulk chemical analysis done in-house at UIB encountered some problems with digestion reflected in the table of analyses (Figure 64 and 65), and does therefore not have all elements analysed that are found in the samples. Some of the elements from the ICP-OES analysis (Figure 64) have no detection limit, which can give incorrect values. The elements that were missing detection limit were K, Mg and Na. Certain elements are also off on some of the reference standards, and so the values given for the ICP-OES analysis might not be correct. But it gives an impression of at what degree the elements are present in the samples, and should be of good enough quality to compare the samples. There were also problems with the HR-ICP-MS (Figure 65), as it is not certain that the reference standards CCU-1D and CZN-4 are suitable both for control of the measured elements but also for the digestion methods that were used. During analysis Ag had possible interference from Nb. Sb had possible interference from Cu or Fe species, and Mo and As had possible interference from Cu species. This interference problem might mostly be a problem for the CCU-1D standard, as it contains 30wt% Cu, this might be less of a problem for the samples as they do not contain nearly as much Cu which likely causes less interferencs. However as for the ICP-OES analysis, the HR-

ICP-MS analysis gives an impression of what degree the elements are found in the samples, and should be good enough for a comparison of the samples.

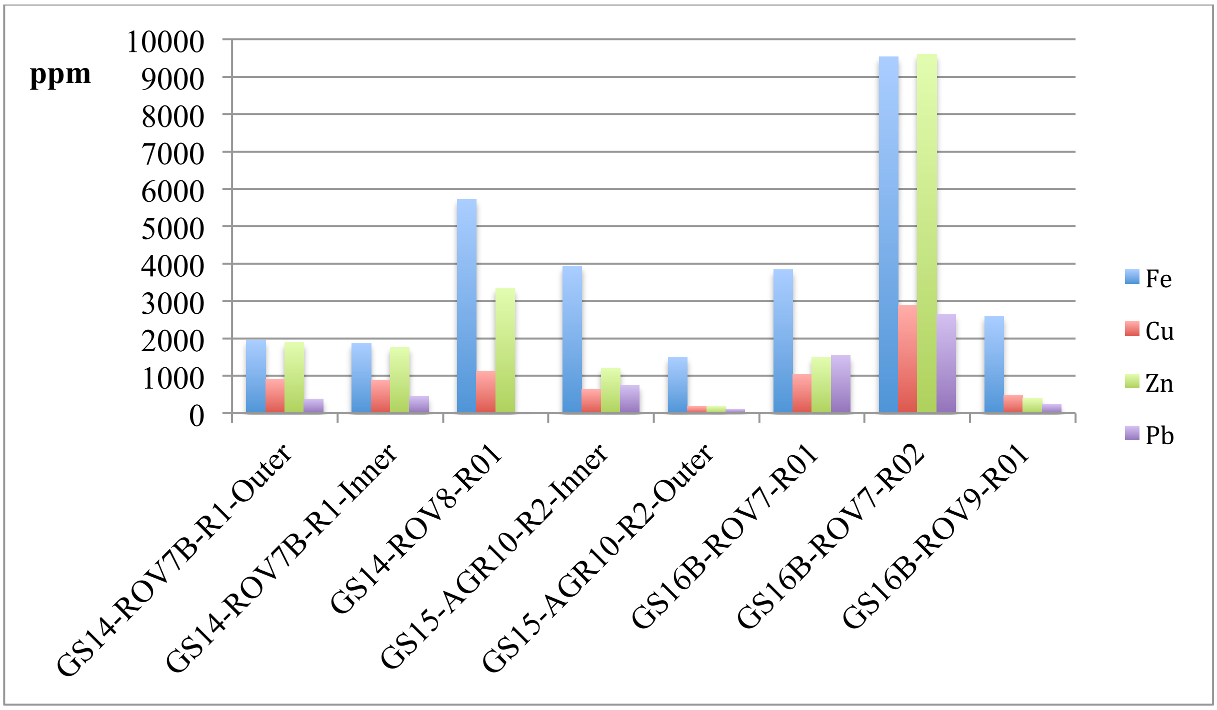

Figure 66: Diagram showing the amount (in ppm) of Fe, Cu, Zn and Pb for the samples.

The samples have a large variation in the amount of elements Fe, Cu, Zn and Pb as shown in Figure 66, and Figure 67. The amounts of these elements reflect the amount of sulphides in the samples with Fe for pyrite, Cu for chalcopyrite and covellite, Zn for sphalerite and Pb for galena. Bruse feeder structure (GS14-ROV7B-R1) shows almost identical amounts of the outer and inner part, which indicates that the colour variation seen in the sample might not be an indication of big variances in the composition and enrichment of sulphides found in the sample. Perle active chimney (GS14-ROV8-R01) has higher amounts of Fe, Cu and Zn but lower amounts of Pb even though the sampled material is much younger than the material from the Bruse feeder structure. The vent fluids of the Perle vent field might be lower in Pb, or it might form during a late stage of paragenesis. Fallen down chimneys of the Aegir vent field shows relatively similar values between the inner part of GS15-AGR10-R2 and GS16B-ROV7-R01. The outer parts of GS15-AGR10-R2 on the other hand have lower values indicating smaller amounts of sulphides in the outer parts of the chimney. The active chimney GS16B-ROV9-R01 has relatively low amounts of the elements compared to the other Aegir samples, which could indicate that the active chimney is relatively young compared to the other sampled material from this vent field, or that it is fluids less enriched in these elements that have formed this chimney. The inactive in-situ chimney GS16B-ROV7-R02 has the highest amounts of elements amongst the sampled material. This indicates either that the chimney is older than the other sampled material leaving more time for sulphide enrichment, or that fluids that have formed this chimney are more enriched than the other vents at this vent field. Figure 64 shows values for Mg that varies greatly between the Perle and Bruse Vent field, and Aegir. This is likely connected to the amount of silica in the samples, as this element is most likely derived from seawater, which are enriched in Mg compared to hydrothermal fluids. Samples from Aegir vent field is rich in silica compared to Perle and Bruse, a mixture between seawater rich in Mg and hydrothermal fluids rich in silica leading to precipitation of silica rich in Mg is the most likely explanation of this. The same distribution of values can also be seen for Na, and is likely connected to the same process.

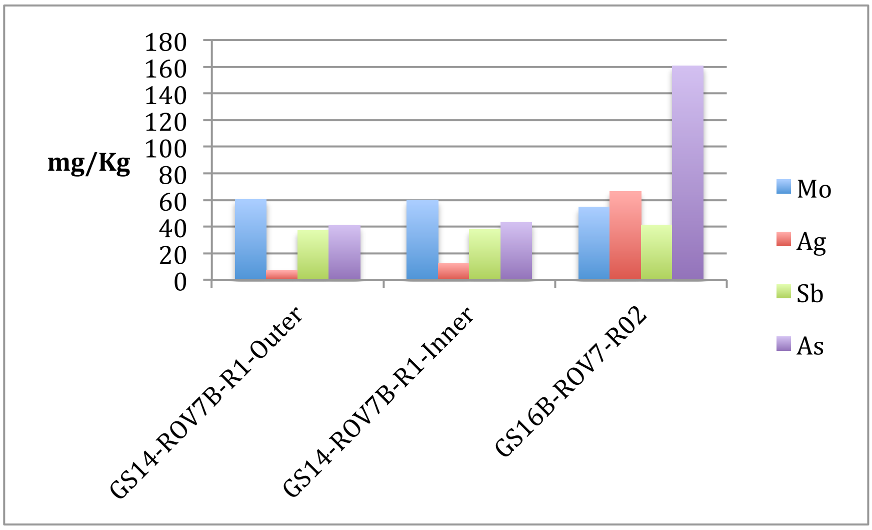

Figure 67: Diagram based on values from Figure 65, and shows distribution of the elements Mo, Ag, Sb and As, for samples enriched in these elements.

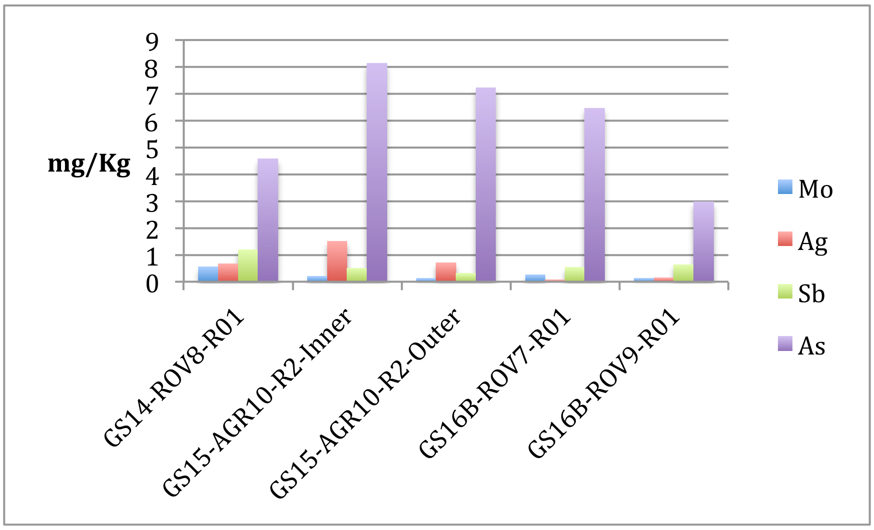

Figure 68: Diagram based on values from Figure 65, and shows distribution of the elements Mo, Ag, Sb and As, for samples with lower amounts of these elements.

The elements Mo, Ag, Sb and As (values listed in figure 65 and shown in figure 67 and 68) are most likely linked to sulphides found in the samples. These elements readily go into the crystal lattice or are found as inclusions in the sulphides. Mo can be found in pyrite and sphalerite; Ag can be found in pyrite, chalcopyrite and sphalerite; Sb can be found in pyrite and sphalerite; As can be found in pyrite and sphalerite (Huston et al., 1995). From EDS microanalysis of the sulphides found in the samples it is evident that they contain trace elements. Samples enriched in the elements (Figure 67) are the feeder structure from Bruse (GS14-ROV7B-R1) and the in-situ inactive chimney from Aegir (GS16B-ROV7-R02). The Bruse feeder structure is older than the other dated material (Figure 68), and the Aegir in-situ inactive chimney is thought to be older than the rest of the sampled material based on the mineralogical composition of the chimney. This might be the explanation for the enrichment of these samples, as the material is progressively enriched by these elements from the fluids migrating trough the material. Another explanation might be that the fluids that have formed these samples are more enriched in these elements, making the material formed from these fluids enriched in the elemements.

Element	Analythical method	GS14-ROV7B-R2	GS-14-ROV8-R1
Ca (%)	AR-ICP	3,19	8,26
Fe (%)	INAA	0,29	0,8
K(%)	AR-ICP	< 0.01	0,01
Na(%)	INAA	0,1	0,06
S(%)	AR-ICP	3,14	8,868
Si(%)	FUS-Na2O2	0,16	0,07
Ag (ppm)	MULT INAA / AR-ICP	38,3	2,8
As (ppm)	INAA	27	9
Cd (ppm)	AR-ICP	43,5	133
Cu (ppm)	AR-ICP	1190	1290
Mn (ppm)	AR-ICP	< 2	4
Mo (ppm)	AR-ICP	33	2
Ni (ppm)	MULT INAA / AR-ICP	< 1	1
Pb (ppm)	AR-ICP	2090	34
Zn (ppm)	MULT INAA / AR-ICP	3870	4730
Ba (ppm)	MULT INAA / AR-ICP	478000	8400
Bi (ppm)	AR-MS	< 0.10	< 0.10
Cs (ppm)	MULT INAA / AR-ICP-MS	< 0.05	< 0.05
Ga (ppm)	AR-MS	4	4
Ge(ppm)	AR-MS	< 0.1	< 0.1
Sb(ppm)	INAA	118	2,6
Se(ppm)	MULT INAA / AR-ICP-MS	12,2	6
Te(ppm)	AR-MS	< 0.1	< 0.1
Tl(ppm)	AR-MS	0,3	0,3
W(ppm)	INAA	< 4	< 4
Hg(ppm)	INAA	< 1	2
Au (ppb)	INAA	638	248

Figure 69: Table over the analysis results from ACTLABS for the active chimney at Bruse GS14-ROV7B-ROV-R2, and Perle GS14-ROV8-R01. "<" Indicate that the values for the sample are under the detection limit.

Even though the bulk chemical analysis from ACTLABS (Figure 69) has multiple elements under the detection limit, it indicates anyhow the difference in concentrations for most elements in the samples and can therefore be used as an indication of the compositional differences between the samples. The Powder used for the ACTLABS bulk chemical analysis for the sample GS14-ROV8-R1 is different from what was used in-house at UIB and therefore depicts other values, as hydrothermal material is heterogenous.

6 Discussion

6.1 Southern Mohns ridge: The Jan Mayen hydrothermal system

6.1.1 Perle vent system

The hydrothermal products found at Perle Vent field are dominated by anhydrite with relatively abundant amounts of sulphides and late stage of barite mixed with silica found in the active vent (GS14-ROV8-R1). Barite is found mostly as mound material of the site where lower temperature diffuse venting occurs, and has low amounts of sulphides. The fluids venting at approximately 248ºC and at 567 m deep (E. Reeves, personal communication) are close to the two-phase boundary for phase separation (Hannington, 2014; German and Von Damm, 2006; Bischoff and Rosenbauer, 1985) The bubbling vent fluids are an indicator that phase separation occurs as the fluids cross the two-phase boundary as they rise towards the seafloor. Analysis of the vent fluids shows an anomalously high content of CO_2 (F. Marques, personal communication), high CO_2 concentrations in vent fluids might be an indication that the fluids are affected by a recent magmatic event (Pester et al., 2012; Reeves et al., 2011). The hydrothermal products at this site seem to be strongly affected by the phase separation, as the chimneys are very small and extremely brittle. The active chimney from Perle (GS14-ROV8-R01) contains however a fair amount of sulphides suggesting that metals are being transported in the vent fluids even though the fluids undergo phase separation. Since the sampled material shows that the main constituent of the hydrothermal products found amongst the mound rubble (GS14-ROV8-Shuffle) are sulphates. The mound rubble is most likely made up of clasts from collapsed broken up chimneys, the low amount of sulphides in the mound material indicates that the broken down chimney material have not gone into phase 2 of chimney growth. The chimeys are not enriched in sulphides, which decreases the porosity and most likely also affects how fragile the chimneys are (Tivey, 2007; Tivey, 1998). The result is that sulphides do not seal off the vent structure and the chimneys are therefore very brittle and porous. During ROV dives this is evident, as chimneys that were attempted sampled would simply collapse and shatter into fine particles when the grabber of the ROV tried to pick them up. Since the chimneys are so brittle it is very likely that they easily break down if they are subjected to external forces such as ocean currents or earthquakes. It seems like the chimneys are mostly brittle in the upper parts of the chimney structure, as multiple of the observed chimneys during ROV dives tend to be forming a pointy cone on top of a thicker and more solid base. Indicating that the chimney is growing upwards and outwards with formation of anhydrite (Heymon, 1983). The active chimney sample (GS14-ROV8-R01) was taken from the base of one of the vents and is relatively solid. The sample is relatively rich in sulphides. This shows that the lowermost sturdier parts of the chimneys enter into phase 2 and are more solid than the upper parts of the chimney. Small amounts of barite mixed with silica in the active sampled chimney indicate that there is an onset of barite precipitiation during late stage mineralization for these hydrothermal products.

6.1.2 Bruse vent field

The hydrothermal material sampled from the Bruse vent field are composed mostly by barite, minor anhydrite sulphides and silica. The chimneys in Bruse vent field are generally larger than in Perle Vent Field and appear also to be more robust than the samples collected at Perle. This is due to the barite-dominated mineralogy. To collect the samples at Bruse vent field a chainsaw was used to cut off pieces that could be collected by the ROV. The samples from the active chimney (GS14-ROV7B-R2) are dominated by barite followed by anhydrite crystals that are partly dissolved indicating that are no longer in equilibrium with the fluid. Silica seems to be a later phase at it is often found between the barite crystals. The feeder structure in the mound area of the vent field (GS14-ROV7b-R1) is too dominated by barite. Textural and mineralogical observations suggest that the chimneys formed with crystallization of anhydrite during phase 1, followed by formation of barite within the chimney structure. The sulphide assemblage is similar in both Perle and Bruse vent areas, except for the presence of covellite in Bruse that seems to replace chalcopyrite. This means that the chalcopyrite is reworked due to changes in redox or solution compositions (Janecky and Seyfried, 1984). The first sulphide phase to form is pyrite followed by chalcopyrite. Both mineral phases can be found included in larger and later sphalerite. In some areas, sphalerite forms in parallel with chalcopyrite and galena. Galena is exclusively found associated to sphalerite and is often included inside the sphalerite growths. This indicates that the chimney structure is growing and temperatures are rising or be due to changes in the fluid chemistry within the chimney that in turn leads to the crystallization of other mineral phases within the chimney structure. The last sulphide phase to occur is covellite. This mineral is formed as a secondary product from the reworking of chalcopyrite within the chimney structure, and indicates that the chimney has been cooling and that there has been an increased mixing with seawater (Janecky and Seyfried, 1984) The age of the barite mineralization in this active chimney is also indicating that the reworking of the minerals inside the chimney has been a relatively longer process when compared to the other samples.

6.1.3 Similarities and differences between the Perle and Bruse vent field

To best look at the similarities and differences between Perle and Bruse it is best to look at the active chimneys (GS14-ROV8-R1 and GS14-ROV7B-R2), as these are almost of identical age derived from radiometric dating of Barite. Perle active chimney has an age of 7,4±0,4 years, and Bruse active chimney has an age of 8,7±0,3 years. If we look at the size of the chimneys they are quite different, as the active bruse chimney is much larger than the Perle chimney even though they are relatively close in age. This could be due to the fact that the Bruse chimney is dominated by barite as the dominating sulphate phase, and is much more solid than the Perle chimney which is dominated by anhydrite and is more fragile. This difference was easily witnessed while sampling the chimneys as the Bruse chimney required to be cut down by a chainsaw while the Perle chimney easily could be gathered by only the use of the grabber. The difference in barite content can easily be seen from the bulck chemical analysis (Figure 69), where the bruse chimney is enriched in contrast to the Perle chimney. The mineralogical composition of the two chimneys is quite similar when it comes to the sulphide phases and their paragenesis. Temperatures for both vent fields are close to 250°C, with measured temperatures of 242°C (E. Reeves, personal communication) for the Bruse vent field and 248°C for the Perle vent field (F. Marques, personal communications). It is needed temperatures between 350-250°C for chalcopyrite to form, and this phase is present in each vent field indicating that the temperature is sufficiently high enough to precipitate this mineral (Hannington, 2014). This indicates that temperatures of the vent fluids might not be the cause of the differences we see between the two systems. The Perle active chimney does not contain galena as can be seen from the low Pb values for this sample in figure 64 and 69, indicating that Pb is not available in the fluids. The presence of CO_2 rich bubbles coming from the Perle active chimney (F. Marques, personal communication) could indicate that Perle hydrothermal fluids are affected by recent magmatic events (Pester et al., 2012; Reeves et al., 2011). Magmatic fluids might therefore affect the fluids at the Perle vent field, while the Bruse vent field does not show tendencies to be affected. Even though the two went fields are in close proximity to each other, magmatic activity in close proximity to Perle vent field might affect the fluids at this site while leaving Bruse unaffected. Since the two vent fields are found in the approximate same water depth, and the hydrothermal fluids are measured to be of nearly equal temperature a difference in plumbing system might be the explanation for the differences between the two systems. On the other hand, the similarities in depth and temperature between the two vent fields explain the similarities in mineral phases and isotopic values of $^{87/86}$Sr and δ^{34}S.

6.2 Central Mohns ridge

6.2.1 Aegir vent field

The hydrothermal material sampled from the Aegir site is composed of anhydrite and barite, with minor silica and sulphides. Following the growth model of Tivey, 2007; Tivey, 1998, the chimneys is formed with the precipitation of anhydrite on an initial stage (phase 1). Subsequently this stage is followed by the formation of barite, silica and sulphides in phase 2. The barite found in the samples is clustered together in patches and seems to have formed in open spaces such as veins or micro orifices. The amount of anhydrite seems to decline as the chimneys go from phase 1 to phase 2. This could either be due to; (1) anhydrite dissolution as the chimney grows, temperature rises and fluids become more reduced, (2) Ba-rich hydrothermal fluids that favour barite formation over anhydrite, or (3) a combination of both.

Semi-quantitative SEM-EDS analysis in microcrystalline silica found in the chimneys indicates contents in magnesium and Fe (SEM-EDS). Hydrothermal fluids are depleted in magnesium (Alt, 1995), but seawater is rich. Therefore, silica and Fe must stem from the hydrothermal fluids, so that the silica in the chimneys is formed as a mixture between silica and Fe-rich hydrothermal fluids and Mg-rich seawater. The sulphide phases found in the chimneys are pyrite, chalcopyrite, sphalerite and galena. This mineral phase is found in all the chimneys in varying amounts. The first sulphide to precipitate in the chimneys is pyrite. Pyrite crystals are generally much larger than the other sulphide crystals found in the thin section. Chalcopyrite seconds pyrite and is often seen coating the outside of pyrite crystals, this is most likely due to the chimney growing thicker and temperatures within the chimney structure increasing enabling Cu-transport. The last suphide phases to occur are sphalerite and galena. Pyrite and chalcopyrite are often found as inclusions inside sphalerite. Galena is found in association with sphalerite, within the sphalerite crystals. A mixture of hydrothermal fluids and seawater inside the chimney walls much likely forms the sphalerite and galena. Sulphides are found in association with silica, and are often found inside or around the silica in the sample. This suggests that the silica and sulphide phases had the same means of formation with a varying degree of mixture between hydrothermal fluids and seawater that lead to precipitation in the veins and orifices in the chimney structure. Since all the chimney samples include the same mineral phases it is possible that they show different ages with respect to the enrichment of silica and sulphides found in the chimney. As the chimneys grow older the open spaces in the chimney structure gets progressively filled with silica and sulphide until all the fluid pathways are filled and the fluids are cut off from the chimney. The in situ inactive chimney GS16-ROV7-R02 seems to be the most developed in this sense, with very high amounts of sulphides relative to the other sampled chimneys at this site (Figure 66). The chimney is extinct and showed no signs of emanating hot fluids during sampling. However, due to the higher content of sulphides it could be that this chimney vented higher temperature fluids when compared to the other the sampled chimneys from the site, or be formed from fluids richer in sulphide forming elements. Fluids exiting the chimney GS16-ROV9-R01 were around 279°C (E. Reeves, personal communication). But temperatures could be higher due to the physical parameters at this vent field. With depth close to that of Loki´s castle (Aegir ~2320m; Loki´s castle ~2400m), which has temperatures in excess of 310-320°C, it is likely that hydrothermal fluids at Aegir vent field can reach temperatures higher than the measured ones (German and Von Damm, 2006; Bischoff and Rosenbauer, 1985; Pedersen et al, 2010a; Pedersen et al., 2010b). The most likely explanation for the differences observed in this chimney is that the chimney is much older and has had time to form more silica and sulphides within the chimney structure, as it shares the mineralogical features of the other chimneys at this vent field. With higher temperatures it is likely that other mineral phases would have formed such as talc as seen at Loki´s castle (Pedersen et al., 2010a; Tivey, 1998). It is therefore possible to make assumptions about relative age relations of the chimneys at the Aegir Vent Field with regards to how far the individual vent chimneys have come in their evolution. From these assumptions the oldest chimney of the site is the inactive in situ chimney GS16-ROV7-R02, as this has a very high content of both silica and sulphides.

6.3 Differences between hydrothermal activity in the Southern and Central Mohns ridge

The tectonic setting of the Perle and Bruse and Aegir vent field are different, as the Jan Mayen hydrothermal system that Perle and bruse is part of is situated on the southern segment of Mohns ridge that is affected by the Jan Mayen mantle plume (Elkins et al. 2016). Both the Jan Mayen and Aegir hydrothermal systems are hosted in basalts, but the basalt composition differs as the Jan Mayen hydrothermal system is closer to the Jan Mayen anamoly, which gives basalts of different composition with an decrease in Jan Mayen signature NorthEastwards along the Mohns ridge (Neumann and Schilling, 1984; Elkins et al. 2016). Spreading is also different from Southern Mohns ridge to central Mohns ridge due to the Jan Mayen plume affecting Southern, which has orthogonal spreading instead of the highly oblique spreading found on central and northern Mohns ridge (Deuteuil and Brun, 1993; Pedersen et al., 2010b). In detail, there are observable differences between each hydrothermal system, and each vent within a system. The hydrothermal products found in Perle og Bruse vents in the Jan Mayen area are dominated by sulphates with only minor amounts of silica. The vent chimneys are small in size, which relates to several factors, namely the chimneys mineral composition and the relative maturity of the chimney. The shallow depth of the vent fields Perle (567 m) and Bruse (594 m) means that these vents will phase separate at 270 ºC without phase separation (Hannington, 2014; German and Von Damm, 2006; Bischoff and Rosenbauer, 1985). This is agreement with the observed temperatures of the hydrothermal fluids at Perle (248ºC) (F.Marques, personal communication) and Bruse (242ºC) (E. Reeves, personal communication) that are not sufficiently high to transport and consequently precipitate the amounts of sulphides required to form a vigorously growing sulfide rich chimneys. Instead, the chimneys are brittle, as sulphides do not seal the interior chimney structure as in high temperature black smoker vents (Tivey, 1998). Due to the small sized chimneys in the Perle vent area, it can be thought that the chimneys do not exit stage 1 (Tivey and McDuff, 1990) and it therefore cannot grow larger than a certain size as the brittle material the chimney is composed of will break down continuously as it cannot sustain the weight. The Aegir vent chimneys are on the other hand generally larger, the measured temperatures at this vent field is higher but not sufficiently enough to sustain metal rich fluids (black smoker fluids). The hydrothermal products of the Aegir Vent Field are different from that of Jan Mayen Vent field as they do have a high composition of silica. A high content of silica in the Aegir Vent Field chimneys may explain why they can grow so large with a relatively low content of sulphide. On the other hand both Perle and Bruse and Aegir shares the same sulphate and sulphide assemblages with the exception of covellite which can only be found in the Bruse vent field, and galena which is not abundant in the Perle vent field but can be found in Bruse samples. This might be due to the age differences we see between the sampled material at these two sites, as galena might not have has sufficient time to develop. It could also be that vent fluids at the Perle site are lower in galena. So even though the geological setting and depth of formation is different the similarities between mineralogy and paragenesis during vent formation are evident between the Perle and Bruse and Aegir vent field.

7 Conclusion

- Perle and bruse shares many common characteristics due to similar depth of formation and fluid temperatures, but differences in geochemistry seen in the different hydrothermal products sampled from the systems can be explained trough the two systems not sharing a common plumbing system.
- The same effect is seen between the Perle and Bruse and Aegir vent field. Even though Aegir vent field is found at a greater depth and different tectonic setting, temperatures at this vent field are similar to those found at Perle and Bruse. This leads to similar paragenesis and similar mineralogical composition.
- The differences in chimney size between Perle and Bruse, and Aegir vent field is most likely due to the higher amounts of silica found in the Aegir vent field. The silica seals off the chimneys and makes it possible for the chimneys to grow larger at Aegir vent field.
- The difference between degree of sulphide enrichment in the sampled material of the vent fields are likely controlled by duration of venting with an progressive enrichment over time, rather than large variations in fluid temperature and fluid chemistry.
- Samples analysed for $^{87/86}$Sr isotopic ratios shows formation of mineralization trough mixing of hydrothermal fluids and seawater. δ^{34}S shows that the sulphur is derived from seawater.
- The sampled chimney material of all vent fields shows the same formation process with initial formation of anhydrite followed by barite precipitation and removal of anhydrite as it dissolves at lower temperatures. Silica forms in the open pore spaces in varying amounts. The sulphide phases are initiated by pyrite followed by chalcopyrite, sphalerite and galena. Galena is found exclusively in association with sphalerite. Sulphides either forms on the dissolving anhydrite or in the pore space in association with silica. Covellite is found in the Bruse feeder structure formed as a secondary product from chalcopyrite.

Future work:

To increase the knowledge about the vent fields systematic sampling needs be done in order to better understand the processes of chimney growth found at these sites. To better understand the differences between the vent fields more sampled material is needed. Due to the fact that the chimneys composition changes over time, it might be better to take cores instead as this might better show the features of the individual vent field better than chimneys.

References:

Alt, J.C., 1995. Subseafloor Processes in Mid-Ocean Ridge Hydrothennal Systems. Seafloor Hydrothermal Systems: Physical, Chemical, Biological, and Geological Interactions, pp.85-114.

Beaulieu, S.E., Baker, E.T., German, C.R. and Maffei, A., 2013. An authoritative global database for active submarine hydrothermal vent fields. Geochemistry, Geophysics, Geosystems, 14(11), pp.4892-4905.

Beaulieu, S.E., Baker, E.T. and German, C.R., 2015. Where are the undiscovered hydrothermal vents on oceanic spreading ridges?. Deep Sea Research Part II: Topical Studies in Oceanography, 121, pp.202-212.

Beaulieu, S., Joyce, K. and Soule, S.A. (2010) InterRidge Vents Database Version 2.0. funding from InterRidge and Morss Colloquium Program at WHOI. World Wide Web electronic publication. https://www.interridge.org/irvents/maps (Downloaded 22.02.2017 at 15.00)

Bischoff, J.L. and Seyfried, W.E., 1978. Hydrothermal chemistry of seawater from 25 degrees to 350 degrees C. American Journal of Science, 278(6), pp.838-860.

Bischoff, J.L. and Rosenbauer, R.J., 1985. An empirical equation of state for hydrothermal seawater (3.2 percent NaCl). American Journal of Science, 285(8), pp.725-763.

Boschen, R.E., Rowden, A.A., Clark, M.R. and Gardner, J.P.A., 2013. Mining of deep-sea seafloor massive sulfides: a review of the deposits, their benthic communities, impacts from mining, regulatory frameworks and management strategies. Ocean & coastal management, 84, pp.54-67.

Chen, Y.J., 1992. Oceanic crustal thickness versus spreading rate. Geophysical Research Letters, 19(8), pp.753-756.

Cochran, J.R., Kurras, G.J., Edwards, M.H. and Coakley, B.J., 2003. The Gakkel Ridge: Bathymetry, gravity anomalies, and crustal accretion at extremely slow spreading rates. Journal of Geophysical Research: Solid Earth, 108(B2).

Connelly, D.P., German, C.R., Asada, M., Okino, K., Egorov, A., Naganuma, T., Pimenov, N., Cherkashev, G. and Tamaki, K., 2007. Hydrothermal activity on the ultra-slow spreading southern Knipovich Ridge. Geochemistry, Geophysics, Geosystems, 8(8).

Connelly, D.P., German, C.R., Naganuma, T., Pimenov, N., Egorov, A. and Dohsik, H., 2002, December. Hydrothermal Plume Signals Along the Knipovich Ridge. In AGU Fall Meeting Abstracts.

Corliss, J.B., Dymond, J., Gordon, L.I. and Edmond, J.M., 1979. on the Galapagos Rift. Science, 203, p.16.

Curewitz, D. and Karson, J.A., 1997. Structural settings of hydrothermal outflow: Fracture permeability maintained by fault propagation and interaction. Journal of Volcanology and Geothermal Research, 79(3), pp.149-168.

Dauteuil, O. and Brun, J.P., 1996. Deformation partitioning in a slow spreading ridge undergoing oblique extension: Mohns Ridge, Norwegian Sea. Tectonics, 15(4), pp.870-884.

Dauteuil, O. and Brun, J.P., 1993. Oblique rifting in a slow-spreading ridge. Nature, 361, pp.145-148.

Deniel, C., Pin, C., 2001. Single-stage method for the simultaneous isolation of lead and strontium from silicate samples for isotopic measurements. Analytica Chimica Acta, 426(1), pp.95-103.

de Ronde, C.E., Faure, K., Bray, C.J., Chappell, D.A. and Wright, I.C., 2003. Hydrothermal fluids associated with seafloor mineralization at two southern Kermadec arc volcanoes, offshore New Zealand. *Mineralium Deposita*, *38*(2), pp.217-233.

de Ronde, C.E., Hannington, M.D., Stoffers, P., Wright, I.C., Ditchburn, R.G., Reyes, A.G., Baker, E.T., Massoth, G.J., Lupton, J.E., Walker, S.L. and Greene, R.R., 2005. Evolution of a submarine magmatic-hydrothermal system: Brothers volcano, southern Kermadec arc, New Zealand. *Economic Geology*, *100*(6), pp.1097-1133.

Dick, H.J., Lin, J. and Schouten, H., 2003. An ultraslow-spreading class of ocean ridge. Nature, 426(6965), pp.405-412.

Ditchburn, R.G., de Ronde, C.E. and Barry, B.J., 2012. Radiometric Dating of Volcanogenic Massive Sulfides and Associated Iron Oxide Crusts with an Emphasis on 226Ra/Ba and 228Ra/226Ra in Volcanic and Hydrothermal Processes at Intraoceanic Arcs. Economic Geology, 107(8), pp.1635-1648.

Ditchburn, R.G., Graham, I.J., Barry, B.J. and de Ronde, C.E., 2004. Uranium series disequilibrium dating of black smoker chimneys. *New Zealand Science Review*, *61*(2), pp.54-56.

Edmonds, H.N., Michael, P.J., Baker, E.T., Connelly, D.P., Snow, J.E., Langmuir, C.H., Dick, H.J.B., Mühe, R., German, C.R. and Graham, D.W., 2003. Discovery of abundant hydrothermal venting on the ultraslow-spreading Gakkel ridge in the Arctic Ocean. Nature, 421(6920), pp.252-256.

Eickmann, B., Thorseth, I.H., Peters, M., Strauss, H., Bröcker, M. and Pedersen, R.B., 2014. Barite in hydrothermal environments as a recorder of subseafloor processes: a multiple-isotope study from the Loki's Castle vent field. Geobiology, 12(4), pp.308-321.

Elkins, L.J., Hamelin, C., Blichert-Toft, J., Scott, S.R., Sims, K.W.W., Yeo, I.A., Devey, C.W. and Pedersen, R.B., 2016. North Atlantic hotspot-ridge interaction near Jan Mayen Island. Geochemical Perspectives Letters, 2(1), pp.55-67.

Engel, A.J., Engel, C.G. and Havens, R.G., 1965. Chemical characteristics of oceanic basalts and the upper mantle. Geological Society of America Bulletin, 76(7), pp.719-734.

Fehn, U. and Cathles, L.M., 1979. Hydrothermal convection at slow-spreading mid-ocean ridges. Tectonophysics, 55(1-2), pp.239-260.

Francis, T.J.G., 1981. Serpentinization faults and their role in the tectonics of slow spreading ridges. Journal of Geophysical Research: Solid Earth, 86(B12), pp.11,616-11,622.

Franklin, J.M., Gibson, H.L., Galley, A.G. & Jonasson, I.R. 2005. Volcanogenic Massive Sulfide Deposits. In: Hedenquist, J.W., Thompson, J.F.H., Goldfarb, R.J. & Richards, J.P. (eds) Economic Geology 100th Anniversary Volume. Society of

Economic Geologists, Littleton, CO, 523– 560.

Géli, L., Renard, V. and Rommevaux, C., 1994. Ocean crust formation processes at very slow spreading centers: A model for the Mohns Ridge, near 72 N, based on magnetic, gravity, and seismic data. Journal of Geophysical Research: Solid Earth, 99(B2), pp.2995-3013.

Géli, L., 1993. Volcano-tectonic events and sedimentation since late Miocene times at the Mohns Ridge, near 72 N, in the Norwegian-Greenland Sea. Tectonophysics, 222(3-4), pp.417-444.

German, C.R. and Von Damm, K.L., 2006. Hydrothermal processes. Treatise on geochemistry, 6, pp.181-222.

Gernigon, L., Olesen, O., Ebbing, J., Wienecke, S., Gaina, C., Mogaard, J.O., Sand, M. and Myklebust, R., 2009. Geophysical insights and early spreading history in the vicinity of the Jan Mayen Fracture Zone, Norwegian–Greenland Sea. Tectonophysics, 468(1), pp.185-205.

Grassle, J.F., 1985. Hydrothermal vent animals: distribution and biology. Science(Washington), 229(4715), pp.713-717.

Griffith, E.M. and Paytan, A., 2012. Barite in the ocean–occurrence, geochemistry and palaeoceanographic applications. Sedimentology, 59(6), pp.1817-1835.

Hannington, M.D., 2014. 13.18-Volcanogenic Massive Sulfide Deposits. Treatise on geochemistry, 13, pp. 463-488. DOI: 10.1016/b978-0-08-095975-7.01120-7

Hannington, M.D., Jonasson, I.R., Herzig, P.M. and Petersen, S., 1995. Physical and chemical processes of seafloor mineralization at mid-ocean ridges. Seafloor hydrothermal systems: Physical, chemical, biological, and geological interactions, pp.115-157.

Hanor, J.S., 2000. Barite–celestine geochemistry and environments of formation. Reviews in Mineralogy and Geochemistry, 40(1), pp.193-275.

Haymon, R.M., 1983. Growth history of hydrothermal black smoker chimneys. Nature, 301, pp.695-698.

Haymon, R.M., 1996. The response of ridge-crest hydrothermal systems to segmented, episodic magma supply. Geological Society of London Special Publications, 118, pp.157-168.

Herzig, P.M., Hannington, M.D. and Arribas Jr, A., 1998. Sulfur isotopic composition of hydrothermal precipitates from the Lau back-arc: implications for magmatic contributions to seafloor hydrothermal systems. Mineralium Deposita, 33(3), pp.226-237.

http://www.actlabs.com/page.aspx?page=725&app=276&cat1=685&tp=12&lk=no&menu=73 (Read 27.10.2016 at 16.00)

http://moocs.southampton.ac.uk/oceans/2014/10/04/mapping-the-deep-and-the-real-story-behind-the-95-unexplored-oceans/ (Read 12.10.2016 at 19.22)

http://www.nautilusminerals.com/irm/content/overview1.aspx?RID=257&RedirectCount=1 (Read 28.10.2016 at 17.15)

http://www.nautilusminerals.com/irm/content/overview.aspx?RID=252 (Read 28.10.2016 at 17.30)

http://www.nautilusminerals.com/irm/content/status-of-the-equipment.aspx?RID=424 (Read 28.01.2017 at 18.00)

Humphris, S.E., Herzig, P.M., Miller, D.J., Alt, J.C., Becker, K., Brown, D., Brügmann, G., Chiba, H., Fouquet, Y., Gemmell, J.B. and Guerin, G., 1995. The internal structure of an active sea-floor massive sulphide deposit. Nature, 377(6551), pp.713-716.

Husson, L., Yamato, P. and Bezos, A., 2015. Ultraslow, slow, or fast spreading ridges: Arm wrestling between mantle convection and far-field tectonics. Earth and Planetary Science Letters, 429, pp.205-215.

Huston, D.L., Sie, S.H., Suter, G.F., Cooke, D.R. and Both, R.A., 1995. Trace elements in sulfide minerals from eastern Australian volcanic-hosted massive sulfide deposits; Part I, Proton microprobe analyses of pyrite, chalcopyrite, and sphalerite, and Part II, Selenium levels in pyrite; comparison with delta 34 S values and implications for the source of sulfur in volcanogenic hydrothermal systems. *Economic Geology*, *90*(5), pp.1167-1196.

Jamieson, J.W., Hannington, M.D., Petersen, S., Tivey, M.K., 2014. Volcanogenic Massive Sulfides. Encyclopedia of Marine Geosciences DOI 10.1007/978-94-007-6644-0_37-1

Jamieson, J.W., Hannington, M.D., Tivey, M.K., Hansteen, T., Williamson, N.M.B., Stewart, M., Fietzke, J., Butterfield, D., Frische, M., Allen, L. and Cousens, B., 2016. Precipitation and growth of barite within hydrothermal vent deposits from the Endeavour Segment, Juan de Fuca Ridge. Geochimica et Cosmochimica Acta, 173, pp.64-85.

Jupp, T.E. and Schultz, A., 2004. Physical balances in subseafloor hydrothermal convection cells. *Journal of Geophysical Research: Solid Earth*, *109*(B5).

Janecky, D.R. and Seyfried, W.E., 1984. Formation of massive sulfide deposits on oceanic ridge crests: Incremental reaction models for mixing between hydrothermal solutions and seawater. *Geochimica et Cosmochimica Acta*, *48*(12), pp.2723-2738.

Kandilarov, A., Mjelde, R., Pedersen, R.B., Hellevang, B., Papenberg, C., Petersen, C.J., Planert, L. and Flueh, E., 2012. The northern boundary of the Jan Mayen microcontinent, North Atlantic determined from ocean bottom seismic, multichannel seismic, and gravity data. Marine Geophysical Research, 33(1), pp.55-76.

Klingelhöfer, F., Géli, L. and White, R.S., 2000a. geophysical and geochemical constraints on crustal accretion at the very-slow spreading mohns ridge. Geophysical Research Letters, 27(10), pp.1547-1550.

Klingelhöfer, F., Geli, L., Matias, L., Steinsland, N. and Mohr, J., 2000b. Crustal structure of a super-slow spreading centre: a seismic refraction study of Mohns Ridge, 72 N. Geophysical Journal International, 141(2), pp.509-526.

Kusakabe, M. and Robinson, B.W., 1977. Oxygen and sulfur isotope equilibria in the BaSO4 HSO4− H2O system from 110 to 350° C and applications. Geochimica et Cosmochimica Acta, 41(8), pp.1033-1040.

Kusakabe, M., Mayeda, S. and Nakamura, E., 1990. S, O and Sr isotope systematics of active vent materials from the Mariana backarc basin spreading axis at 18 N. *Earth and Planetary Science Letters*, *100*(1-3), pp.275-282.

Los, C., Bach, W. and Plümper, O., 2016, April. Replacive sulfide formation in anhydrite chimneys from the Pacmanus hydrothermal field, Papua New Guinea. In EGU General Assembly Conference Abstracts (Vol. 18, p. 12042).

Lowell, R.P. and Rona, P.A., 2002. Seafloor hydrothermal systems driven by the serpentinization of peridotite. Geophysical Research Letters, 29(11).

Marques, A.F.A., Pedersen, R.B., Roerdink, D.L., Baumberger, T., Denny, A., Thorseth, I.H., Okland, I., Lilley, M.D., Ronde, C.D., Ditchburn, B., Hamelin, C., In press. First record of epithermal-type mineralization on a shallow submarine volcano on the slow spreading Arctic Mid-Ocean Ridge.

Martin, W., Baross, J., Kelley, D. and Russell, M.J., 2008. Hydrothermal vents and the origin of life. Nature Reviews Microbiology, 6(11), pp.805-814.

Misra, K., 2012. Understanding mineral deposits. Springer Science & Business Media.

Neumann, E.R. and Schilling, J.G., 1984. Petrology of basalts from the Mohns-Knipovich ridge; the Norwegian-Greenland Sea. Contributions to Mineralogy and Petrology, 85(3), pp.209-223.

Ohmoto, H., 1996. Formation of volcanogenic massive sulfide deposits: the Kuroko perspective. Ore geology reviews, 10(3), pp.135-177.

Ohmoto, H., 1972. Systematics of sulfur and carbon isotopes in hydrothermal ore deposits. Economic Geology, 67(5), pp.551-578.

Olsen BR, Økland IE, Thorseth IH, Pedersen RB, Rapp HT (2016) Environmental challenges related to offshore mining and gas hydrate extraction. Norwegian Environment Agency. Report no: M-532-2016.

Paytan, A., Mearon, S., Cobb, K. and Kastner, M., 2002. Origin of marine barite deposits: Sr and S isotope characterization. *Geology*, *30*(8), pp.747-750.

Pedersen, R.B., et al. 2016. Cruise report, C-DEEP 2016 expedition R/V G.O. Sars. University of Bergen.

Pedersen, R.B., Thorseth, I.H., Nygård, T.E., Lilley, M.D. and Kelley, D.S., 2010b. Hydrothermal activity at the Arctic mid-ocean ridges. Washington DC American Geophysical Union Geophysical Monograph Series, 188, pp.67-89.

Pedersen, R.B., Rapp, H.T., Thorseth, I.H., Lilley, M.D., Barriga, F.J., Baumberger, T., Flesland, K., Fonseca, R., Früh-Green, G.L. and Jorgensen, S.L., 2010a. Discovery of a black smoker vent field and vent fauna at the Arctic Mid-Ocean Ridge. Nature Communications, 1:126. doi:10.1038/ncomms1124

Pedersen, R.B., Thorseth, I.H., Hellevang, B., Schultz, A., Taylor, P., Knudsen, H.P. and Steinsbu, B.O., 2005. Two vent fields discovered at the ultraslow spreading Arctic ridge system. In AGU Fall Meeting Abstracts (Vol. 1, p. 01).

Perry, R.K., 1986. Bathymetry. In The Nordic Seas (pp. 211-236). Springer New York.

Pester, N.J., Reeves, E.P., Rough, M.E., Ding, K., Seewald, J.S. and Seyfried, W.E., 2012. Subseafloor phase equilibria in high-temperature hydrothermal fluids of the Lucky Strike Seamount (Mid-Atlantic Ridge, 37° 17′ N). Geochimica et Cosmochimica Acta, 90, pp.303-322.

Reeves, E.P., Seewald, J.S., Saccocia, P., Bach, W., Craddock, P.R., Shanks, W.C., Sylva, S.P., Walsh, E., Pichler, T. and Rosner, M., 2011. Geochemistry of hydrothermal fluids from the PACMANUS, Northeast Pual and Vienna Woods hydrothermal fields, Manus basin, Papua New Guinea. Geochimica et Cosmochimica Acta, 75(4), pp.1088-1123.

Reid, I. and Jackson, H.R., 1981. Oceanic spreading rate and crustal thickness. Marine Geophysical Researches, 5(2), pp.165-172.

Renner, J.L., White, D.E. and Williams, D.L., 1975. Hydrothermal convection systems. In Assessment of geothermal resources of the United States (Vol. 726).

Rye, R.O. and Ohmoto, H., 1974. Sulfur and carbon isotopes and ore genesis: a review. Economic Geology, 69(6), pp.826-842.

Sakai, H., Des Marais, D.J., Ueda, A. and Moore, J.G., 1984. Concentrations and isotope ratios of carbon, nitrogen and sulfur in ocean-floor basalts. Geochimica et Cosmochimica Acta, 48(12), pp.2433-2441.

Scott, S.D. 1997. Submarine hydrothermal systems and deposits. In: Barnes, H.L. (ed.) Geochemistry of Hydrothermal Ore Deposits, 3rd Edition. John Wiley and Sons Ltd, New York, 797–875

Schilling, J.G., Kingsley, R., Fontignie, D., Poreda, R. and Xue, S., 1999. Dispersion of the Jan Mayen and Iceland mantle plumes in the Arctic: A He-Pb-Nd-Sr isotope tracer study of basalts from the Kolbeinsey, Mohns, and Knipovich ridges. Journal of Geophysical Research: Solid Earth, 104(B5), pp.10543-10569.

Siivola, J. and Schmid, R., 2007. List of Mineral Abbreviations: Recommendations by the IUGS Subcommission on the Systematics of Metamorphic Rocks. Electronic Source

Shanks III, W.C., Böhlke, J.K. and Seal, R.R., 1995. Stable isotopes in mid-ocean ridge hydrothermal systems: Interactions between fluids, minerals, and organisms. Washington DC American Geophysical Union Geophysical Monograph Series, 91, pp.194-221.

Shanks, W.C., 2001. Stable isotopes in seafloor hydrothermal systems: vent fluids, hydrothermal deposits, hydrothermal alteration, and microbial processes. Reviews in Mineralogy and Geochemistry, 43(1), pp.469-525.

Spang, A., Saw, J.H., Jørgensen, S.L., Zaremba-Niedzwiedzka, K., Martijn, J., Lind, A.E., van Eijk, R., Schleper, C., Guy, L. and Ettema, T.J., 2015. Complex archaea that bridge the gap between prokaryotes and eukaryotes. Nature, 521(7551), pp.173-179.

Spooner, E.T.C., Beckinsale, R.D., Fyfe, W.S. and Smewing, J.D., 1974. O18 enriched ophiolitic metabasic rocks from E. Liguria (Italy), Pindos (Greece), and Troodos (Cyprus). Contributions to Mineralogy and Petrology, 47(1), pp.41-62.

Stein, C.A. and Stein, S., 1994. Constraints on hydrothermal heat flux through the oceanic lithosphere from global heat flow. Journal of Geophysical Research: Solid Earth, 99(B2), pp.3081-3095.

Stein, C.A., Stein, S. and Pelayo, A.M., 1995. Heat flow and hydrothermal circulation. Washington DC American Geophysical Union Geophysical Monograph Series, 91, pp.425-445.

Sundvor (1997) Joint U.S., Russian and Norwegian research at Knipovich Ridge, Norwegian-Greenland Sea. InterRidge News 6(1): 17.

Svellingen, W. and Pedersen, R.B., 2003, April. Jan Mayen: a result of ridge-transform-micro-continent interaction. In EGS-AGU-EUG Joint Assembly (Vol. 1, abstract #12993).

Tivey, M.K., 1998. How to build a black smoker chimney. Oceanus, 41(2), p.22.

Tivey, M.K., 2007. Generation of Seafloor Hydrothermal Vent Fluids and associated Mineral Deposits. Oceanography, 20(1), p.50-65.

Tivey, M.K. and McDuff, R.E., 1990. Mineral precipitation in the walls of black smoker chimneys: a quantitative model of transport and chemical reaction. Journal of Geophysical Research: Solid Earth, 95(B8), pp.12617-12637.

Tornos, F., 2006. Environment of formation and styles of volcanogenic massive sulfides: the Iberian Pyrite Belt. Ore Geology Reviews, 28(3), pp.259-307.

Ueda, A., Krouse, H.R., 1986. Direct conversion of sulphide and sulphate minerals to SO2 for isotope analyses. Geochemical Journal, 20(4), pp.209-212.

Van Dover, C.L., 2011. Mining seafloor massive sulphides and biodiversity: what is at risk?. ICES Journal of Marine Science: Journal du Conseil, 68(2), pp.341-348.

Vogt, P.R., 1986. Seafloor topography, sediments, and paleoenvironments. In The Nordic Seas (pp. 237-412). Springer New York.

White, R.S., McKenzie, D. and O'Nions, R.K., 1992. Oceanic crustal thickness from seismic measurements and rare earth element inversions. Journal of Geophysical Research: Solid Earth, 97(B13), pp.19683-19715.